

Dark Energy Survey Year 6 Results: Cosmological Constraints from Galaxy Clustering and Weak Lensing

T. M. C. Abbott,¹ M. Adamow,² M. Aguena,^{3,4} A. Alarcon,⁵ S. S. Allam,⁶ O. Alves,⁷ A. Amon,⁸ D. Anbajagane,⁹ F. Andrade-Oliveira,¹⁰ S. Avila,¹¹ D. Bacon,¹² E. J. Baxter,¹³ J. Beas-Gonzalez,¹⁴ K. Bechtol,¹⁴ M. R. Becker,¹⁵ G. M. Bernstein,¹⁶ E. Bertin,^{17,18} J. Blazek,¹⁹ S. Bocquet,²⁰ D. Brooks,²¹ D. Brout,²² H. Camacho,^{23,4} G. Camacho-Ciurana,⁵ R. Camilleri,²⁴ G. Campailla,²⁵ A. Campos,^{26,27} A. Carnero Rosell,^{28,4,29} M. Carrasco Kind,^{2,30} J. Carretero,³¹ P. Carrilho,^{32,33} F. J. Castander,^{34,5} R. Cawthon,³⁵ C. Chang,^{36,9} A. Choi,³⁷ J. M. Coloma-Nadal,⁵ M. Costanzi,^{38,3,39} M. Crocce,^{34,5} W. d'Assignies,³¹ L. N. da Costa,⁴ M. E. da Silva Pereira,⁴⁰ T. M. Davis,²⁴ J. De Vicente,¹¹ J. DeRose,^{41,23} H. T. Diehl,⁶ S. Dodelson,^{36,6,9} C. Doux,^{16,42} A. Drlica-Wagner,^{36,6,9} T. F. Eifler,^{43,44} J. Elvin-Poole,⁴⁵ J. Estrada,⁶ S. Everett,⁴⁶ A. E. Evrard,^{47,7} J. Fang,⁴⁸ A. Farahi,^{49,50} A. Ferté,⁵¹ B. Flaugher,⁶ P. Fosalba,^{34,5} J. Frieman,^{36,6,9} J. García-Bellido,⁵² M. Gatti,^{5,9} E. Gaztanaga,^{34,12,5} G. Giannini,^{5,9} P. Giles,⁵³ K. Glazebrook,⁵⁴ M. Gorsuch,¹⁴ D. Gruen,²⁰ R. A. Gruendl,^{2,30} J. Gschwend,⁴ G. Gutierrez,⁶ I. Harrison,⁵⁵ W. G. Hartley,⁵⁶ E. Henning,³⁵ K. Herner,⁶ S. R. Hinton,²⁴ D. L. Hollowood,⁵⁷ K. Honscheid,^{58,59} E. M. Huff,^{46,44} D. Huterer,⁷ B. Jain,¹⁶ D. J. James,²² M. Jarvis,¹⁶ N. Jeffrey,²¹ T. Jeltema,⁵⁷ T. Kacprzak,⁶⁰ S. Kent,⁶ A. Kovacs,^{61,62} E. Krause,⁶³ R. Kron,^{6,9} K. Kuehn,^{64,65} O. Lahav,²¹ S. Lee,^{44,66} E. Legnani,³¹ C. Lidman,^{67,68} H. Lin,⁶ N. MacCrann,⁶⁹ M. Manera,³¹ T. Manning,² R. Marco,²⁵ J. L. Marshall,⁷⁰ S. Mau,^{71,72,73} J. McCullough,^{8,73,51,20} J. Mena-Fernández,^{74,42} F. Menanteau,^{2,30} R. Miquel,^{75,31} J. J. Mohr,²⁰ J. Muir,^{76,77} J. Myles,⁸ R. C. Nichol,⁷⁸ B. Nord,⁶ J. H. O'Donnell,⁵⁷ R. L. C. Ogando,^{79,80} A. Palmese,²⁶ M. Paterno,⁶ J. Peoples,⁶ W. J. Percival,^{45,77} D. Petrvick,² A. Pieres,^{4,81} A. A. Plazas Malagón,^{73,51} A. Porredon,^{11,82} A. Pourtsidou,^{33,83} J. Prat,⁸⁴ C. Preston,⁸⁵ M. Raveri,²⁵ W. Riquelme,⁵² M. Rodriguez-Monroy,^{86,87,82} P. Rogozenki,^{63,88} A. K. Romer,⁵³ A. Roodman,^{73,51} R. Rosenfeld,^{89,4} A. J. Ross,⁵⁸ E. Rozo,⁶³ E. S. Rykoff,^{73,51} S. Samuroff,^{19,31} C. Sánchez,^{90,31} E. Sanchez,¹¹ D. Sanchez Cid,^{11,10} T. Schutt,^{72,73,51} I. Sevilla-Noarbe,¹¹ E. Sheldon,²³ N. Sherman,⁹¹ T. Shin,⁹² M. Smith,⁹³ M. Soares-Santos,¹⁰ E. Suchyta,⁹⁴ M. E. C. Swanson,² M. Tabbutt,¹⁴ G. Tarle,⁷ D. Thomas,¹² C. To,³⁶ A. Tong,^{16,71} L. Toribio San Cipriano,¹¹ M. A. Troxel,⁷¹ M. Tsedrik,^{33,36} D. L. Tucker,⁶ V. Vikram,⁹⁵ A. R. Walker,¹ N. Weaverdyck,^{96,41} R. H. Wechsler,^{72,73,51} D. H. Weinberg,^{58,97} J. Weller,^{98,99} V. Wetzell,¹⁶ A. Whyley,¹² R.D. Wilkinson,⁵³ P. Wiseman,¹⁰⁰ H.-Y. Wu,⁵⁹ M. Yamamoto,^{8,71} B. Yanny,⁶ B. Yin,⁷¹ G. Zacharegkas,⁹ Y. Zhang,¹ and J. Zuntz¹⁰¹
(DES Collaboration)

¹Cerro Tololo Inter-American Observatory, NSF's National Optical-Infrared Astronomy Research Laboratory, Casilla 603, La Serena, Chile²Center for Astrophysical Surveys, National Center for Supercomputing Applications, 1205 West Clark St., Urbana, IL 61801, USA³INAF-Osservatorio Astronomico di Trieste, via G. B. Tiepolo 11, I-34143 Trieste, Italy⁴Laboratório Interinstitucional de e-Astronomia - LIneA, Av. Pastor Martin Luther King Jr, 126 Del Castilho, Nova América Offices, Torre 3000/sala 817 CEP: 20765-000, Brazil⁵Institute of Space Sciences (ICE, CSIC), Campus UAB, Carrer de Can Magrans, s/n, 08193 Barcelona, Spain⁶Fermi National Accelerator Laboratory, P. O. Box 500, Batavia, IL 60510, USA⁷Department of Physics, University of Michigan, Ann Arbor, MI 48109, USA⁸Department of Astrophysical Sciences, Princeton University, Peyton Hall, Princeton, NJ 08544, USA⁹Kavli Institute for Cosmological Physics, University of Chicago, Chicago, IL 60637, USA¹⁰Physik-Institut, University of Zürich, Winterthurerstrasse 190, CH-8057 Zürich, Switzerland¹¹Centro de Investigaciones Energéticas, Medioambientales y Tecnológicas (CIEMAT), Madrid, Spain¹²Institute of Cosmology and Gravitation, University of Portsmouth, Portsmouth, PO1 3FX, UK¹³Institute for Astronomy, University of Hawai'i, 2680 Woodlawn Drive, Honolulu, HI 96822, USA¹⁴Physics Department, 2320 Chamberlin Hall, University of Wisconsin-Madison, 1150 University Avenue Madison, WI 53706-1390¹⁵Argonne National Laboratory, 9700 South Cass Avenue, Lemont, IL 60439, USA¹⁶Department of Physics and Astronomy, University of Pennsylvania, Philadelphia, PA 19104, USA¹⁷CNRS, UMR 7095, Institut d'Astrophysique de Paris, F-75014, Paris, France¹⁸Sorbonne Universités, UPMC Univ Paris 06, UMR 7095,¹⁹Institut d'Astrophysique de Paris, F-75014, Paris, France²⁰Department of Physics, Northeastern University, Boston, MA 02115, USA²¹University Observatory, LMU Faculty of Physics, Scheinerstr. 1, 81679 Munich, Germany²²Department of Physics & Astronomy, University College London, Gower Street, London, WC1E 6BT, UK²³Center for Astrophysics | Harvard & Smithsonian, 60 Garden Street, Cambridge, MA 02138, USA²⁴Brookhaven National Laboratory, Bldg 510, Upton, NY 11973, USA²⁵School of Mathematics and Physics, University of Queensland, Brisbane, QLD 4072, Australia²⁶Department of Physics, University of Genova and INFN, Via Dodecaneso 33, 16146, Genova, Italy²⁷Department of Physics, Carnegie Mellon University, Pittsburgh, Pennsylvania 15312, USA²⁷NSF AI Planning Institute for Physics of the Future,²⁷Carnegie Mellon University, Pittsburgh, PA 15213, USA

²⁸*Instituto de Astrofísica de Canarias, E-38205 La Laguna, Tenerife, Spain*
²⁹*Universidad de La Laguna, Dpto. Astrofísica, E-38206 La Laguna, Tenerife, Spain*
³⁰*Department of Astronomy, University of Illinois at Urbana-Champaign, 1002 W. Green Street, Urbana, IL 61801, USA*
³¹*Institut de Física d'Altes Energies (IFAE), The Barcelona Institute of Science and Technology, Campus UAB, 08193 Bellaterra (Barcelona) Spain*
³²*Centre for Astrophysics Research, University of Hertfordshire, College Lane, Hatfield AL10 9AB, UK*
³³*Institute for Astronomy, The University of Edinburgh, Royal Observatory, Edinburgh EH9 3HJ, UK*
³⁴*Institut d'Estudis Espacials de Catalunya (IEEC), 08034 Barcelona, Spain*
³⁵*Oxford College of Emory University, Oxford, GA 30054, USA*
³⁶*Department of Astronomy and Astrophysics, University of Chicago, Chicago, IL 60637, USA*
³⁷*NASA Goddard Space Flight Center, 8800 Greenbelt Rd, Greenbelt, MD 20771, USA*
³⁸*Astronomy Unit, Department of Physics, University of Trieste, via Tiepolo 11, I-34131 Trieste, Italy*
³⁹*Institute for Fundamental Physics of the Universe, Via Beirut 2, 34014 Trieste, Italy*
⁴⁰*Hamburger Sternwarte, Universität Hamburg, Gojenbergsweg 112, 21029 Hamburg, Germany*
⁴¹*Lawrence Berkeley National Laboratory, 1 Cyclotron Road, Berkeley, CA 94720, USA*
⁴²*Université Grenoble Alpes, CNRS, LPSC-IN2P3, 38000 Grenoble, France*
⁴³*Department of Astronomy/Steward Observatory, University of Arizona, 933 North Cherry Avenue, Tucson, AZ 85721-0065, USA*
⁴⁴*Jet Propulsion Laboratory, California Institute of Technology, 4800 Oak Grove Dr, Pasadena, CA 91109, USA*
⁴⁵*Department of Physics and Astronomy, University of Waterloo, 200 University Ave W, Waterloo, ON N2L 3G1, Canada*
⁴⁶*California Institute of Technology, 1200 East California Blvd, MC 249-17, Pasadena, CA 91125, USA*
⁴⁷*Department of Astronomy, University of Michigan, Ann Arbor, MI 48109, USA*
⁴⁸*Physics Department, William Jewell College, Liberty, MO 64068, USA*
⁴⁹*Departments of Statistics and Data Sciences, University of Texas at Austin, Austin, TX 78757, USA*
⁵⁰*NSF-Simons AI Institute for Cosmic Origins, University of Texas at Austin, Austin, TX 78757, USA*
⁵¹*SLAC National Accelerator Laboratory, Menlo Park, CA 94025, USA*
⁵²*Instituto de Física Teórica UAM/CSIC, Universidad Autónoma de Madrid, 28049 Madrid, Spain*
⁵³*Department of Physics and Astronomy, Pevenssey Building, University of Sussex, Brighton, BN1 9QH, UK*
⁵⁴*Centre for Astrophysics & Supercomputing, Swinburne University of Technology, Victoria 3122, Australia*
⁵⁵*School of Physics and Astronomy, Cardiff University, CF24 3AA, UK*
⁵⁶*Department of Astronomy, University of Geneva, ch. d'Écogia 16, CH-1290 Versoix, Switzerland*
⁵⁷*Santa Cruz Institute for Particle Physics, Santa Cruz, CA 95064, USA*
⁵⁸*Center for Cosmology and Astro-Particle Physics, The Ohio State University, Columbus, OH 43210, USA*
⁵⁹*Department of Physics, The Ohio State University, Columbus, OH 43210, USA*
⁶⁰*Department of Physics, ETH Zurich, Wolfgang-Pauli-Strasse 16, CH-8093 Zurich, Switzerland*
⁶¹*MTA-CSFK Lendület "Momentum" Large-Scale Structure (LSS) Research Group, Konkoly Thege Miklós út 15-17, H-1121 Budapest, Hungary*
⁶²*Konkoly Observatory, HUN-REN Research Centre for Astronomy and Earth Sciences, Konkoly Thege Miklós út 15-17, H-1121 Budapest, Hungary*
⁶³*Department of Physics, University of Arizona, Tucson, AZ 85721, USA*
⁶⁴*Australian Astronomical Optics, Macquarie University, North Ryde, NSW 2113, Australia*
⁶⁵*Lowell Observatory, 1400 Mars Hill Rd, Flagstaff, AZ 86001, USA*
⁶⁶*Department of Physics and Astronomy, Ohio University, Clippinger Labs, Athens, OH 45701, USA*
⁶⁷*Centre for Gravitational Astrophysics, College of Science, The Australian National University, ACT 2601, Australia*
⁶⁸*The Research School of Astronomy and Astrophysics, Australian National University, ACT 2601, Australia*
⁶⁹*Department of Applied Mathematics and Theoretical Physics, University of Cambridge, Cambridge CB3 0WA, UK*
⁷⁰*George P. and Cynthia Woods Mitchell Institute for Fundamental Physics and Astronomy, and Department of Physics and Astronomy, Texas A&M University, College Station, TX 77843, USA*
⁷¹*Department of Physics, Duke University Durham, NC 27708, USA*
⁷²*Department of Physics, Stanford University, 382 Via Pueblo Mall, Stanford, CA 94305, USA*
⁷³*Kavli Institute for Particle Astrophysics & Cosmology, P. O. Box 2450, Stanford University, Stanford, CA 94305, USA*
⁷⁴*Aix Marseille Univ, CNRS/IN2P3, CPPM, Marseille, France*
⁷⁵*Institució Catalana de Recerca i Estudis Avançats, E-08010 Barcelona, Spain*
⁷⁶*Department of Physics, University of Cincinnati, Cincinnati, Ohio 45221, USA*
⁷⁷*Perimeter Institute for Theoretical Physics, 31 Caroline St. North, Waterloo, ON N2L 2Y5, Canada*
⁷⁸*School of Mathematics and Physics, University of Surrey, Guildford, UK, GU2 7HX*
⁷⁹*Centro de Tecnología da Informação Renato Archer, Campinas, SP, Brazil - 13069-901*
⁸⁰*Observatório Nacional, Rio de Janeiro, RJ, Brazil - 20921-400*
⁸¹*Observatório Nacional, Rua Gal. José Cristino 77, Rio de Janeiro, RJ - 20921-400, Brazil*
⁸²*Ruhr University Bochum, Faculty of Physics and Astronomy, Astronomical Institute, German Centre for Cosmological Lensing, 44780 Bochum, Germany*

⁸³*Higgs Centre for Theoretical Physics, School of Physics and Astronomy,*

The University of Edinburgh, Edinburgh EH9 3FD, UK

⁸⁴*Nordita, KTH Royal Institute of Technology and Stockholm University,*

Hannes Alfvéns väg 12, SE-10691 Stockholm, Sweden

⁸⁵*Institute of Astronomy, University of Cambridge, Madingley Road, Cambridge CB3 0HA, UK*

⁸⁶*Instituto de Física Teórica UAM/CSIC, Universidad Autónoma de Madrid, 28049 Madrid, Spain*

⁸⁷*Laboratoire de physique des 2 infinis Irène Joliot-Curie,*

CNRS Université Paris-Saclay, Bât. 100, F-91405 Orsay Cedex, France

⁸⁸*McWilliams Center for Cosmology and Astrophysics, Department of Physics,*

Carnegie Mellon University, Pittsburgh, PA 15213, USA

⁸⁹*ICTP South American Institute for Fundamental Research*

Instituto de Física Teórica, Universidade Estadual Paulista, São Paulo, Brazil

⁹⁰*Departament de Física, Universitat Autònoma de Barcelona (UAB), 08193 Bellaterra, Barcelona, Spain*

⁹¹*Institute for Astrophysical Research, Boston University, 725 Commonwealth Avenue, Boston, MA 02215, USA*

⁹²*Department of Physics and Astronomy, Stony Brook University, Stony Brook, NY 11794, USA*

⁹³*Physics Department, Lancaster University, Lancaster, LA1 4YB, UK*

⁹⁴*Computer Science and Mathematics Division, Oak Ridge National Laboratory, Oak Ridge, TN 37831*

⁹⁵*Central University of Kerala, Kasaragod, Kerala, India 671325*

⁹⁶*Berkeley Center for Cosmological Physics, Department of Physics, University of California, Berkeley, CA 94720, US*

⁹⁷*Department of Astronomy Ohio State University, Columbus, OH 43210*

⁹⁸*Max Planck Institute for Extraterrestrial Physics, Giessenbachstrasse, 85748 Garching, Germany*

⁹⁹*Universitäts-Sternwarte, Fakultät für Physik, Ludwig-Maximilians Universität München, Scheinerstr. 1, 81679 München, Germany*

¹⁰⁰*School of Physics and Astronomy, University of Southampton, Southampton, SO17 1BJ, UK*

¹⁰¹*Institute for Astronomy, University of Edinburgh, Edinburgh EH9 3HJ, UK*

(Dated: January 22, 2026)

We present cosmology results combining galaxy clustering and weak gravitational lensing measured in the full six years (Y6) of observations by the Dark Energy Survey (DES) covering $\sim 5000 \text{ deg}^2$. We perform a large-scale structure analysis with galaxy samples defined from the final data extending to redshift range $z \lesssim 2$, using three two-point correlation functions ($3 \times 2\text{pt}$): (i) cosmic shear measuring correlations among the shapes of 140 million source galaxies, (ii) auto-correlations of the spatial distribution of 9 million lens galaxies, and (iii) galaxy-galaxy lensing from the cross-correlation between lens positions and source shapes. We perform the analysis under a rigorous blinding protocol to prevent confirmation biases. We model the data in flat ΛCDM and $w\text{CDM}$ cosmologies. We find consistent cosmological results from subsets of the three two-point correlation functions. Their combined analysis yields $S_8 \equiv \sigma_8(\Omega_m/0.3)^{0.5} = 0.789^{+0.012}_{-0.012}$ and matter density $\Omega_m = 0.333^{+0.023}_{-0.028}$ in ΛCDM (68% CL), where σ_8 is the clustering amplitude. The factor of two improvement in constraining power in the $\Omega_m-\sigma_8$ plane relative to DES Year 3 is due to higher source number density, extended redshift range, and improved modeling. These constraints show a (full-space) parameter difference of 1.8σ from a combination of cosmic microwave background (CMB) primary anisotropy datasets from *Planck* 2018, ACT-DR6, and SPT-3G DR1. Projected only into S_8 the difference is 2.6σ . In $w\text{CDM}$ the Y6 $3 \times 2\text{pt}$ results yield $S_8 = 0.782^{+0.021}_{-0.020}$, $\Omega_m = 0.325^{+0.032}_{-0.035}$, and dark energy equation-of-state parameter $w = -1.12^{+0.26}_{-0.20}$. For the first time, we combine all DES dark-energy probes: $3 \times 2\text{pt}$, SNe Ia, BAO and Clusters. In ΛCDM this combination yields a 2.8σ parameter difference from the CMB. When combining DES $3 \times 2\text{pt}$ with other most constraining low-redshift datasets (DESI DR2 BAO, DES SNe Ia, SPT clusters), we find a 2.3σ parameter difference with CMB. A joint fit of Y6 $3 \times 2\text{pt}$, CMB, and those low- z datasets produces the tightest ΛCDM constraints to date: $S_8 = 0.806^{+0.006}_{-0.007}$, $\Omega_m = 0.302^{+0.003}_{-0.003}$, $h = 0.683^{+0.003}_{-0.002}$, and $\sum m_\nu < 0.14 \text{ eV}$ (95% CL). In $w\text{CDM}$, this dataset combination yields $w = -0.981^{+0.021}_{-0.022}$, with no significant preference over ΛCDM .

I. INTRODUCTION

The concordance model of cosmology posits that the universe is well described by General Relativity and is composed of $\sim 5\%$ baryons, $\sim 25\%$ cold dark matter (CDM) and $\sim 70\%$ dark energy. The nature of dark matter is largely unknown aside from the fact that it interacts gravitationally, but it is canonical to assume that it is non-relativistic and only weakly interacting (CDM). The nature of dark energy is even less constrained—typically, it is assumed to be either a cosmological constant (Λ) or describable as an effective fluid with equation of state parameter w . In this paper, we analyze and compare results in the context of two cosmological models,

the standard ΛCDM paradigm and $w\text{CDM}$, where in the latter case w is assumed to be constant in time but can differ from the ΛCDM value of $w = -1$. Most previous analyses of data in the context of these two models [1–10] have found results consistent with $w = -1$, i.e., with ΛCDM . A separate paper [11] will consider DES constraints in the context of models with time-varying w , which have garnered considerable recent interest [12–14].

The Dark Energy Survey (DES; [15]) was developed to test the ΛCDM paradigm and probe the nature of dark energy through a combination of cosmological probes. Between 2013 and 2019, DES imaged $\sim 1/8$ th of the sky to leverage information encoded in the large-scale structure (LSS) of galaxies and

TABLE I. Reference table for supporting papers to this work.

Shorthand	Reference	Description
Y6GOLD	[17]	Coadd object catalog and associated products
Y6BALROG	[18]	Synthetic source injection
Y6PSF	[19]	Point spread function (PSF) models
Y6MASK	[20]	Survey mask
Y6SHEAR	[21]	METADECTECT shear catalog
Y6POS	[22]	MAGLIM++ lens selection and galaxy clustering
Y6SHEARPZ	[23]	Source photo- z calibration
Y6POSPZ	[24]	Lens photo- z calibration
Y6WZ	[25]	Clustering redshift
Y6MODE	[26]	Method for marginalizing redshift uncertainty
Y6IMSIM	[27]	Image simulation
Y6MOCK	[28]	Mock galaxy catalog
Y6MODEL	[29]	Modeling and analysis choices
Y6MAG	[30]	Characterising lens magnification
Y6PPD	[31]	Quantifying internal consistency with posterior predictive distribution
Y6GGL	[32]	Galaxy-galaxy lensing
Y6-1x2PT	[33]	Cosmology from cosmic shear
Y6-2x2PT	[34]	Cosmology from galaxy-galaxy lensing and galaxy clustering

matter, as well as a large number of other science goals [16]. This paper presents the LSS analysis from the full six years of DES data (DES Y6), combining measurements of the galaxy angular overdensity field δ_g and the weak gravitational lensing shear field γ , which measures the coherent distortion of galaxy shapes caused by deflection of light by the cosmic mass distribution. In particular, we perform a 3×2 pt analysis, which uses two distinct galaxy samples to measure three complementary 2-point correlation functions. The *source sample* consists of galaxies selected for shape measurements to quantify weak lensing shear, whereas the *lens sample* comprises galaxies whose positions trace the large-scale matter distribution. The three correlation functions are: the auto-correlation of galaxy shear, $\xi_{\pm} = \langle \gamma\gamma \rangle$, often referred to as cosmic shear; the correlation between galaxy density and shear, $\gamma_t = \langle \delta_g \gamma \rangle$, often referred to as galaxy-galaxy lensing; and the auto-correlation of galaxy density, $w = \langle \delta_g \delta_g \rangle$, or galaxy clustering.

The combination of galaxy clustering with weak gravitational lensing was proposed by [35] in 2004 as a way to increase sensitivity relative to weak lensing alone. Jointly analyzing these three probes allows the data to self-calibrate astrophysical and nuisance parameters, resulting in tighter and more robust cosmological constraints. This technique was first applied to data in the first-year DES cosmology analysis (DES Y1) [36], and was later built upon in the DES three-year analysis (DES Y3) [37]. Many improvements in data quality, data quantity, and methodology have been implemented for successive DES analyses. The major methodological changes from Y3 to the present Y6 analysis are summarized in Appendix F.

Other collaborations have conducted 3×2 pt analyses on multi-survey data, relying on overlapping spectroscopic lens

samples. The Kilo-Degree Survey¹ [KiDS 38, 39] presented in [39] a 3×2 pt analysis using a combination of the KiDS-1000 shear catalog and lenses from the Baryon Oscillation Spectroscopic Survey (BOSS) and spectroscopic 2-degree Field Lensing Survey (2dFLenS). The most up-to-date KiDS shear analysis was recently presented in [7], and its extension to 3×2 pt is currently ongoing. The Hyper Suprime-Cam Subaru Strategic Program² [HSC-SSP, 40–42] carried out a 3×2 pt analysis in [43–45] using the HSC Year 3 shear catalog and the SDSS DR11 spectroscopic galaxies.

This paper presents constraints from DES Y6 3×2 pt statistics on a baseline 6-parameter flat Λ CDM model and its extension to $w \neq -1$ (w CDM). These results build on two papers that present subsets of the 3×2 pt probes: [Y6-1x2PT] carries out a detailed analysis using only cosmic shear (1×2 pt), while [Y6-2x2PT] investigates the combination of galaxy-galaxy lensing and galaxy clustering probes (2×2 pt). We also present cosmological constraints by combining DES Y6 3×2 pt results with those from other DES cosmological probes. In particular, we present results from the combination of four dark energy probes using the DES dataset: Y6 3×2 pt (this work) and previous measurements of supernovae type Ia (SNe Ia) [12], galaxy clusters [46], and baryon acoustic oscillation (BAO) [47]. A follow-up paper [48] will update the analysis of galaxy clusters using DES Y6 data, completing the final internal combination that was envisioned in the design of DES.

In this paper we also analyze combinations of the DES Y6 3×2 pt results with state-of-the-art external probes and assess the consistency between them. Future work in [11] will use the DES Y6 data discussed in this paper to explore alternative cosmological models such as modified gravity and evolving dark energy. Further followup papers will present cosmological constraints using different lens and/or source samples and differing sets of summary statistics.

This paper is organized as follows. In Section II we describe the DES Y6 data used in this work. In Section III we present the measurements of the data vector. In Section IV we describe the modeling framework and analysis choices. We present our main 3×2 pt results in Section V, combine with other DES probes in Section VI, and combine with external probes in Section VII. We conclude in Section VIII. The DES Y6 cosmological constraints build on a series of 18 supporting papers³, and references within, that develop the individual components that go into the final cosmological inferences. To ease the reader’s navigation, this paper refers to the supporting papers with the labels listed in Table I.

¹ <http://kids.strw.leidenuniv.nl/>

² <https://www.naoj.org/Projects/HSC/>

³ Some of these papers are still in preparation, but are expected to be published in the near future.

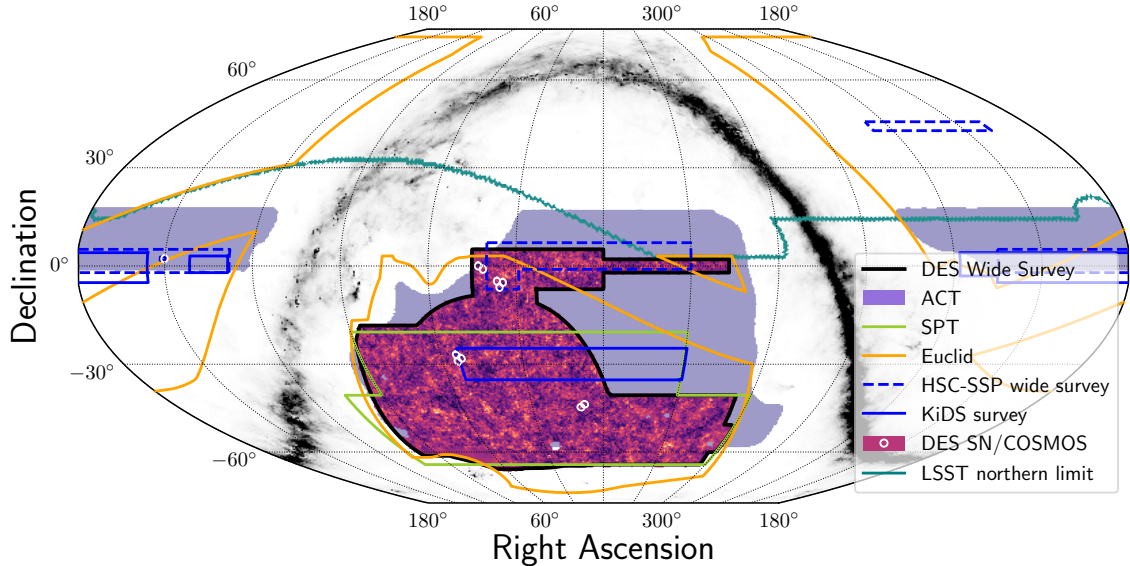


FIG. 1. DES footprint in equatorial coordinates. The $\sim 5000 \text{ deg}^2$ wide-field survey footprint is shown as a black outline, with overplotted convergence map using the Wiener filter reconstruction method [49]. The white circles, scaled to approximately one full DECam field-of-view, show the supernovae field locations. Other current and planned surveys are shown as well. The South Pole Telescope footprint includes the SPTpol and SPT-SZ surveys described in [50].

II. THE DARK ENERGY SURVEY YEAR 6 DATA PRODUCTS

A. Y6 Gold Catalog

DES was allocated 760 distinct full- or half-nights of observations between 2013 August 15 and 2019 January 9 [51] to use the Dark Energy Camera (DECam; [52, 53]), a 570-megapixel camera with a 3 deg^2 field-of-view installed at the prime focus of the 4-meter Víctor M. Blanco Telescope at Cerro Tololo Inter-American Observatory (CTIO) in Chile. The DES wide-field survey observed in five broad bands, $grizY$, spanning $400 \text{ nm} \lesssim \lambda \lesssim 1060 \text{ nm}$. The final DES data release, DES Data Release 2 (DES DR2; [54]), includes 76,217 DECam exposures from the wide-field survey in the $grizY$ bands that passed baseline survey quality criteria. The image reduction, detrending, and processing for DES DR2 were performed using the DES Data Management system at NCSA [55], with the configuration described in [54].

DES DR2 is used to produce the DES Y6 Gold data collection, which serves as the basis for most cosmological analyses with the DES wide-field survey data [Y6GOLD]. Y6 Gold augments DES DR2 with value-added information including survey systematics maps, improved multi-epoch photometry, and catalog quality flags. The DES Y6 Gold catalog contains 669 million objects spanning $4,923 \text{ deg}^2$ of the sky with a median coadd depth of $i = 23.8$ mag, defined as the magnitude corresponding to a $S/N = 10$ in 1.95 arcsec diameter apertures [54]. Each galaxy in the Y6 Gold sample is assigned

a photometric redshift estimate, z_{DNF} , via the Directional Neighbourhood Fitting (DNF; [56]) method. The cosmology analyses also make use of deeper catalogs by assembling coadded images from exposures in the DES supernovae (SN) fields [57], which were then used to seed synthetic source injection studies using the BALROG software [18, 58, 59]. Figure 1 shows the sky footprint of the DES wide survey and the locations of the DES deep fields (DES SN/COSMOS).

B. Source galaxies

The DES Y6 shear catalog [Y6SHEAR] is constructed by applying METADETECTION [60] to cell-based coadded images (e.g., [61]). The principle of METADETECTION is to produce five shear catalogs for each coadd cell (of size 200×200 pixels): one from the unsheared image, and two with positive and negative synthetic shears applied to the image in each of the spin-2 axes; $\pm e_1, \pm e_2$. A nominal shear estimator is applied to each variant image; the variation of the measurement under synthetic shear is used to calculate the response factor $\langle R \rangle$ of the nominal estimator to γ in each tomographic bin. Due to detecting objects on cell-based coadds, the METADETECTION catalog does not map onto the Gold catalog. We make similar quality selections as when constructing the Gold catalog, however, to ensure the quality of photometric redshifts (see Section 3.1 of [Y6SHEARPZ]), and to make a common selection of regions between lens and source samples [see Y6MASK, Y6SHEAR]. This leaves

TABLE II. Characteristics of the source and lens samples. For each tomographic source bin and their union, we list the mean redshift, number of objects, effective number density, shape noise, shear response and weighted residual mean shear. For lens bins we give the mean redshift, number of objects and number density for the lens sample.

Bin	Source sample							Lens sample		
	$\langle z_s \rangle$	num. of objects	n_{eff} [gals/arcmin 2]	σ_e	$\langle R \rangle$	$\langle e_1 \rangle \times 10^{-4}$	$\langle e_2 \rangle \times 10^{-4}$	$\langle z_l \rangle$	num. of objects	n_{gal} [gals/arcmin 2]
1	0.414	33,707,071	2.05	0.265	0.856	+1.6	+0.62	0.306	1,852,538	0.128
2	0.538	34,580,888	2.10	0.287	0.869	+0.45	-0.58	0.435	1,335,294	0.092
3	0.846	34,646,416	2.14	0.282	0.819	+2.4	-1.7	0.624	1,413,738	0.097
4	1.157	36,727,798	2.32	0.347	0.692	+3.1	+1.1	0.778	1,783,834	0.123
5	-	-	-	-	-	-	-	0.903	1,391,521	0.096
6	-	-	-	-	-	-	-	1.011	1,409,280	0.097
All		139,662,173	8.29	0.289	0.819	+1.4	-0.15		9,186,205	0.633

139,881,005 galaxies with the effective number density $n_{\text{eff}} = 8.29$ galaxies/arcmin 2 and shape noise (which includes the intrinsic ellipticity dispersion) $\sigma_e = 0.289$. Table II summarizes the shear responses, mean densities, and shear noise levels for each tomographic bin.

METADETECTION shear estimations make use of PSF models created with the PiFF software [62]. The PSF models for Y6 newly incorporate the chromatic dependence of the PSF, significantly reducing modeling errors in all *griz* bands [Y6PSF]. However, due to residual modeling errors in *g*-band, shapes measured on *g*-band images are not suitable for cosmology, but the fluxes are less affected. We therefore use the *g*-band fluxes for better photometric redshift estimates in addition to *riz* fluxes.

The cosmological inferences include nuisance parameters to marginalize over multiplicative biases m in the METADETECTION shear estimators. Residual additive biases c (measured as the weighted mean shear, see Table II) are subtracted empirically. Priors on m in each source bin are estimated by building a suite of image simulations that mimic our DES images, then processing them through the same measurement pipeline as the data. The simulations are particularly important for quantifying the effect of blended galaxies (i.e., overlapping) galaxies in the images, for which the apparent shape of the observed light profile is subject to the weak lensing shear applied at two different redshifts. The Y6 image simulations [Y6IMSIM] improve upon those from [63] in several ways: the simulations include a more realistic distribution of stars, the galaxies include a redshift-dependent clustering signal informed by an N -body simulation [Y6MOCK], and the determination of the calibration accounts for the full covariance between shear and redshift distribution calibration parameters. This last improvement is especially important in Y6, with its higher rate of blending relative to Y3.

C. Lens galaxies

The lens sample used in this work is the MAGLIM++ sample described in [Y6POS]. MAGLIM++ is designed to balance shot-noise against redshift resolution; we do this by selecting

galaxies with *i*-band magnitudes restricted to [64]:

$$17.5 < i < 18 + 4 \times z_{\text{DNF}}. \quad (1)$$

Two additional cuts reduce systematic contamination from stars and other interlopers. First, a redshift-bin optimized star-galaxy classifier [65] leverages near-infrared unWISE [66, 67] data to identify optimal color cuts in $(r - z, z - W1)$ space for each bin, complementing the GOLD morphological classifier [Y6GOLD] and removing [1.1, 0.6, 2.0, 3.3, 3.2, 1.3)% of objects as residual stellar contamination across redshift bins. Second, a selection in the space of a self-organized map (SOM) of the *griz* color space removes objects occupying compact regions with large photo- z dispersion, due to either color-redshift degeneracies or training data limitations. This removes an additional 1.66% of objects, primarily QSOs. The final number density of lens galaxies in each bin is listed in Table II. These number densities are significantly smaller than those of the sources due to the need for a higher photometric redshift accuracy for galaxy clustering.

The observed galaxy density is modulated by spatially-varying observing conditions or survey properties, which modify the detection probability. For example, regions of high dust extinction often have fewer detected galaxies in them; other examples of these varying survey properties include variations due to changing observing conditions such as seeing and sky noise. To mitigate the impact of these, each galaxy is assigned a weight constructed from template maps of the spatially-varying survey properties. Two different weights methods are used—(ENET [68] and ISD [69])—and the covariance matrix for the $w(\theta)$ measurements incorporates analytic marginalization over the results of these methods.

D. Tomographic bin assignment

We select lens galaxies in six disjoint z_{DNF} ranges to form bins in which we measure their δ_g fields. Note that we use the z_{DNF} values only for bin assignment; the redshift distributions $n(z)$ of each bin's members are determined by fully distinct methods, described in Section II E. We select four disjoint bins of source galaxies to use for tomographic estimation

of the weak lensing shear γ . We select galaxies into these bins by using a SOM to compress their $griz$ fluxes into a two-dimensional grid of cells. This grid is further partitioned into four sets of cells according to the mean redshift estimated for each cell (see Section II E) to form roughly equipopulated bins (see Table II).

E. Photometric redshift distributions

Estimates of the redshift distribution $n^i(z)$ for each tomographic bin i are required to model the 3×2 pt signal (see Section IV A). The $n(z)$ estimations for source bins are described in [Y6SHEARPZ], and for lens bins in [Y6POSPZ]. Each uses a hybrid framework combining photometry information (SOMPZ) and clustering information (WZ) [Y6WZ].

The SOMPZ process begins with photometry from the DES deep fields [57], a sample of 1.68 million galaxies spanning 5.88 deg^2 over four different fields (Figure 1). This deep data combines (i) $10 \times$ the depth of the wide-field coadded images with (ii) extended wavelength coverage from DES u -band and near-infrared JHK imaging provided by overlapping VIDEO [70] or UltraVISTA [71] observations and (iii) highly accurate redshift information, primarily from spectroscopic and multi-band photometric data in the COSMOS field. Using the 8-band fluxes of deep-field galaxies that are bright enough to be detected in the wide-field survey, we construct a 2D SOM. The redshift distribution of each cell is constrained by its associated deep-field galaxies with high-quality spectroscopy [72–79] or many-band photo- z from COSMOS [80] or PAUS [81, 82].

A distinct two-dimensional SOM is constructed for the wide-field galaxies, using 4 bands ($griz$) instead of 8. We want the “transfer function” giving the probability that members of a given deep-SOM cell will be assigned to each wide-SOM cell when observed in the DES wide-field survey. This is measured using the synthetic-source catalog created by the BALROG process [Y6BALROG]: each galaxy in the BALROG catalog is a model of a true deep field galaxy that has been added into the wide-field $griz$ images and measured with the wide-field pipeline. The BALROG transfer function then allows mapping the redshift distributions of the deep-field SOM cells into an $n(z)$ estimate for the collection of wide-field SOM cells that comprise a given source or lens galaxy bin.

The SOMPZ derivation of the $n(z)$ s is realized many times by sampling over uncertainties in COSMOS and PAUS photometric redshift assignments, over the uncertainties in the relative photometric calibrations of the deep fields, and over sample variance in the limited area of both the deep and redshift samples. For the source galaxies, the dominant uncertainty contribution comes from imperfections in the redshift sample, primarily due to the lack of representative spectra of faint galaxies. For the lens galaxies there is no single source of uncertainty clearly dominating across all tomographic bins. As described in [Y6WZ], the SOMPZ realizations are importance-sampled by the likelihood that each $n(z)$ realization would reproduce the observed correlations $w(\theta, z)$ against spectroscopic galaxies in several intervals of

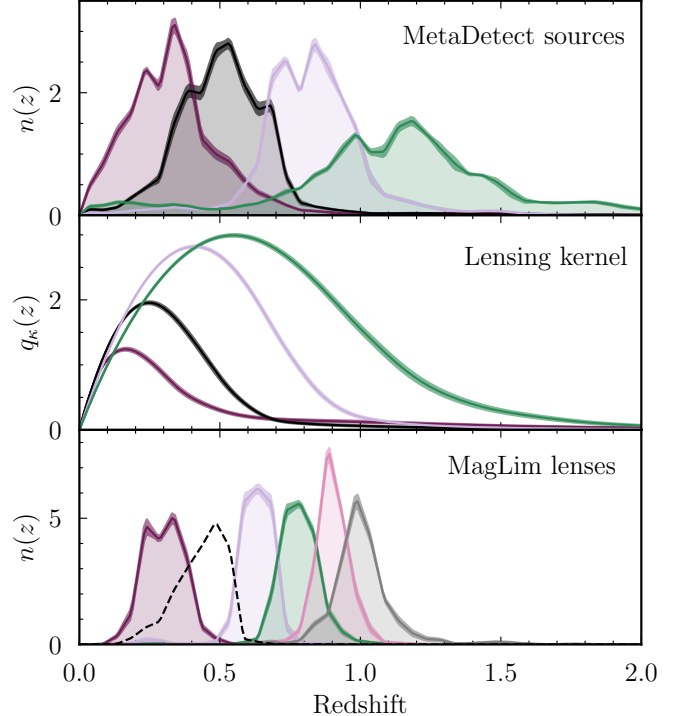


FIG. 2. Estimated redshift distributions of the Y6 source (top) and lens (bottom) samples. Different colors represent different tomographic bins. The middle panel shows the lensing efficiency (Equation 11) for each source bin. In each case, the solid lines and band represent the mean and standard distribution of 100 $n(z)$ reconstructions, drawn from the posterior of our fiducial 3×2 pt linear bias analysis. Note that lens bin 2 is unshaded because it is excluded from our fiducial analysis (see Appendix A for details).

z [Y6WZ]. The correlations used in the clustering redshift method, WZ, are limited to angular scales that are smaller than those used in the fiducial 3×2 pt cosmological analysis. The entire process yields samples of $n(z)$ that are drawn from the joint SOMPZ+WZ likelihood.

Multiplicative shear calibration m is coupled with redshift calibration through blending, and both are incorporated at the level of the source redshift distributions. This is represented by an effective sheared redshift distribution, $n_\gamma^i := R^i(z) n^i(z)$, where the redshift dependence of the response matrix is evaluated using image simulations [Y6IMSIM]. Since $n_\gamma^i(z)$ are not, in general, normalized, we introduce multiplicative shear bias coefficients $m^i = \int n_\gamma^i(z) dz - 1$, such that

$$n_\gamma^i = (1 + m^i) n_{\gamma, \text{norm}}^i(z). \quad (2)$$

The new normalized effective sheared distributions can differ significantly from the original $n(z)$ distributions with mean- z shift for each bin: $-0.013, -0.021, -0.002, -0.034$ [Y6IMSIM]. In the rest of this work, we use the normalized effective sheared source redshift distributions, but we omit the γ notation.

To efficiently marginalize over redshift uncertainties in the cosmological inference, we apply a mode projection approach

[Y6MODES] to these samples. The ensemble of SOMPZ+WZ redshift realizations are decomposed into linear sums of components $U^{i,\beta}(z)$ that capture the directions of largest cosmological impact:

$$n^i(z) = \bar{n}^i(z) + \sum_{\beta} u^{\beta} U^{i,\beta}(z), \quad (3)$$

where u^{β} are the mode amplitudes that are being marginalized over. We find that a total of seven β modes are sufficient to describe all variations seen in the SOMPZ+WZ samples of the four source bins' $n^i(z)$ that have the capacity to produce detectable variations in the $3 \times 2\text{pt}$ statistics [Y6SHEARPZ]. For each lens bin, three modes are found sufficient to specify any detectable influence on the observables [Y6POSPZ]. In total, 25 nuisance coefficients u^{β} specify the uncertainties in the SOMPZ+WZ estimations of $n^i(z)$ for the 10 source and lens bins. The modes are constructed such that each u^{β} has a prior with zero mean and unit variance. In most cases the priors are normal distributions; for a few of the u^{β} , these are detectably non-Gaussian, but a simple transformation of variables renders the prior Gaussian again [Y6MODES].

We make a final joint adjustment to the priors on the multiplicative shear errors m^i and the redshift mode coefficients u^{β} to make the shear measurement model consistent with the effects of galaxy blending measured in the image simulations. This correction, as described in [Y6IMSIM] and [Y6SHEARPZ], results in a prior with small non-zero covariances among the m^i and u^{β} .

We further validate our redshift calibration using the shear ratio (SR) test [83], by taking the ratio of galaxy-galaxy lensing using the same lens and different source bins. As described in [Y6GGL], we use non-overlapping lens-source pairs to ensure the approximation of geometric ratios holds, where the evolution of lens properties within the lens bins is ignored. This results in us using the two lowest lens bins and the two highest source bins. This ensures SR is sensitive only to redshift and shear calibration, while being complementary at higher redshift to the information in the galaxy clustering constraint. We find that our SR result is consistent with SOMPZ + WZ + blending.

The final redshift distributions for the source and lens samples reconstructed by the modes are shown in the top and bottom panel of Figure 2, respectively.

III. TWO-POINT MEASUREMENTS

From the galaxy positions in the lens sample and the shear and position of galaxies in the source sample, we measure three projected two-point correlation functions.

1. The angular two-point function $w^{ij}(\theta)$ between positions of lens galaxies in redshift bins i and j , measured by comparing counts of galaxy pairs separated by angular separation θ to the number of random-point pairs. We retain only auto-correlations, discarding measurements where $i \neq j$. The $w^{ij}(\theta)$ estimator, its measurement, and validation process are described in detail in [Y6POS].

2. The galaxy-galaxy lensing signal $\gamma_t^{ij}(\theta)$ captures the shear γ of background (source) galaxies caused by the mass distribution traced by foreground (lens) galaxy positions. We measure $\gamma_t^{ij}(\theta)$ by averaging the tangential shear of source galaxies in bin j around lens galaxies in bin i as a function of the angular separation between lens-source pairs. The $\gamma_t^{ij}(\theta)$ estimator, its measurement, and validation process are described in detail in [Y6GGL].
3. The cosmic shear functions $\xi_{\pm}^{ij}(\theta)$ capture the coherent distortion of galaxy shapes. We measure $\xi_{\pm}^{ij}(\theta)$ as the correlation of the shear of source galaxy pairs from source bins i and j as a function of their angular separation θ . The $\xi_{\pm}^{ij}(\theta)$ estimators are defined as the sum and difference of the products of the tangential and cross-components of the projected shear. More details on the estimator, the cosmic shear measurement, and validation process can be found in [Y6-1X2PT].

To compute these data vectors, we use the fast tree code TREECORR v5.1.1 [84]. We measure these correlation functions in 26 logarithmically-spaced angular bins spanning $2.5' < \theta \lesssim 1000'$. Only the 20 bins between $2.5' < \theta < 250'$ are used for the main analysis, as larger separations carry minimal additional information for the cosmological models we test here. We have 6 lens bins and 4 source bins, leading to a total of 1000 data points, excluding galaxy clustering cross-correlations. After scale cuts (see Section IV C) and the exclusion of lens bin 2 (see Section IV H), the final $3 \times 2\text{pt}$ data vector consists of 602 (652) data points for the linear (nonlinear) galaxy bias model. We plot all of the data in Figures 3 through 5.

The total signal-to-noise of the $3 \times 2\text{pt}$ data vector is $S/N = 110$ (95) after fiducial linear galaxy bias scale cuts without (with) point-mass marginalization (see Section IV A), where $S/N = \xi_{\text{data}} \mathbf{Cov}^{-1} \xi_{\text{model}} / \sqrt{\xi_{\text{model}} \mathbf{Cov}^{-1} \xi_{\text{model}}}$, with covariance matrix \mathbf{Cov} and best-fit model ξ_{model} . This is a 26% improvement over the DES Y3 $3 \times 2\text{pt}$ S/N. We obtain $S/N = 160$ (147) for the nonlinear galaxy bias case.

IV. ANALYSIS

We use the COSMOSIS [85] package to perform the inference of parameters \mathbf{p} from the observed $3 \times 2\text{pt}$ data \mathbf{D} . Throughout we assume a Gaussian likelihood of the form,

$$\mathcal{L}(\mathbf{D}|\mathbf{p}) \propto \exp \left(-\frac{1}{2} [\mathbf{D} - \mathbf{M}(\mathbf{p})]^T \mathbf{Cov}^{-1} [\mathbf{D} - \mathbf{M}(\mathbf{p})] \right), \quad (4)$$

where $\mathbf{M}(\mathbf{p})$ is the model for the observables, and \mathbf{Cov} is a predicted covariance matrix for the data. We now describe the model, its parameters, their priors, and the covariance matrix, and then the tools of the inference process.

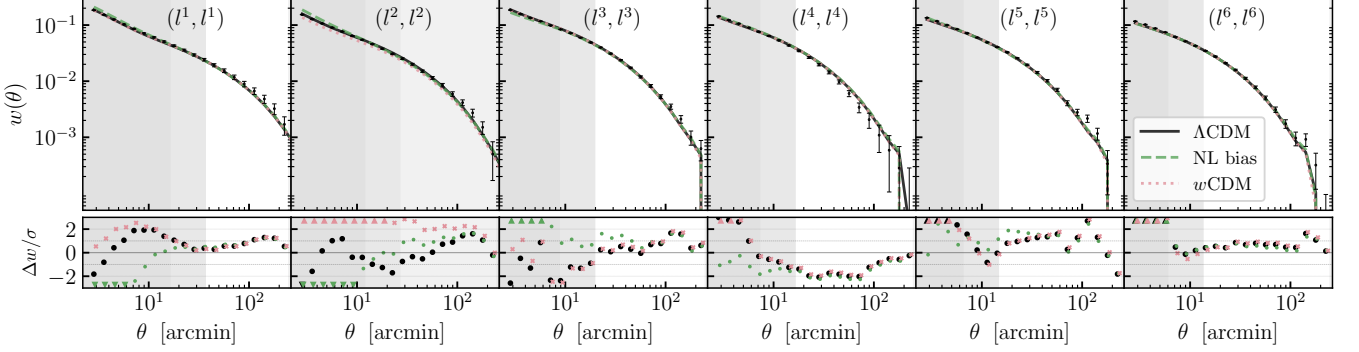


FIG. 3. Angular galaxy clustering auto-correlation function as a function of angular separation θ for different lens redshift bins. Upper panels show measurements (black points) with best-fit models: Λ CDM linear galaxy bias (black solid), Λ CDM nonlinear bias (green dashed), and w CDM linear bias (pink dotted). Lower panels show residuals in units of the expected standard deviation. Gray shaded regions indicate excluded scales: lighter gray for linear bias cuts, darker gray for nonlinear bias cuts. Lens bin 2 is entirely shaded because it is excluded from the fiducial analysis (see Appendix A). Triangle markers indicate the residuals are larger than 3σ .

A. Model

The 3×2 pt data vector used in this work concatenates the real-space galaxy clustering $w(\theta)$, galaxy-galaxy lensing $\gamma_t(\theta)$ and cosmic shear $\xi_{\pm}(\theta)$. All of these statistics are Fourier transforms of their respective angular (cross-) power spectra $C_{AB}(\ell)$ which under the full-sky prescription take the form:

$$w^{ij}(\theta) = \sum_{\ell} \frac{2\ell+1}{4\pi} P_{\ell}(\cos \theta) C_{\delta_{g,o} \delta_{g,o}}^{ij}(\ell), \quad (5)$$

$$\gamma_t^{ij}(\theta) = (1+m^j) \sum_{\ell} \frac{2\ell+1}{4\pi} \frac{P_{\ell}^2(\cos \theta)}{\ell(\ell+1)} C_{\delta_{g,o} E}^{ij}(\ell), \quad (6)$$

$$\xi_{\pm}^{ij}(\theta) = (1+m^i)(1+m^j) \times \quad (7)$$

$$\sum_{\ell} \frac{2\ell+1}{4\pi} \frac{2(G_{\ell,2}^+(x) \pm G_{\ell,2}^-(x))}{\ell^2(\ell+1)^2} [C_{EE}^{ij}(\ell) \pm C_{BB}^{ij}(\ell)].$$

Here, P_{ℓ} and P_{ℓ}^2 are the Legendre and associated Legendre polynomials of degree ℓ , $G_{\ell,2}^{\pm}$ are given by Equation (4.19) in [86], i and j indicate the tomographic redshift bins, $\delta_{g,o}$ refers to the observed galaxy density contrast, E/B refer to the weak lensing E/B -mode signals, and the set of m^i corresponds to the multiplicative shear bias parameters [Y6IMSIM], which account for biases in the shear calibration. The model is integrated over each specific angular bin range to ensure proper comparison with measurements.

The observed angular power spectra between the observed

galaxy density contrast and the shear field are

$$\begin{aligned} C_{\delta_{g,o} \delta_{g,o}}^{ii}(\ell) &= C_{\delta_g \delta_g}^{ii}(\ell) + C_{\delta_{\mu} \delta_{\mu}}^{ii}(\ell) + C_{\delta_{RSD} \delta_{RSD}}^{ii}(\ell) \\ &\quad + 2C_{\delta_g \delta_{\mu}}^{ii}(\ell) + 2C_{\delta_g \delta_{RSD}}^{ii}(\ell) + 2C_{\delta_{RSD} \delta_{\mu}}^{ii}(\ell), \\ C_{\delta_{g,o} E}^{ij}(\ell) &= C_{\delta_g \kappa}^{ij} + C_{\delta_g I_E}^{ij} + C_{\delta_{\mu} \kappa}^{ij} + C_{\delta_{\mu} I_E}^{ij}, \\ C_{EE}^{ij}(\ell) &= C_{\kappa \kappa}^{ij}(\ell) + C_{\kappa I_E}^{ij}(\ell) + C_{\kappa I_E}^{ji}(\ell) + C_{I_E I_E}^{ij}(\ell), \\ C_{BB}^{ij}(\ell) &= C_{I_B I_B}^{ij}(\ell), \end{aligned} \quad (8)$$

where the observed galaxy density receives contributions from lens magnification (δ_{μ}), affecting the observed number of galaxies and modeled as described in [Y6MAG], and from redshift-space distortions (δ_{RSD}) arising from the peculiar velocities of galaxies. The shear field receives contributions from the convergence field κ , including shear calibration effects, as well as from the intrinsic-alignment (IA) E/B modes ($I_{E/B}$), discussed in detail in [Y6-1X2PT], which mimic the cosmic shear signal and are produced due to the alignment of galaxies with their local environment.

For $C_{\delta_g \kappa}^{ij}(\ell)$ and $C_{\kappa \kappa}^{ij}(\ell)$, we compute the angular power spectra with the Limber approximation, which for a flat Universe takes the form:

$$C_{AB}^{ij}(\ell) = \int d\chi \frac{q_A^i(\chi) q_B^j(\chi)}{\chi^2} P_m \left(k = \frac{\ell+1/2}{\chi}, z(\chi) \right), \quad (9)$$

where \mathcal{A} and \mathcal{B} represent the fields being correlated, which in our case correspond to the galaxy overdensity field δ_g and the convergence field κ . The function $P_m(k, z)$ represents the three-dimensional matter power spectrum, which we evaluate at a given redshift z and wavenumber k . The linear matter power spectrum is computed with CAMB [87, 88], while the nonlinear power spectrum is based on HMCode2020 [89]. Due to the narrow width of the lens tomography bins, the Limber approximation is not sufficient for evaluating the angular galaxy clustering signal. Instead we carry out the non-Limber integrals using the linear/non-linear growth split described in [90]. The kernel or radial weight function for the galaxy over-

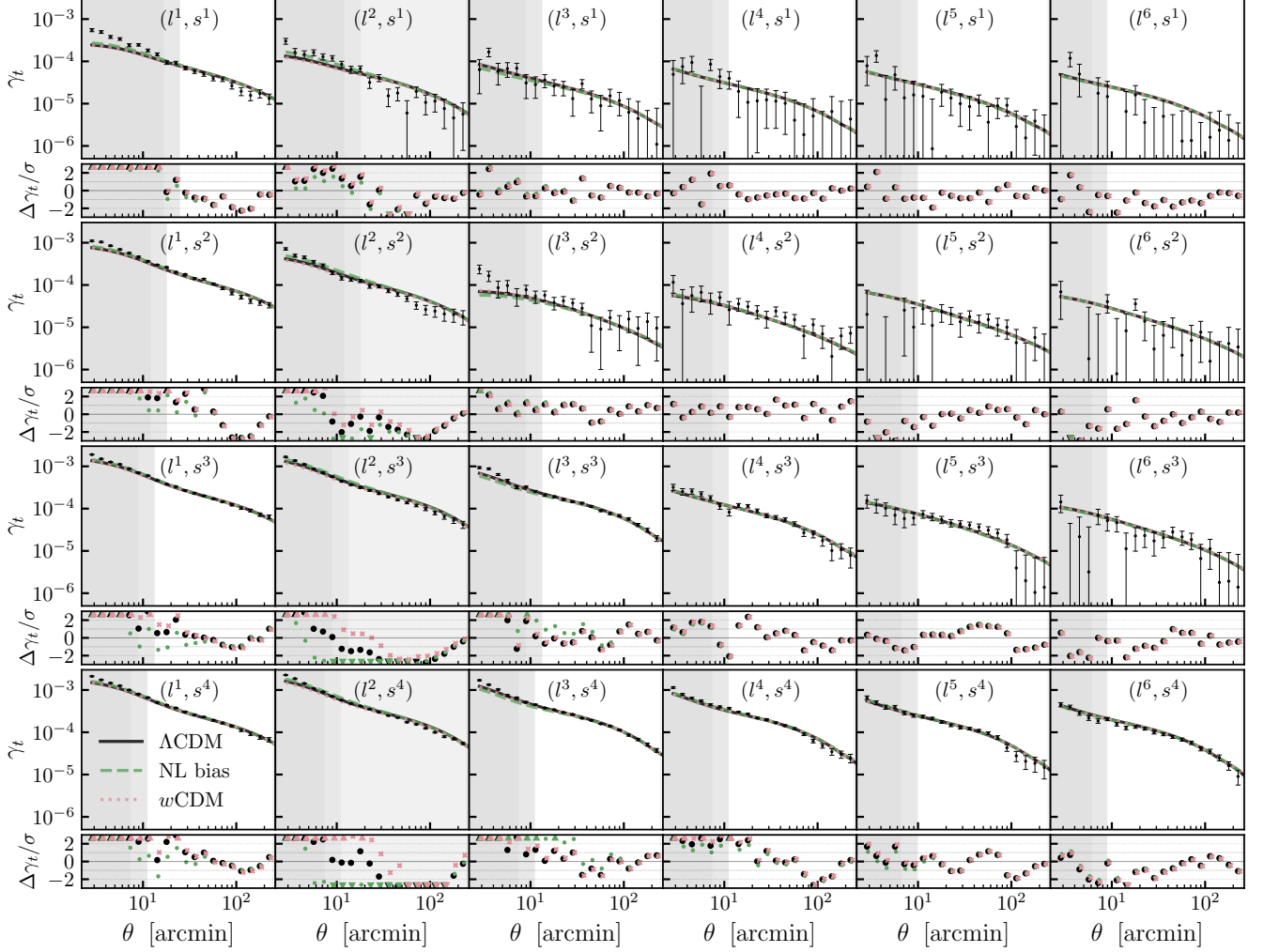


FIG. 4. Galaxy-galaxy lensing correlation function γ_t as a function of angular separation θ for different lens-source bin combinations (l^i, s^j) . Upper panels show measurements (black points) with best-fit models: Λ CDM linear galaxy bias (black solid), Λ CDM nonlinear bias (green dashed), and w CDM linear bias (pink dotted). Lower panels show residuals. Gray shaded regions indicate excluded scales: lighter gray for linear bias cuts, darker gray for nonlinear bias cuts. Lens bin 2 is entirely shaded because it is excluded from the fiducial analysis (see Appendix A). Note that this figure does not reflect the point-mass marginalization procedure, which is applied directly to the inverse covariance matrix during likelihood evaluation and cannot be visualized through the covariance matrix elements shown here.

density field is

$$q_{\delta_g}^i(\chi) = b_1^i n_1^i(z(\chi)) \frac{dz}{d\chi}, \quad (10)$$

and for the convergence field, the lensing efficiency is

$$q_{\kappa}^i(\chi) = \frac{3 H_0^2 \Omega_m \chi}{2 a(\chi)} \int_{\chi}^{\chi_H} d\chi' \frac{dz}{d\chi'} \frac{\chi' - \chi}{\chi'} n_s^i(z(\chi')), \quad (11)$$

where b_1^i are the linear galaxy bias coefficients, $n_{1/s}$ are the normalized redshift distribution of the lens/source galaxies, H_0 is the Hubble constant, and $a(\chi)$ is the scale factor for a given comoving distance χ . The lensing efficiency for the source sample is shown in the middle panel of Figure 2.

The matter power spectrum $P_m(k, z)$ and the distances $\chi(z)$ that appear in these equations are functions of the cosmological model. Our nominal Λ CDM model has the 6 free

parameters $A_s, \Omega_m, h, \Omega_b, n_s$ and $\sum m_{\nu}$. For a given set of parameters, we usually translate A_s to alternative measures of clustering more relevant at low-redshift, replacing it with either σ_8 (the RMS of linear fluctuations at scales of 8 Mpc/h) or $S_8 = \sigma_8(\Omega_m/0.3)^{0.5}$. We also explore the w CDM model, with an additional free parameter, the dark energy equation of state w .

The models contain several classes of nuisance parameters. Section II B introduced the multiplicative shear bias parameters m^i , with $i \in [1, 2, 3, 4]$ indexing source bins, with priors constrained by the shear image simulations. Section II E described the priors for the $n(z)$ perturbative mode amplitudes u_s^{β} , with $\beta \in [1, \dots, 7]$, and the 18 total lens-redshift mode

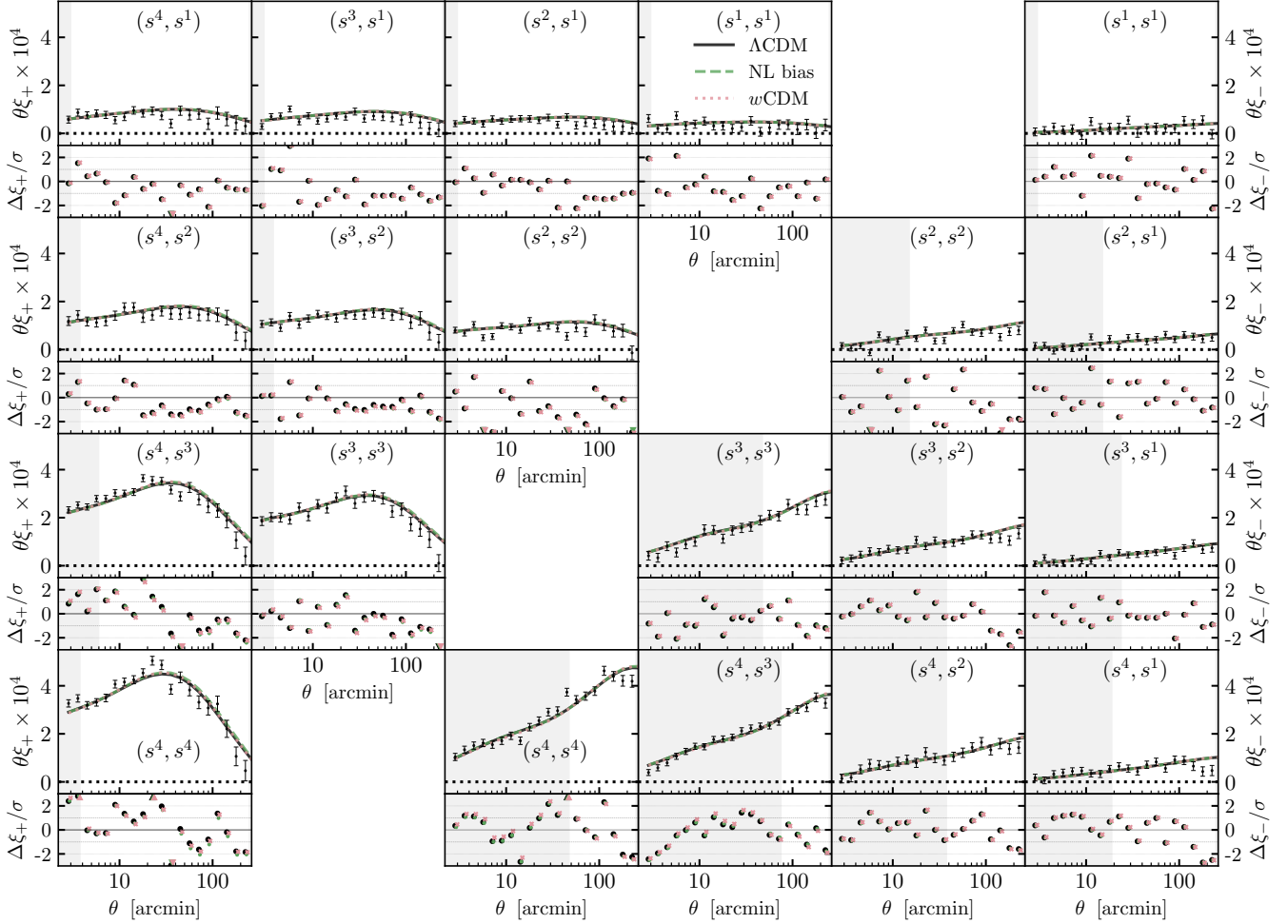


FIG. 5. Cosmic shear correlation functions $\xi_+(\theta)$ (left panels) and $\xi_-(\theta)$ (right panels) for different source redshift bin combinations (i, j) . Upper panels show measurements (black points) with best-fit models: Λ CDM linear galaxy bias (black solid), Λ CDM nonlinear bias (green dashed), and w CDM linear bias (pink dotted). Lower panels show residuals in units of the expected standard deviation. Gray shaded regions indicate excluded scales.

amplitudes $u_1^{i,\beta}$ ($\beta \in [1, 2, 3]$).⁴ We also use magnification coefficients α^i for each lens bin to model δ_μ , with calibration of their priors from image simulations detailed in [Y6MAG].

The remaining nuisance parameters in our model are required to account for uncertainties in astrophysical theory and observing conditions, as described below.

Nonlinear power spectrum: We model the impact of nonlinear structure formation on the matter power spectrum using HMCode2020 [89]. A significant uncertainty here is how much baryonic feedback, mainly from AGN, suppresses matter clustering. HMCode2020 introduces the effect of baryons via the sub-grid heating parameter $\Theta_{\text{AGN}} = \log_{10}(T_{\text{AGN}}/\text{K})$, indicating the strength of the AGN. We employ angular scale

cuts, to be described below, to mitigate potential biases from this uncertainty while fixing $\Theta_{\text{AGN}} = 7.7$ in our fiducial analysis (see [Y6MODEL] for more details). This value corresponds to the one employed in the fiducial BAHAMAS hydrodynamical simulations [91]. We examine the cosmological impact of other choices of parameters in Appendix C. We find them to cause $< 0.3\sigma$ changes in the inferred cosmology.

Nonlinear galaxy bias: Our simplest model assumes linear scale-independent galaxy bias, leading to a single free bias parameter b_1^i for each lens bin. We also explore a more complex nonlinear bias model with an additional free parameter b_2^i for local quadratic bias in each lens bin. For more details see [Y6MODEL].

Point-mass marginalization: Because the tangential shear signal $\gamma_t(\theta)$ is an integral of the mass distribution at radii $\leq \theta$, modeling uncertainty in the small-scale mass distribution around galaxies can propagate to larger radii. We account for this by marginalizing over a mean central point mass (PM) in

⁴ The full covariance among the m^i and u_s^β parameters derived in [Y6IMSIM] that accounts for source blending will be available with our ancillary data products.

each lens [92], which introduces a term with $1/\theta^2$ scaling,

$$\gamma_t^{ij}(\theta) \rightarrow \gamma_{t,\text{model}}^{ij}(\theta) + \frac{A^i}{\theta^2}. \quad (12)$$

We marginalize analytically over one PM amplitude per lens bin by adding a term to the inverse covariance, removing sensitivity to the mass distribution within our smallest retained θ value.

Intrinsic alignments (IA): The fiducial model for IA of the source galaxies is the tidal alignment and tidal torquing model [TATT, 93] described in [Y6MODEL]. Free parameters are required for IA scaling linearly with the tidal field (A_1), for IA quadratic in the tidal field (A_2), and for the dependence of each on source redshift (η_1, η_2). A fifth parameter, the coefficient b_{TA} for the IA term that scales as the product of the density field and its tidal field, is held fixed. The pivot redshift z_0 is chosen to match the peak sensitivity of DES Y6 shear data. In Appendix C, we investigate the consequences of freeing b_{TA} , and of fixing $A_2 = 0$ to reduce to the simpler nonlinear alignment [NLA, 94, 95] model.

Observing conditions marginalization: We analytically marginalize over uncertainty in computing the weights that remove correlations of the density field with observing conditions. See [Y6POS] for a description of the weights methods and marginalization and [Y6MASK] for details on the survey properties used as weights templates.

B. Covariance

The covariance of the $3 \times 2\text{pt}$ signal is computed analytically using COSMOcov [96, 97], which incorporates both Gaussian and non-Gaussian contributions. The covariance estimation code was thoroughly validated for the DES Y3 $3 \times 2\text{pt}$ analysis [98]. Furthermore, we marginalize analytically over uncertainties in the weights of observational systematics that modulate $w(\theta)$, as well as point mass contributions to the galaxy-galaxy lensing signal.

There are several changes in the Y6 covariance and modeling choices [Y6MODEL] compared to Y3, which have a well-understood impact on the error estimates: (i) we incorporate non-zero central values for multiplicative shear bias, requiring adjusted effective source galaxy densities; (ii) we employ HMCode2020 for signal modeling but keep HALOFIT [99] for covariance calculation; this leads to minor discrepancies in individual covariance elements ($\lesssim 2.5\%$) and negligible impact in our error estimates (see Appendix A 3); (iii) we compute survey geometry corrections to shape/shot noise [100] directly in configuration space from the Y6 random catalogs. The latter is necessitated by the fact that the Y6 mask contained more small-scale structures compared to Y3.

C. Scale cuts

Reference [Y6MODEL] derives lower bounds on θ for the DES Y6 $\xi_{\pm}(\theta)$, $\gamma_t(\theta)$, and $w(\theta)$ that reduce the influence of uncertainties in the theoretical model to well below the other

uncertainties in the inference. These scale cuts were tested for both ΛCDM and $w\text{CDM}$. For linear galaxy bias, the scale cuts are 9 Mpc/ h for $w(\theta)$, 6 Mpc/ h for $\gamma_t(\theta)$, and $[\Delta\chi^2]_{\text{max}} = 5$ for $\xi_{\pm}(\theta)$. For $w(\theta)$ and $\gamma_t(\theta)$, we convert the projected physical scales to an angular scale assuming the fiducial cosmology in [Y6MODEL] and the mean redshift of the lens bins. For $\Delta\chi^2$, we calculate the χ^2 difference between the theoretical cosmic shear data vector computed with our fiducial model and two versions generated using an alternate model for nonlinear dark matter clustering: one without baryonic feedback effects and another one with more extreme baryonic feedback contamination than our fiducial. We adjust the scale cut until $\Delta\chi^2 < [\Delta\chi^2]_{\text{max}}$. As such, $[\Delta\chi^2]_{\text{max}} = 5$ maps into concrete θ_{min} values per bin-pair (with smallest $\theta_{\text{min}} \sim 3'$ in our case). These cuts are similar to those used in DES Y3 [101], with $\xi_{\pm}(\theta)$ including slightly more scales. The nonlinear bias model enables use of smaller-scale data—down to 4 Mpc/ h for both $w(\theta)$ and $\gamma_t(\theta)$ as seen in Figures 3 and 4. This changes comes at the cost of having to marginalize over additional nuisance parameters for bias, resulting in nearly equal final precision [102, 103].

D. Sampling

Table III lists all the parameters used in the model $\mathbf{M}(\mathbf{p})$ for the likelihood in Equation 4 of our $3 \times 2\text{pt}$ data. The cosmological parameters of interest (A_s, Ω_m) and galaxy bias parameters take wide, flat priors, while tight, informative Gaussian priors are placed on nuisance parameters that we are able to constrain in simulations of our data (lens magnification, redshift and shear calibration parameters). Priors on the IA parameters are motivated by our current understanding of IA from observations (see [Y6MODEL]).

We sample \mathcal{L} in Equation 4 using the NAUTILUS sampler [104].⁵ The sampling results in Monte Carlo chains for $3 \times 2\text{pt}$ as well as other individual probes. For $3 \times 2\text{pt}$ chains, we also specifically test in Appendix B for potential prior-volume effects, whereby the posterior density is strongly influenced by nonlinear projection of the prior volume into the space of cosmological parameters (also known as “projection effects”). For our fiducial results, we only quote parameters that are not shifted significantly by prior-volume effects.

For some purposes, e.g., combining the likelihoods or posteriors of different probes across a common parameter space, it is necessary to produce a density estimator of the sampler output. We do this using normalizing flows [105–107]. Normalizing flows are machine-learning models that transform a simple base distribution (typically a multivariate Gaussian) into a complex target via a sequence of invertible, differentiable mappings. Once the mapping and its Jacobian are learned, one can both evaluate the probability density of the target distribution and draw samples from it. This enables

⁵ All runs with NAUTILUS use the following settings: $n_{\text{live}} = 10,000$, $\text{discard_exploration} = \text{T}$, $n_{\text{networks}} = 16$.

TABLE III. Fiducial values and priors for the cosmological, astrophysical, and calibration parameters. Parameters are sampled using either flat priors, denoted by [min, max], or Gaussian priors, following the notation $\mathcal{N}(\mu, \sigma^2)$ for a normal distribution with mean μ and variance σ^2 . The priors on the calibration parameters of the source galaxy samples—namely the multiplicative shear bias m and the source redshift distribution modes—are correlated, see Sec. IV A. The width of their Gaussian priors is determined by the covariance matrix of the parameters.

Parameter	Prior
Cosmology	
Ω_m	$[0.1, 0.6]$
$A_s \times 10^9$	$[0.5, 5]$
h	$[0.58, 0.8]$
Ω_b	$[0.03, 0.07]$
n_s	$[0.93, 1.00]$
w	$[-2, -1/3]$
m_ν [eV]	$[0.06, 0.6]$
Intrinsic alignment	
A_1	$[-1, 3]$
A_2	$[-3, 3]$
η_1	$\mathcal{N}(0.0, 3.0) \in [-5, 5]$
η_2	$\mathcal{N}(0.0, 3.0) \in [-5, 5]$
b_{TA}	1, fixed
z_0	0.3, fixed
Lens galaxy bias	
$b_1^i (i \in [1, 6])$	$[0.8, 3]$
$b_2^i (i \in [1, 6])$	$[-3, 3]$
Lens magnification	
α^1	$\mathcal{N}(1.58, 0.04)$
α^2	$\mathcal{N}(1.38, 0.11)$
α^3	$\mathcal{N}(2.04, 0.08)$
α^4	$\mathcal{N}(2.21, 0.08)$
α^5	$\mathcal{N}(2.45, 0.14)$
α^6	$\mathcal{N}(2.42, 0.13)$
Lens n(z) modes	
$u_1^{i,\beta} (i \in [1, \dots, 6], \beta \in [1, 2, 3])$	$\mathcal{N}(0, 1) \in [-3, 3]$
Source n(z) modes	
$u_s^\beta (\beta \in [1, \dots, 7])$	$\mathcal{N}(0, 1) \in [-3, 3]$
Shear calibration	
m^1	$\mathcal{N}(-0.0034, 0.0058)$
m^2	$\mathcal{N}(0.0065, 0.0066)$
m^3	$\mathcal{N}(0.0159, 0.0059)$
m^4	$\mathcal{N}(0.0017, 0.0122)$
External CMB data	
A_{CMB} (ACT & <i>Planck</i>)	$\mathcal{N}(1.0, 0.0025) \in [0.9, 1.1]$
T_{cal} (SPT-3G)	$\mathcal{N}(1.0, 0.0036) \in [0.8, 1.2]$
P_{ACT} (ACT)	$[0.9, 1.1]$
E_{cal} (SPT-3G)	$[0.8, 1.2]$

combining independent probes without rerunning chains for the full joint likelihood. The normalizing flow is implemented in the `tensiometer` package [106, 108].

E. Goodness of fit and internal consistency

We assess the ability of our model to fit the data using two approaches: a posterior predictive distribution (PPD) metric that quantifies the internal consistency of measurements; and point estimates of the goodness of fit for the maximum *a posteriori* (MAP) parameters.

The PPD is the probability distribution for realizations of a set of test observables \mathbf{D}_t conditioned on a measurement of a (potentially different) set of observables, $\mathbf{D}_c^{\text{obs}}$. Given model parameters \mathbf{p} and an estimate of the posterior $P(\mathbf{p}|\mathbf{D}_c^{\text{obs}})$,

$$P(\mathbf{D}_t|\mathbf{D}_c^{\text{obs}}) = \int P(\mathbf{D}_t|\mathbf{D}_c^{\text{obs}}, \mathbf{p}) P(\mathbf{p}|\mathbf{D}_c^{\text{obs}}) d\mathbf{p}. \quad (13)$$

Comparing an actual measurement $\mathbf{D}_t^{\text{obs}}$ to the PPD assesses the consistency of measurements \mathbf{D}_t and \mathbf{D}_c under the assumed model. We can compress a high-dimensional PPD distribution to a single summary statistic giving the fraction of \mathbf{D}_t with lower PPD than the observed $\mathbf{D}_t^{\text{obs}}$:

$$\Delta_{\text{PPD}} = \int_{P(\mathbf{D}_t|\mathbf{D}_c^{\text{obs}}) < P(\mathbf{D}_t^{\text{obs}}|\mathbf{D}_c^{\text{obs}})} P(\mathbf{D}_t|\mathbf{D}_c^{\text{obs}}) d\mathbf{D}_t. \quad (14)$$

Small values of Δ_{PPD} indicate a lack of consistency, while values close to one signify over-fitting. If $\mathbf{D}_t = \mathbf{D}_c$, or if the test observables are a subset of \mathbf{D}_c , this serves as an assessment of the goodness of fit. We can also evaluate the PPD for cases where \mathbf{D}_t and \mathbf{D}_c are disjoint but correlated sets of observables in order to assess the internal consistency between those measurements.

For Y6, PPDs are estimated using Gaussian mixture models. The Y6 PPD methods and their improvements over Y3 methods [109] are detailed in [Y6PPD].

Another statistic used to gauge goodness of fit is the value of χ^2 at the best-fit parameter values. The standard way to compute this would be $\chi^2 = -2 \ln \mathcal{L}_{\text{max}}$, evaluated at the parameter values maximizing the likelihood given in Equation 4. In this work, we employ a slightly different definition that incorporates agreement with Gaussian priors as part of our goodness-of-fit assessment, following [110]. If the posterior for data \mathbf{D} at a location \mathbf{p} in parameter space is $P(\mathbf{p}|\mathbf{D}) \propto \mathcal{L}(\mathbf{D}|\mathbf{p})\pi_G(\mathbf{p})\pi_F(\mathbf{p})$, where π_G is the product of all Gaussian priors and $\pi_F \equiv \prod_i (\Delta\theta_i)^{-1}$ is the product of all flat priors (where $\Delta\theta$ is the prior width for each parameter i), then we define $\chi^2 = -2 \ln [\mathcal{L}\pi_G]_{\text{max}}$. Since the same parameters that maximize the posterior will also maximize the product $\mathcal{L}\pi_G$, we can simply evaluate this from the MAP by subtracting the contribution from π_F .

If P_{MAP} is the value of the posterior associated with the MAP parameters, we thus compute

$$\chi^2 = -2 \ln P_{\text{MAP}} - 2 \sum_i \ln \Delta\theta_i. \quad (15)$$

While in this paper we only report χ^2 statistics in the context of model comparison, we did evaluate χ^2 per degree of freedom as a cross-check on PPD statistics during pre-unblinding validation checks (see Table VIII from Appendix A). For that evaluation, the number of degrees of freedom $\nu = N_{\text{data}} - N_{\text{eff}}$ is evaluated by adjusting the number of sampled parameters to

$$N_{\text{eff}} = N_{\text{sampled}} - \text{Tr}(\mathcal{C}_P \mathcal{C}_\pi^{-1}), \quad (16)$$

where \mathcal{C}_P and \mathcal{C}_π^{-1} are parameter covariances estimated from the posterior and prior, respectively.

We estimate MAP parameters using a two-step optimization procedure, where the $N_{\text{guess}} = 20$ highest posterior samples from a chain are used as starting guesses for optimizer searches.⁶ We select \mathbf{p}_{MAP} to be the parameters associated with the highest posterior found among those N_{guess} searches. To indicate when marginal 1D posteriors may be dominated by volume effects, we also compute and show the projected joint highest posterior density (PJ-HPD) of parameters. The PJ-HPD indicates the highest posterior density region that contains 68% of a parameter's marginal posterior mass [111]. By definition it includes the MAP and large differences between the marginal 1D posteriors and the PJ-HPD indicate where projection or volume effects may be significant.

F. Tension metrics and external consistency

We require a measure of the consistency of probability distributions over the same parameters \mathbf{p} conditioned on two different experiments, A and B —for example, we must do so before ascribing any meaning to their joint constraint $P(\mathbf{p}|A, B)$. We measure consistency from the probability of a parameter difference, following the method described in [106, 108], as employed in the recent DES analyses [107, 112]. The parameter difference probability density, $P(\Delta\mathbf{p})$, is given by the cross-correlation integral:

$$P(\Delta\mathbf{p}) = \int P(\mathbf{p}|A) P(\mathbf{p} - \Delta\mathbf{p}|B) d\mathbf{p}. \quad (17)$$

A scalar consistency estimator is the $\Delta\mathbf{p}$ probability above the iso-density contour corresponding to no parameter shift ($\Delta\mathbf{p} = 0$):

$$\Delta = \frac{1}{\sum_{i=1}^n w_i} \sum_{i=1}^n w_i S(\hat{P}(\Delta\mathbf{p}_i) - \hat{P}(0)), \quad (18)$$

where $S(x)$ is the Heaviside step function (unity for $x > 0$, zero otherwise), n is the number of samples $\Delta\mathbf{p}_i$ from $P(\Delta\mathbf{p})$ with weights w_i and \hat{P} represents their probability as given by the normalizing flow model for the parameter difference distribution.

⁶ We use `scipy`'s Powell optimizer in our analysis, though we find similar results for noise levels with `minuit` and `BOBYQA` algorithms. See Appendix E of [Y6MODEL] for more details.

Tension results are reported in terms of the effective number of standard deviations, i.e. the number of standard deviations that an event with the same probability would have had if it had been drawn from a Gaussian distribution [108]:

$$n_\sigma \equiv \sqrt{2} \text{erf}^{-1}(\Delta), \quad (19)$$

where erf^{-1} is the inverse error function. We set $n_\sigma < 3$ as the criterion for different data sets agreeing well enough that it makes sense to examine their combined constraint.

While the integrations in Equations 17 and 18 can be done if we are interested in consistency for a single dimension of parameter space, more generally it involves a high-dimensional integral further complicated by knowing $P(\mathbf{p}|A)$ and $P(\mathbf{p}|B)$ only through a set of incommensurate samples. In practice, the estimation of Δ is done by constructing density estimators with normalizing flows, and executing the integral in Equation 18 via Monte Carlo methods, as described in [106] and executed by the `tensiometer` code. In this paper, most of the discussion will center around full-parameter tensions as listed in Table VI, but we will also quote 1D or 2D numbers when needed.

G. Model comparison

We employ two metrics for deciding whether the data prefer ΛCDM or $w\text{CDM}$:

- **Posterior differences:** Taking advantage of the fact that ΛCDM is a nested model of $w\text{CDM}$, we require $|1 - w| \gg \sigma(w)$ to have significant preference for $w\text{CDM}$ over ΛCDM , where w and $\sigma(w)$ are the mean and standard deviation of the marginalized posterior of the $w\text{CDM}$ model.
- **Goodness-of-fit differences:** We compute goodness-of-fit differences as:

$$\Delta\chi^2 \equiv \chi^2_{w\text{CDM}} - \chi^2_{\Lambda\text{CDM}}, \quad (20)$$

where each χ^2 is computed with Equation 15. We note that the fact that the ΛCDM parameter space is a subset of $w\text{CDM}$ guarantees $\Delta\chi^2 \leq 0$. To assess the significance of the resulting value, we conduct a likelihood ratio test: we evaluate the probability p of finding a value higher than $|\Delta\chi^2|$ when drawing from a χ^2 distribution with one degree of freedom. We then convert this to the effective number of standard deviations for a χ^2 variable.

H. Blinding and unblinding

To avoid confirmation bias, it is necessary for decisions about the analysis to be made without knowledge of whether they will drive the inferred cosmological parameters closer to or further from particular values, such as previous experiments' results. This is particularly true when previous results have shown marginal evidence for failure of the ΛCDM

model. A blinding framework also forces a large collaboration to codify the criteria that will be used to detect internal inconsistencies in their data and resolve them before knowing the results. The DES Y6 3×2 pt analysis has three levels of blinding.

- **Catalog level:** The galaxy shapes e —and the inferred shears γ —in the METADETECTION catalog are rescaled by some blind factor $0.9 < f < 1.1$ (more precisely, $\eta = \tanh^{-1} e$ is rescaled). All work proceeds with the blinded shear catalog until a suite of null tests on the catalog, described in [Y6SHEAR], are successfully passed. For example, the inferred shear γ should have no correlation with the properties of the PSF.
- **Data-vector level:** The summary statistics derived from the catalogs are transformed using the technique from [113], whereby they are changed by factors that would transform data from a nominal cosmology to some (blind) other cosmology. This preserves the ability to check for consistency within and between the summary statistics under the cosmological models being considered. The null tests performed are described in [Y6-1X2PT] (for ξ_{\pm}), [Y6GGL] (for γ_t) and [Y6POS] (for w). All choices of measurement and astrophysical models are complete before the data vectors are unblinded. Once all tests pass in this stage, we unblind the data vector. Note that we do not run chains on the blinded data vectors in this framework.
- **Cosmology level:** Cosmological inference chains for 3×2 pt, 2×2 pt ($w + \gamma_t$) and 1×2 pt (ξ_{\pm}) are run without revealing the values of cosmological parameters they yield. The covariance matrix for these runs assumes a fiducial cosmology. The Δ_{PPD} values from these chains must exceed the predetermined threshold $\Delta_{\text{PPD}} > 0.01$, and internal consistency between the probes is also tested and required to have $\Delta_{\text{PPD}} > 0.01$. We also examine the χ^2/ν values of the MAP fits (without revealing the MAP values). We check whether the posterior distributions of any of the redshift, shear and magnification nuisance parameters push strongly against the priors. Once these tests are passed, we recalculate the covariance matrix using the (still blind) MAP cosmology from the 3×2 pt case, then rerun the chains and recheck the Δ_{PPD} values. Only after these pass do we unblind the cosmological parameters.

During the last stage of unblinding, several PPD tests failed, and the posterior for one of the $n(z)$ modes of lens bin 2 was pushing strongly against its prior. After a thorough investigation, we were unable to determine the exact cause of this behavior of lens bin 2. To be conservative, we decided to complete the analysis without using any data involving lens redshift bin 2. After this change, all blinding tests passed, and the results were unblinded.

We emphasize that the aforementioned investigation involved reviewing most of the pipeline and three iterations of blind inference. The decision-making process was outlined in

advance by a detailed analysis plan, which prevented any post hoc decisions. In itself, this serves as an important lesson for future Stage IV missions.

The complete unblinding criteria, and the investigation of lens bin 2, are described in Appendix A. We also show that in the post-unblinding results, neither the values nor the constraining power of the inferred cosmology are meaningfully altered by the omission of lens bin 2.

V. COSMOLOGY FROM DES Y6 3×2 PT

In this section, we present the cosmological constraints derived from the DES Y6 3×2 pt probes. We present our constraints for ΛCDM in Section V A and compare them to those from the CMB in Section V B. Constraints for $w\text{CDM}$ are presented in Section V C. For all constraints, we report the mean in each parameter, along with the 68% credible level (CL) of posterior volume around the mean and the MAP in parentheses. Also, as described in Appendix B, we omit quoting quantities that suffer from severe prior volume effects as tested in simulations. Table IV and Table V summarize all the numerical results from this paper, while Figure 8 provides a visual representation of S_8 , Ω_m and σ_8 constraints in the ΛCDM model.

A. ΛCDM

1. Linear galaxy bias

The main 3×2 pt constraints assuming ΛCDM and linear galaxy bias are shown in Figure 6, overlaid by the individual ξ_{\pm} and 2×2 pt constraints. We show in Appendix E the posterior in the full parameter space. From Figure 6 we observe that ξ_{\pm} and 2×2 pt individually have similar constraining power in the $\Omega_m - S_8$ two-dimensional plane, with ξ_{\pm} having better precision in S_8 and 2×2 pt in Ω_m . The calculated figures of merit $\text{FoM}_{\sigma_8, \Omega_m}$ in the σ_8, Ω_m plane (Table IV) are similar for ξ_{\pm} and 2×2 pt, and their combination into 3×2 pt increases the $\text{FoM}_{\sigma_8, \Omega_m}$ by more than a factor of two due to degeneracy breaking in the high-dimensional space.

ξ_{\pm} and 2×2 pt are consistent with each other, having $\Delta_{\text{PPD}} = 0.049$, even though the marginalized two-dimensional contours appear somewhat offset from each other. For two highly covariant data sets, there is no a priori expectation or requirement that the projection of their joint posterior in a small subset of the parameter space should be centered on the mean of the two individual contours.

For the main cosmological parameters from 3×2 pt, we find

$$\begin{aligned} S_8 &= 0.789_{-0.012}^{+0.012} \quad (0.793), \\ \Omega_m &= 0.333_{-0.028}^{+0.023} \quad (0.316), \\ \sigma_8 &= 0.751_{-0.036}^{+0.034} \quad (0.772), \end{aligned} \quad (21)$$

We are also able to independently constrain $\Omega_b \times 10^2 = 4.58_{-0.93}^{+0.75}$ using DES 3×2 pt. We show in Appendix C that

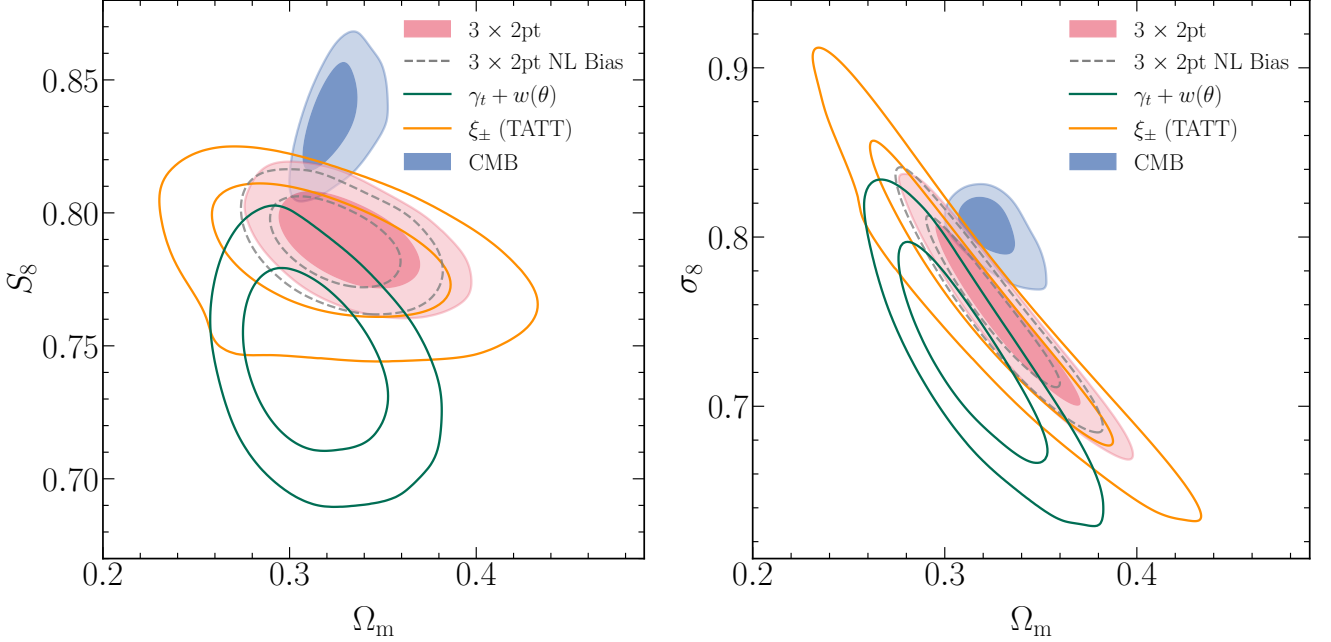


FIG. 6. Marginalized constraints in Ω_m , σ_8 , and $S_8 \equiv \sigma_8 \sqrt{\Omega_m/0.3}$ in the Λ CDM analysis of cosmic shear (ξ_+ , orange), galaxy clustering plus galaxy-galaxy lensing ($w(\theta) + \gamma_t$, green), and their combination ($3 \times 2\text{pt}$, pink). Additionally, we show the result from the nonlinear galaxy bias ($3 \times 2\text{pt NL Bias}$, dashed grey line) and the CMB (solid blue). Depicted contours represent the 68% and 95% credible levels.

these results are robust to many variations of the analysis choices. In Appendix D, we break down the relative contributions to the uncertainties from different sources by fixing the nuisance parameters and looking at the resulting change in the cosmological constraints.

The DES Y6 $3 \times 2\text{pt}$ constraints are compared to previous DES $3 \times 2\text{pt}$ results in Figure 7. The Y1 constraint is from [36] and the Y3 constraint from [37]. We do not attempt to homogenize the analysis choices here between the three results, as there has been significant evolution of both the data samples and the modeling approach since Y1. Overall, we see a sustained gain in constraining power from Y1 to Y3 to Y6. Table IV shows $\text{FoM}_{\sigma_8, \Omega_m}$ gains as $1085 \rightarrow 2068 \rightarrow 3907$. The three sets of contours are consistent, with Y1 having slightly lower Ω_m central value.

2. Nonlinear galaxy bias

We also analyze our $3 \times 2\text{pt}$ data vector assuming a nonlinear galaxy bias model, going to smaller scales with the $2 \times 2\text{pt}$ data vector while allowing for one additional free parameter per lens bin as well as two additional bias parameters fixed by a relationship to the linear bias [Y6MODEL]. The constraints are shown as dashed lines in Figure 6. We find

$$\begin{aligned} S_8 &= 0.789_{-0.011}^{+0.011} \quad (0.788), \\ \Omega_m &= 0.325_{-0.025}^{+0.021} \quad (0.330), \\ \sigma_8 &= 0.759_{-0.034}^{+0.032} \quad (0.752). \end{aligned} \quad (22)$$

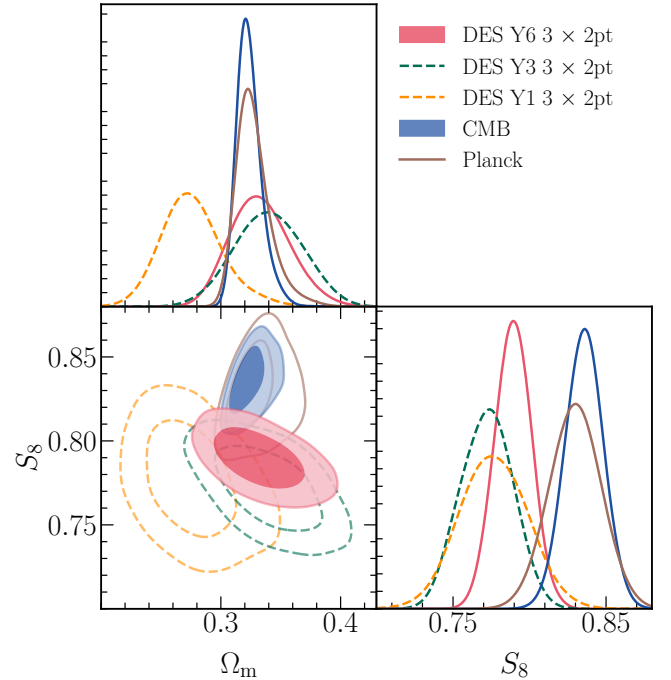


FIG. 7. S_8 and Ω_m constraints in Λ CDM from DES Y6 $3 \times 2\text{pt}$ compared to the combined primary CMB constraints. We also include the results from the DES Y3 $3 \times 2\text{pt}$ analysis, in which we compared with the primary *Planck* 2018 constraints, also overlaid in the figure. When comparing with *Planck* only, the difference in the $S_8 - \Omega_m$ plane is reduced from 1.9σ (Y3) to 1.4σ (Y6). This difference increases to 2.2σ in Y6 when comparing to the combined CMB likelihood. We also overlay the published DES Y1 $3 \times 2\text{pt}$ constraints.

These constraints are consistent with the linear bias analysis, and only slightly tighter than those assuming linear galaxy bias, with a less than 10% improvement on S_8 and an increase of about 14% in $\text{FoM}_{\sigma_8, \Omega_m}$ (see Table IV). These gains are very similar to the ones found in DES Y3 [37]. These results indicate that our fiducial ΛCDM $3\times 2\text{pt}$ constraints are robust to galaxy bias modeling. Due to the similarity in constraints, and because the gain in using nonlinear galaxy modeling is not sufficient to justify the added computational complexity when exploring analysis variants, in the remainder of the paper we primarily present results using linear galaxy bias (unless otherwise specified). We also find slightly larger prior-volume effects for the nonlinear bias model ($\sim 0.5\sigma$ for the main parameters of interest, compared to $\sim 0.2\sigma$ for linear bias), as detailed in Appendix B.

B. Comparison with the CMB in ΛCDM

Next, we compare our results with the primary CMB constraints. As we will describe in more detail in Section VII, the particular combination of CMB likelihoods used here is the combined likelihood of *Planck* 2018 [1], ACT-DR6 [3], and SPT-3G DR1 [4], for primary temperature and polarization data, but without CMB lensing. Figure 6 gives a visual impression of the two sets of constraints. DES Y6 $3\times 2\text{pt}$ (pink) and CMB (blue) overlap at the 2σ contour in this parameter subspace. The S_8 constraining power of the CMB is comparable to that of DES $3\times 2\text{pt}$, while the CMB constrains Ω_m about a factor 2-3 more tightly than DES $3\times 2\text{pt}$. We calculate the statistical consistency between these two constraints in Table VI. We compare the two constraints in the one-dimensional (S_8) and two-dimensional ($S_8 - \Omega_m$) parameter spaces most constrained by $3\times 2\text{pt}$, and in the full N -dimensional parameter space based on Equation 19. We find the difference to be 2.6σ , 2.2σ and 1.8σ respectively⁷. $3\times 2\text{pt}$ is most sensitive to directions in parameter space like S_8 , so we are more likely to detect at higher significance any separations between the two posteriors in that projected parameter direction. Similar results were found in previous work [37].

If we consider only the full-parameter difference between $3\times 2\text{pt}$ and CMB, our result (1.8σ) is slightly higher than what was found in DES Y3 (1.5σ , Table III of [37]), but both are still consistent. As such, we are able to combine the DES Y6 $3\times 2\text{pt}$ results with the CMB data, yielding the constraints in Table IV. In detail, both the $3\times 2\text{pt}$ results from DES and the CMB result have improved since our DES Y3 analysis [37] and slightly shifted: from Y3 to Y6 DES $3\times 2\text{pt}$, the constraining power improved by a factor of 2 in the $S_8 - \Omega_m$ plane, while S_8 shifted higher; from *Planck* 2018 to the CMB combination used in this work (SPT+ACT+*Planck*), the constraining power also improved and S_8 also shifted higher. Fig-

ure 7 shows this change. The net result is a slight increase in separation between $3\times 2\text{pt}$ and CMB, even though the DES Y6 $3\times 2\text{pt}$ became *more* consistent with *Planck* 2018 than Y3, being now at 1.0σ while it was at 1.5σ in DES Y3.

C. $w\text{CDM}$

We test a model with one additional free parameter, the dark energy equation of state parameter w , assumed to be constant in time. In this $w\text{CDM}$ model, the dark energy density evolves with redshift as $\rho_{DE} \sim (1+z)^{3(1+w)}$. We find

$$\begin{aligned} w &= -1.12^{+0.26}_{-0.20} \quad (-1.12) \\ \Omega_m &= 0.325^{+0.032}_{-0.035} \quad (0.329) \\ S_8 &= 0.781^{+0.021}_{-0.020} \quad (0.778). \end{aligned} \quad (23)$$

Our constraints show no evidence for departure from a ΛCDM model, e.g. are consistent with $w = -1$. When using a nonlinear galaxy bias model, we find $w = -1.13^{+0.24}_{-0.19}$ (-0.89), $\Omega_m = 0.317^{+0.031}_{-0.032}$ (0.324) and $S_8 = 0.778^{+0.020}_{-0.018}$ (0.798), very similar to the linear bias results, and still within 1σ of ΛCDM . The ΛCDM constraint on S_8 of $0.789^{+0.012}_{-0.012}$ (0.793) is significantly weakened to $0.781^{+0.021}_{-0.020}$ (0.778) in $w\text{CDM}$.

We further assess whether the data prefer a $w\text{CDM}$ universe over a ΛCDM one using the criterion described in Section IV G. We obtain $\Delta\chi^2 = -0.82$ (0.9σ) as defined in Equation 20, corresponding to no significant preference for $w\text{CDM}$.

We compare the consistency of our results with those from the CMB in the $w\text{CDM}$ model in the right panel of Figure 9, which shows posteriors of $3\times 2\text{pt}$ and CMB in the $w - \Omega_m$ plane, which lay on top of each other. However the agreement in $S_8 - \Omega_m$ is similar as in ΛCDM . In the full parameter space, both datasets are consistent at the 1.3σ level. Projected in S_8 the parameter difference is 1.0σ , while in the $w - S_8$ plane, we observe a higher difference with respect to the CMB, reaching 2.1σ .

VI. COMBINATION WITH OTHER DES DATA

In this section we present cosmological constraints from combining the latest results from the four main cosmological probes in DES: the recently recalibrated Type Ia supernovae (DES SN), baryon acoustic oscillation (DES BAO), galaxy clusters (DES CL), and the $3\times 2\text{pt}$ results from this work (DES Y6 $3\times 2\text{pt}$). Since its conception, the Dark Energy Survey was designed to combine these four complementary cosmological probes through its coherent and self-calibrating low-redshift cosmology program. We describe below the likelihoods we use for these other three probes.

- **DES BAO:** DES measured the Baryonic Acoustic Oscillation (BAO) feature from the clustering of galaxies using the full survey data in [47], using a sample optimized for BAO in [114]. This sample consists of

⁷ We also examined $S_8^\alpha \equiv \sigma_8 (\Omega_m/0.3)^\alpha$ with optimized $\alpha = 0.617$, our best-constrained direction, which yields $S_8^{\alpha=0.617} = 0.799^{+0.011}_{-0.010}$ (MAP: 0.797). This remains in 2.5σ tension with CMB, similar to the 2.6σ found for standard S_8 .

TABLE IV. Summary of marginalized parameter constraints in Λ CDM. The mean and 68% CL are provided for each cosmological parameter, followed by the maximum *a posteriori* (MAP) value in parentheses, except for neutrino mass, for which the 95% upper bound is given. For data combinations where we use normalizing flows to combine posterior samples directly (and without access to the full likelihood), we do not report MAP values as they cannot be reliably determined. Parameters that are not significantly constrained are indicated by a dash. Except for DES Y1 and Y3, all data have been re-analyzed with model and prior choices matching the DES Y6 3 \times 2pt analysis. “DES all probes” stands for the data combination used in Section VI: DES Y6 3 \times 2pt, DES BAO, DES SN, DES CL. “CMB” stands for the CMB combination described in Section VII: *Planck* 2018, ACT DR6, SPT-3G DR1 (only primary probes, we do not include CMB lensing). “Ext. Low- z ” represents the combination of the most constraining low-redshift data described in Section VII: DESI DR2 BAO, DES BAO (excl DESI), DES SN, SPT CL. We also define “All Ext.”: CMB, Ext. Low- z .

Λ CDM	S_8	Ω_m	σ_8	$\Omega_b \times 10^2$	n_s	h	$\sum m_\nu$ (eV)	$\text{FoM}_{\sigma_8, \Omega_m}$
DES Data								
3 \times 2pt	$0.789^{+0.012}_{-0.012}$ (0.793)	$0.333^{+0.023}_{-0.028}$ (0.316)	$0.751^{+0.034}_{-0.036}$ (0.772)	$4.58^{+0.75}_{-0.93}$ (4.16)	—	—	—	3907
3 \times 2pt (NL Bias)	$0.789^{+0.011}_{-0.011}$ (0.788)	$0.325^{+0.021}_{-0.025}$ (0.330)	$0.759^{+0.032}_{-0.034}$ (0.752)	$4.66^{+0.79}_{-0.97}$ (4.65)	—	—	—	4455
$\gamma_t + w(\theta)$	$0.743^{+0.023}_{-0.023}$ (0.765)	$0.314^{+0.020}_{-0.029}$ (0.283)	$0.729^{+0.043}_{-0.043}$ (0.787)	—	—	—	—	1833
ξ_{\pm}	$0.783^{+0.019}_{-0.015}$ (0.763)	$0.321^{+0.036}_{-0.047}$ (0.377)	$0.763^{+0.053}_{-0.062}$ (0.681)	—	—	—	—	1450
DES Y3 3 \times 2pt	$0.776^{+0.017}_{-0.017}$ (0.776)	$0.339^{+0.032}_{-0.031}$ (0.372)	$0.733^{+0.039}_{-0.049}$ (0.696)	—	—	—	—	2068
DES Y1 3 \times 2pt	$0.747^{+0.027}_{-0.025}$ (0.770)	$0.303^{+0.034}_{-0.041}$ (0.253)	$0.747^{+0.052}_{-0.068}$ (0.838)	—	—	—	—	1085
DES all probes	$0.796^{+0.010}_{-0.011}$ —	$0.320^{+0.011}_{-0.013}$ —	$0.771^{+0.019}_{-0.020}$ —	$4.05^{+0.35}_{-0.90}$ —	—	—	—	8373
External Data								
Ext. Low- z	$0.801^{+0.019}_{-0.020}$ —	$0.304^{+0.007}_{-0.008}$ —	$0.796^{+0.019}_{-0.019}$ —	$4.84^{+0.96}_{-0.42}$ —	—	—	—	7426
CMB	$0.836^{+0.012}_{-0.013}$ (0.837)	$0.324^{+0.007}_{-0.012}$ (0.314)	$0.805^{+0.014}_{-0.007}$ (0.818)	$5.04^{+0.07}_{-0.12}$ (4.93)	$0.970^{+0.004}_{-0.004}$ (0.971)	$0.667^{+0.009}_{-0.006}$ (0.675)	< 0.24 (95% CL)	8994
Combined Data								
3 \times 2pt + Ext. Low- z	$0.799^{+0.009}_{-0.010}$ —	$0.307^{+0.006}_{-0.006}$ —	$0.789^{+0.012}_{-0.013}$ —	$4.99^{+0.77}_{-0.27}$ —	—	—	< 0.47 (95% CL)	17045
3 \times 2pt + CMB	$0.811^{+0.008}_{-0.008}$ (0.813)	$0.313^{+0.006}_{-0.009}$ (0.305)	$0.795^{+0.013}_{-0.008}$ (0.807)	$4.95^{+0.06}_{-0.10}$ (4.85)	$0.974^{+0.003}_{-0.003}$ (0.974)	$0.675^{+0.007}_{-0.004}$ (0.681)	< 0.22 (95% CL)	16598
DES all probes + CMB	$0.815^{+0.008}_{-0.007}$ —	$0.314^{+0.006}_{-0.007}$ —	$0.797^{+0.012}_{-0.007}$ —	$4.95^{+0.05}_{-0.08}$ —	$0.973^{+0.003}_{-0.003}$ —	$0.674^{+0.006}_{-0.004}$ —	< 0.21 (95% CL)	20590
3 \times 2pt + All Ext.	$0.806^{+0.006}_{-0.007}$ —	$0.302^{+0.003}_{-0.003}$ —	$0.804^{+0.007}_{-0.006}$ —	$4.83^{+0.03}_{-0.04}$ —	$0.976^{+0.003}_{-0.003}$ —	$0.683^{+0.003}_{-0.002}$ —	< 0.14 (95% CL)	51955

TABLE V. Summary of marginalized parameter constraints in w CDM. The combination used for “Ext. Low- z ”, “CMB” and “All Ext.” is the same as in Table IV, while “DES all probes” does not include DES CL (see text for details).

w CDM	S_8	Ω_m	σ_8	$\Omega_b \times 10^2$	n_s	h	w	$\sum m_\nu$ (eV)	$\text{FoM}_{\sigma_8, \Omega_m}$
									FoM_{w, Ω_m}
DES Data									
3×2pt	$0.781_{-0.020}^{+0.021}$ (0.778)	$0.325_{-0.035}^{+0.032}$ (0.329)	$0.753_{-0.039}^{+0.035}$ (0.743)	$4.40_{-1.19}^{+0.57}$ (4.08)	—	—	$-1.12_{-0.20}^{+0.26}$ (-1.12)	—	1584 168
3×2pt (NL Bias)	$0.778_{-0.018}^{+0.020}$ (0.798)	$0.317_{-0.032}^{+0.031}$ (0.324)	$0.760_{-0.040}^{+0.034}$ (0.768)	$4.34_{-1.18}^{+0.51}$ (4.51)	—	—	$-1.13_{-0.19}^{+0.24}$ (-0.89)	—	1790 194
DES Y3 3×2pt	$0.775_{-0.024}^{+0.026}$ (0.779)	$0.352_{-0.041}^{+0.035}$ (0.340)	$0.719_{-0.044}^{+0.037}$ (0.731)	—	—	—	$-0.98_{-0.20}^{+0.32}$ (-1.04)	—	1124 116
DES Y1 3×2pt	$0.782_{-0.024}^{+0.036}$ —	$0.284_{-0.030}^{+0.033}$ —	—	—	—	—	$-0.82_{-0.20}^{+0.21}$ —	—	—
DES all probes (-CL)	$0.797_{-0.012}^{+0.013}$ (0.802)	$0.317_{-0.014}^{+0.013}$ (0.307)	$0.776_{-0.025}^{+0.025}$ (0.792)	$4.39_{-0.85}^{+0.63}$ (4.61)	—	—	$-0.956_{-0.041}^{+0.044}$ (-0.936)	—	6584 1955
External Data									
Ext. Low- z	$0.794_{-0.019}^{+0.020}$ —	$0.296_{-0.008}^{+0.008}$ —	$0.799_{-0.018}^{+0.018}$ —	$5.42_{-0.55}^{+0.86}$ —	—	—	$-0.913_{-0.034}^{+0.037}$ —	—	6709 3655
CMB	$0.812_{-0.022}^{+0.015}$ (0.796)	$0.268_{-0.044}^{+0.011}$ (0.225)	$0.863_{-0.023}^{+0.051}$ (0.919)	$4.17_{-0.68}^{+0.15}$ —	$0.970_{-0.003}^{+0.003}$ (0.972)	—	$-1.238_{-0.192}^{+0.094}$ (-1.376)	< 0.28 (95% CL)	2181 524
Combined Data									
3×2pt + Ext. Low- z	$0.803_{-0.010}^{+0.009}$ —	$0.308_{-0.007}^{+0.006}$ —	$0.793_{-0.013}^{+0.013}$ —	$5.30_{-0.30}^{+0.72}$ —	$0.974_{-0.009}^{+0.024}$ —	—	$-0.962_{-0.029}^{+0.031}$ —	—	16046 5139
3×2pt + CMB	$0.801_{-0.011}^{+0.011}$ (0.806)	$0.280_{-0.025}^{+0.017}$ (0.274)	$0.831_{-0.023}^{+0.031}$ (0.844)	$4.40_{-0.39}^{+0.28}$ (4.34)	$0.972_{-0.003}^{+0.003}$ (0.973)	—	$-1.159_{-0.101}^{+0.100}$ (-1.139)	< 0.31 (95% CL)	5150 990
DES all probes (-CL) + CMB	$0.812_{-0.007}^{+0.009}$ —	$0.317_{-0.007}^{+0.007}$ —	$0.790_{-0.010}^{+0.012}$ —	$5.03_{-0.11}^{+0.10}$ —	$0.974_{-0.003}^{+0.003}$ —	$0.669_{-0.007}^{+0.007}$ —	$-0.978_{-0.027}^{+0.025}$ —	< 0.23 (95% CL)	17422 5449
3×2pt + All Ext.	$0.807_{-0.007}^{+0.007}$ —	$0.305_{-0.005}^{+0.004}$ —	$0.801_{-0.008}^{+0.008}$ —	$4.91_{-0.08}^{+0.07}$ —	$0.977_{-0.003}^{+0.003}$ —	$0.679_{-0.005}^{+0.005}$ —	$-0.981_{-0.022}^{+0.021}$ —	< 0.13 (95% CL)	32033 12970

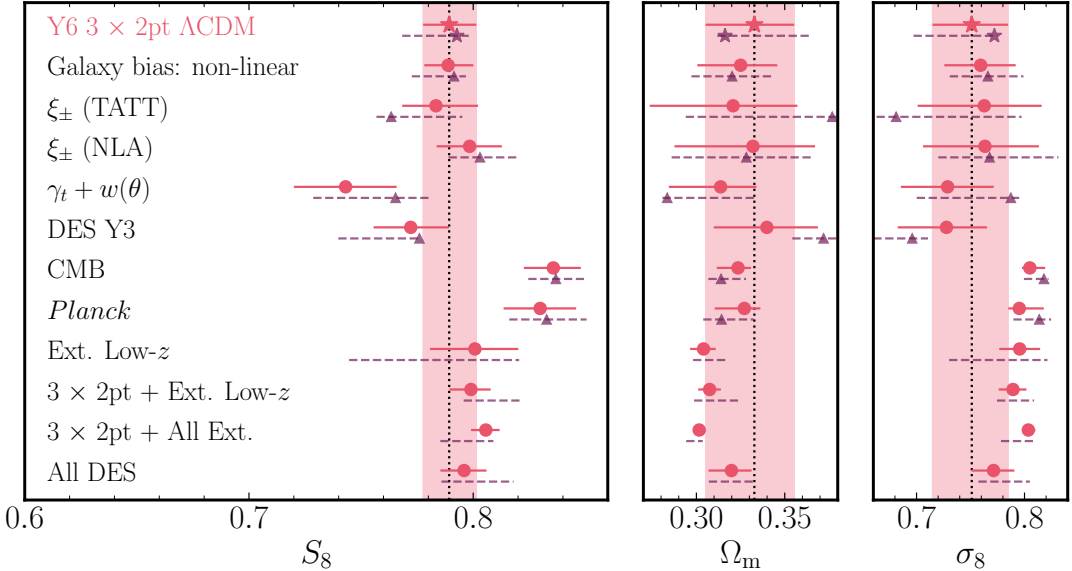


FIG. 8. Constraints on S_8 , Ω_m and σ_8 in Λ CDM – all constraints are shown as marginal 1σ constraints. In the first block, we show the DES Y6 3×2 pt results and its individual components, ξ_{\pm} and 2×2 pt. Second block shows the previous 3×2 pt results, from DES Y3. Third block shows the external constraints of CMB (both *Planck* and *Planck*+ACT+SPT). Final block shows the various combined results that include Ext. Low- z , DES 3×2 pt + Ext. Low- z , 3×2 pt + All Ext and lastly all DES probes. The pink circles and lines represent the marginalized mean and 68% uncertainty. The purple triangle and dashed lines for each row indicate the MAP with the projected joint highest posterior density (PJ-HPD), which is less sensitive to volume effects. [111]. For the filled triangles, the MAP estimate is obtained by running a minimizer. For the last four rows, corresponding to data combinations obtained from normalizing flows whose MAP estimates cannot be reliably determined, we only show the PJ-HPD.

approximately 16 million red and bright galaxies over $4,273 \text{ deg}^2$ and a redshift range of $0.6 < z < 1.2$, with an effective redshift of $z_{\text{eff}} = 0.85$. The BAO analysis combines three different estimators into a consensus measurement of the ratio of the angular distance (D_M) to the sound horizon scale (r_d) of $D_M(z_{\text{eff}})/r_d = 19.51 \pm 0.41$. This 2.1% measurement is the tightest BAO constraint from a photometric galaxy survey and competes in precision with Stage-III spectroscopic surveys. Interestingly, this measurement is in $\sim 2\sigma$ tension with the *Planck* 2018 best-fit – Λ CDM prediction of $D_M(z = 0.85)/r_d = 20.39$.

We note that the DES BAO measurement is not fully independent of DESI BAO, as the two surveys share $\sim 1,000 \text{ deg}^2$. In a followup work [115], we reanalyze the DES BAO in the area that does not overlap with DESI, using the angular correlation function, finding $D_M(z = 0.85)/r_d = 19.74 \pm 0.60$. This new measurement, although looser, is fully independent of DESI. We will hence use this when combining DES BAO with DESI BAO in the next section, and denote this result as “DES BAO (excl. DESI)”.

- **DES SN:** The DES supernovae type Ia (SNe Ia) dataset used here is the “DES-Dovekie” SN Ia sample [116], which is a reanalysis of the original DES-SN5YR [12, 117, 118] SN Ia light curves with updated photometric cross-calibration, among other improvements [116]. This new sample contains 1623 likely SNe Ia from the

full DES supernova survey, combined with approximately 200 SNe from historical low-redshift samples. The pipeline and sample building papers are described in [116]. These data were used to constrain cosmology assuming a time-evolving dark energy equation of state in [14], in combination with CMB and DESI BAO, finding a reduced tension with Λ CDM (3.2σ) vs. the same data combination using the original DES-SN5YR data (4.2σ).

- **DES CL:** The latest galaxy cluster constraints are based on REDMAPPER clusters [119] from the Y3 data. This red-sequence-based optical cluster finder extracted $\sim 16,000$ galaxy clusters in the DES Y3 footprint above richness of 20 and in the redshift range $0.2 < z < 0.85$. In DES Y1 [120], it was found that REDMAPPER clusters suffer from line-of-sight projection effects, where interloper galaxies contaminate the richness estimation by 20-40% and bias the lensing results. This effect was later studied in [121–124]. In DES Y3, we took the alternative approach of discarding the small-scale information that suffers from projection effects. Three additional two-point functions that include cluster density δ_c were added to the standard 3×2 pt analysis: $\langle \delta_c \delta_c \rangle$, $\langle \delta_c \delta_g \rangle$, $\langle \delta_c \gamma_t \rangle$. This methodology was first developed in DES Y1 [28, 125] and applied to DES Y3 data in [126]. It was found that adding galaxy clusters mainly helps in constraining Ω_m (by $\sim 25\%$) and that clusters prefer a slightly lower value of Ω_m .

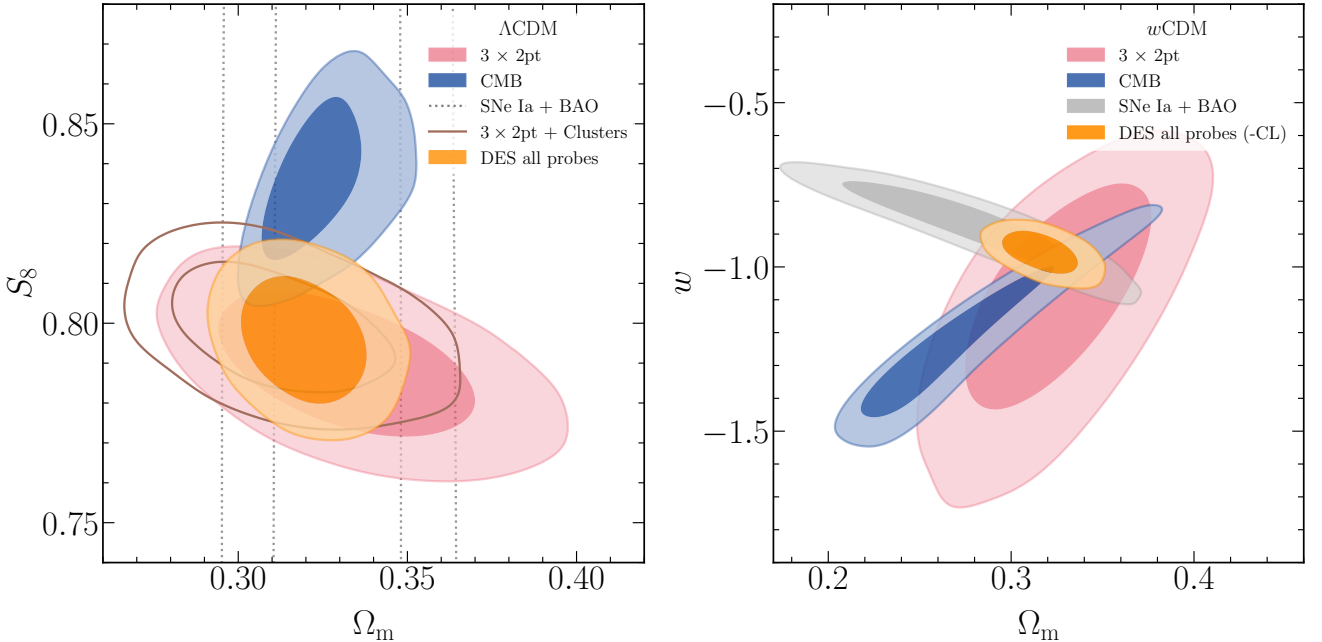


FIG. 9. Combination of all the DES cosmological probes in the Λ CDM (left panel) and w CDM (right panel) models. We show marginalized constraints on parameters from large-scale structure and weak lensing (3×2 pt; pink), type Ia supernovae combined with BAO (black dotted/gray), galaxy cluster clustering and number counts combined with 3×2 pt (brown). The combination of DES Y6 3×2 pt, Clusters, SNe Ia, and BAO is shown in orange (All DES). Blue contours correspond to CMB constraints from Planck, ACT and SPT combined. The combination of DES probes is consistent with CMB at the 2.8σ level in Λ CDM and 2.5σ in w CDM in full parameter space.

One important note is that in [126], the galaxy samples used in the 3×2 pt block were the same as those used for cross-correlation with clusters. This means that several shared nuisance parameters, in particular the mass-observable relation, can be self-calibrated. Here, however, the Y3 source and lens samples are different from the Y6 ones. This means that the combination does not invoke self-calibration. In addition, to be conservative, we only use the part of the data vector in [126] that does not overlap with the Y6 3×2 pt data vector.⁸ Both of these factors result in less constraining power gain when combining with clusters compared to what is shown in [126], but we nevertheless found that there is an impact from including the cluster information ($\sim 16\%$ tighter Ω_m constrain). In addition, we assume the correlation of the Y6 3×2 pt and the Y3 cluster likelihood is small (the later being dominated by shape/shot noise) and we use normalising flows to combine them (see Section IV D).

In an upcoming paper [48], we will present a complete self-calibrating analysis that updates the cross-correlations between the Y3 cluster sample and the Y6 lens and source samples.

In the left panel of Figure 9, we show the individual and combined constraints for Λ CDM from the four DES probes: DES Y6 3×2 pt, DES BAO, DES SN and DES CL. We find

$$\begin{aligned} S_8 &= 0.794^{+0.009}_{-0.012}, \\ \Omega_m &= 0.322^{+0.012}_{-0.011}, \\ \sigma_8 &= 0.766^{+0.017}_{-0.022}. \end{aligned} \quad (24)$$

Combining the four probes results in a 1.3% constraint on S_8 , which is comparable in precision to the constraint from the primary CMB. The $\text{FoM}_{\sigma_8, \Omega_m}$ of the four DES probes and primary CMB are also very similar, 8721 and 8994, respectively. We note that these are the first cosmological constraints combining all four dark energy probes from a single experiment, an important milestone for Stage-III dark energy experiments. Comparing between the different probes, we see that S_8 is primarily constrained by 3×2 pt, SN+BAO places a strong constraint on Ω_m , and clusters contribute to a small shift and tightening in the Ω_m direction. The addition of the other probes to 3×2 pt pulls the Ω_b constraint against the lower prior edge. All four probes appear fully consistent in this parameter space, and we confirm this fact quantitatively in Table VI, where different combinations of DES probes are always consistent to within $\lesssim 2\sigma$.

Comparing the four DES probes and the CMB constraints, we see that in the $S_8 - \Omega_m$ plane the 2σ contours overlap. Quantitatively, we find a 2.8σ parameter differences in the full parameter space between the combination of all DES probes and the CMB. Compared to the case with only 3×2 pt in Sec-

⁸ Specifically, the cluster (CL) likelihood we use to combine with Y6 3×2 pt includes Y3 $\langle \delta_c \delta_g \rangle$, $\langle \delta_c \gamma_t \rangle$ and number counts (N), and ignores Y3 clustering $\langle \delta_g \delta_g \rangle$.

TABLE VI. Consistency of various independent data sets, in units of σ , as introduced in Sec. IV F, with a derived probability-to-exceed shown in parentheses. In the table below, “DES all probes” stands for the data combination used in Section VI: DES Y6 3×2 pt, DES BAO, DES SN, DES CL; “CMB” stands for the CMB combination described in Section VII: *Planck* 2018, ACT DR6, SPT-3G DR1, primary without lensing; “Ext. Low- z ” represents the combination of the most constraining low-redshift data described in Section VII: DESI DR2 BAO, DES BAO (excl. DESI), DES SN, SPT CL.

Dataset 1	Dataset 2	Parameter difference
ΛCDM		
<i>DES internal consistency</i>		
DES 3×2 pt	DES SN + BAO	0.35 (0.725)
DES 3×2 pt	DES CL	2.0 (0.042)
DES 3×2 pt + CL	DES SN + BAO	0.31 (0.753)
DES 3×2 pt + SN + BAO	DES CL	0.51 (0.61)
<i>DES consistency with external data</i>		
DES 3×2 pt	Planck	1.0 (0.319)
DES 3×2 pt	CMB	1.8 (0.08)
DES 3×2 pt + CL	CMB	2.0 (0.042)
DES 3×2 pt + SN + BAO	CMB	2.5 (0.012)
DES all probes	CMB	2.8 (0.006)
DES 3×2 pt	Ext. Low- z	0.2 (0.843)
DES 3×2 pt + Ext. Low- z	CMB	2.3 (0.021)
wCDM		
DES 3×2 pt	CMB	1.3 (0.186)
DES 3×2 pt	DES SN + BAO	0.34 (0.73)
DES 3×2 pt + SN + BAO	CMB	2.5 (0.012)
DES 3×2 pt	Ext. Low- z	1.1 (0.284)
DES 3×2 pt + Ext. Low- z	CMB	2.4 (0.015)

tion V A 1, it is interesting that the addition of DES BAO, SN and CL increased the strength of differences with CMB. We further break down the different components and calculate the consistency between the different DES probes in Table VI. We find that 3×2 pt+SN+BAO gives 2.5σ , while clusters increase the tension slightly. It is not clear that there is a specific DES probe that drives the overall difference with the CMB.

When combining all DES probes with the primary CMB, we find further improvements in all parameters, with $S_8 = 0.815^{+0.008}_{-0.007}$, $\Omega_m = 0.314^{+0.006}_{-0.007}$. The $\text{FoM}_{\sigma_8, \Omega_m}$ increases to 20590, which is a more than $2\times$ gain over the CMB $\text{FoM}_{\sigma_8, \Omega_m}$.

For w CDM, we combine three of the four probes: DES Y6 3×2 pt, DES BAO and DES SN. As the DES clusters analysis of [126] did not test the pipeline in w CDM, we choose to be conservative and omit it in this combination. In a forthcoming paper we will present dark energy constraints including DES clusters [48]. The combined constraints are shown in the right panel of Figure 9. We find $w = -0.956^{+0.044}_{-0.041}$, $\Omega_m = 0.317^{+0.013}_{-0.014}$ and $S_8 = 0.797^{+0.013}_{-0.012}$. Similar to before, we find no evidence for departure from a cosmological constant of $w = -1$, now with a constraint on w tighter than 5%. This is more than twice as constraining as the equivalent constraint in DES Y3 at $w = -0.84^{+0.11}_{-0.10}$, where we combined the mid-survey (DES Year 3) versions of the 3×2 pt [37], SN [127], and BAO [128]. We also do not find a significant pref-

erence of w CDM over Λ CDM (0.5σ) when doing model comparison via $\Delta\chi^2$.

Comparing the different probes, degeneracy-breaking is effective between 3×2 pt and SN+BAO – the degeneracy directions in the $w - \Omega_m$ plane for the two sets of contours are orthogonal, resulting in the tight constraint when combining. The FoM_{w, Ω_m} goes from 168 to 1955 when 3×2 pt is combined with SN+BAO, a more than $10\times$ gain. Compared to the primary CMB constraints, we find that the parameter difference in the full w CDM parameter space is 2.5σ , consistent with the Λ CDM case.

VII. COMBINATION WITH EXTERNAL PROBES

In this section we present results from comparing and combining the 3×2 pt constraints from this work with other external datasets to achieve the tightest cosmological constraints to date. In particular, we use the following external likelihoods:

- *CMB*: We use a combination of TT, EE and TE primary CMB power spectrum measurements from *Planck* 2018 [1], Atacama Cosmology Telescope (ACT)-DR6 [3] and South Pole Telescope (SPT)-3G DR1 [4] experiments. We combine the following likelihoods:

- *Planck* 2018 (PR3 combination – `Plik` likelihood with Legacy maps) *lite* likelihood with $2 < \ell_{\text{TT}} < 1000$ for TT spectra (including two low- ℓ TT bins as described in [129]) and $30 < \ell_{\text{TE,EE}} < 600$ for TE and EE spectra. When used with these cuts and in combination with ground-based CMB data, this is expected to be entirely consistent with the more recent ‘PR4’ *Planck* result from `CamSpec` likelihood with `NPipe` maps [130].
- *Planck* 2018 (simall) likelihood with $2 < \ell_{\text{EE}} < 30$ for low- ℓ polarization information, necessary to constrain the optical depth to reionisation τ . We note that other analyses have used the *Planck* SRoll2 low- ℓ EE likelihood [131, 132], which disfavors lower values of τ and various authors (e.g., [133, 134]) have pointed out that this choice can affect (although not to high significance) the level of consistency of combined data sets with Λ CDM.
- ACT-DR6 *lite* likelihood with $600 < \ell_{\text{TT}} < 8500$ for TT spectra and $600 < \ell_{\text{TE,EE}} < 8500$ for TE and EE spectra [3].
- SPT-3G DR1 *lite* likelihood with `cand1` [135] `SPT3G_D1_TnE` data using $400 < \ell_{\text{TT}} < 3000$ for TT spectra and $400 < \ell_{\text{TE,EE}} < 4000$ for TE and EE spectra.

We follow the official ACT analysis of [3] in ignoring the covariance between ACT-DR6 and *Planck* in the overlapping multipole range, which was not found to affect results. Likelihoods referred to as *lite* include a pre-marginalisation over nuisance parameters which

model microwave foregrounds. Residual uncertainties are modeled using amplitude parameters A_{CMB} (which is shared across ACT and *Planck* likelihoods so that $A_{\text{ACT}} = A_{\text{Planck}}$ as in [3]), T_{cal} (for SPT-3G), and a polarization calibration parameter P_{ACT} (in the ACT part of the likelihood) and E_{cal} (in the SPT-3G part of the likelihood).

We do not combine the DES constraints with the CMB lensing likelihood from these experiments, as the DES $3 \times 2\text{pt}$ is not independent of the CMB lensing information. A proper combination will need to take into account the cross-correlation [136].

- **DESI BAO:** We use BAO measurements from the Dark Energy Spectroscopic Instrument (DESI) Data Release 2 [137] covering an effective redshift range $0.295 < z < 2.330$. More explicitly, we include isotropic BAO scaling parameters measured for the BGS sample, and both isotropic and Alcock-Paczynski scaling parameters for the LRG1, LRG2, LRG3+ELG1, ELG2, QSO and Lyman- α samples.
- **SPT CL:** We use the constraints derived from cluster abundance with SPT described in [50]. The constraint uses a cluster sample constructed from a combination of SPT-SZ, SPTpol ECS and SPTpol 500d data, which comprises of 1,005 clusters in the redshift range $0.25 < z < 1.78$. The cluster masses are calibrated via a combination of DES Y3 and HST weak lensing data.
- **BBN:** Big Bang Nucleosynthesis (BBN) theory predicts the abundance of light elements in the early Universe, such as deuterium and helium, as well as their relation to the baryon-to-photon ratio. Therefore, the observational determination of the primordial deuterium abundance and the helium fraction can be used to compute the physical baryon density parameter today, $\Omega_b h^2$. We employ a BBN $\Omega_b h^2 = 0.02218 \pm 0.00055$ constraint from a recent analysis [138] that recalculates the predictions while marginalizing over uncertainties in reaction rates in the standard ΛCDM model. We mainly use this likelihood to derive constraints on the Hubble parameter in Sec. VII F.

In addition to the above external likelihoods, when combining with supernova data, we use the DES SN described in Section VI as that is the most constraining supernova dataset to date. We also combine with DES BAO (excl. DESI), which is the DES BAO excluding objects that overlap with DESI, as described in the previous section.

A. Early vs. late universe

We now combine our DES Y6 $3 \times 2\text{pt}$ results with the most constraining combination of internal and external cosmological probes. Specifically, we first look at the combination we call “Ext. Low- z ”, which consists of, from the list above, DESI BAO, DES Y6 BAO (excl. DESI), DES SN and SPT

CL. Figure 10 plots the results of combining our $3 \times 2\text{pt}$ results with Ext. Low- z , for ΛCDM and $w\text{CDM}$. The constraints are listed in Table IV.

We find the tightest constraints from the low- z universe in ΛCDM to be $S_8 = 0.799_{-0.010}^{+0.009}$, $\Omega_m = 0.308_{-0.006}^{+0.006}$ and $\sigma_8 = 0.789_{-0.013}^{+0.012}$.

In particular, adding $3 \times 2\text{pt}$ to Ext. Low- z results in a $2.4 \times$ gain in the $\text{FoM}_{\sigma_8, \Omega_m}$.

From Figure 10 it can be clearly seen that, as expected, $3 \times 2\text{pt}$ contributes mostly in constraining the structure growth, or S_8 , while Ext. Low- z provides strong constraining power in Ω_m , primarily driven by the BAO and SN measurements, as seen in Figure 12. The external constraint on Ω_m , as well as the $\text{FoM}_{\sigma_8, \Omega_m}$, are about $2 \times$ better here than the DES-only low-redshift constraints, mostly due to the addition of DESI BAO.

The right panel of Figure 10 shows the $w\text{CDM}$ constraints combining all these datasets. In this model we find $w = -0.962_{-0.029}^{+0.031}$ and $\Omega_m = 0.308_{-0.007}^{+0.006}$.

This is a 3% constraint on w , and is still consistent with the cosmological constant ($w = -1$). Overall, the DES $3 \times 2\text{pt}$ mostly impacts the constraint on S_8 , but also moves Ω_m to slightly higher values compared to the Ext. Low- z probes, increasing the consistency with the primary CMB in the $w - \Omega_m$ plane.

In Figure 10 we also overlay the primary CMB constraints for ΛCDM and $w\text{CDM}$. The comparison with $3 \times 2\text{pt}$ + Ext. Low- z represents our best understanding of the two models from the late and early universe. We find a 2.3σ difference between the $3 \times 2\text{pt}$ + Ext. Low- z results and the CMB when considering the full parameter space for ΛCDM , and 2.4σ for $w\text{CDM}$. While these numbers do not indicate a significant tension between the low- and high-redshift universe, it is worth noting that they are all higher than the values seen in DES Y3 [37]. As discussed in Section V A 1, this is partially driven by the combined CMB constraints.

B. Joint cosmological constraints in ΛCDM and $w\text{CDM}$

We now combine DES Y6 $3 \times 2\text{pt}$ + Ext. Low- z and CMB to obtain the final joint constraint. This produces the tightest ΛCDM joint constraint from all major cosmic surveys to date. We show the $S_8 - \Omega_m$ projection of this constraint in the left panel of Figure 10, but will examine the other projections in the sections below. It is worth noting that there is nontrivial degeneracy breaking when combining such a complex set of data in this high-dimensional space.

We find the tightest constraints available in ΛCDM to be

$$\begin{aligned} S_8 &= 0.806_{-0.007}^{+0.006}, \\ \Omega_m &= 0.302_{-0.003}^{+0.003}, \\ \sigma_8 &= 0.804_{-0.006}^{+0.007}. \end{aligned} \quad (25)$$

This combination has a $\text{FoM}_{\sigma_8, \Omega_m}$ of 51955, 7.4 times larger than $3 \times 2\text{pt}$ + Ext. Low- z alone, and a factor of 1.5 larger than the previous most constraining combination we presented four years ago with DES Y3 [37]. In that work, we combined the

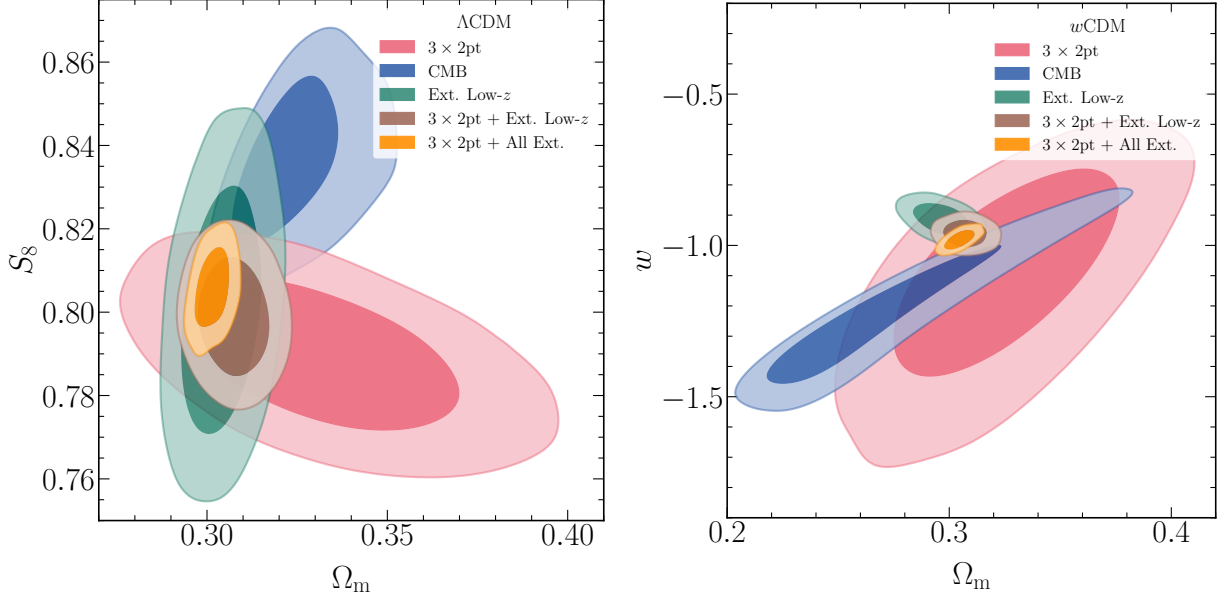


FIG. 10. Λ CDM (left) and w CDM (right) constraints for DES Y6 3×2 pt combined with other low redshift external probes. The primary CMB constraints are shown in blue, and combining DES Y6 3×2 pt, external low-redshift probes and the CMB gives the orange contours.

DES Y3 3×2 pt with eBOSS BAO and RSD, Pantheon SN and CMB constraints from *Planck* 2018. The subsequent upgrades in each of the physical probes together contribute to this gain. Interestingly, this combination also results in S_8 shifting lower by about 0.6σ compared to our result in Y3. Given that the CMB constraints shifted to higher S_8 values from *Planck* to the joint *Planck*+ACT+SPT combination that is used in this work, this suggests that the low-redshift constraints now have substantially greater impact on the joint constraints.

Since we are considering a flat universe, a constraint on Ω_m translates directly into a constraint on the dark-energy density parameter, giving $\Omega_\Lambda = 0.698^{+0.003}_{-0.003}$ and $\Omega_\Lambda h^2 = 0.326^{+0.004}_{-0.004}$. In physical units this translates to $\rho_\Lambda = 6.120^{+0.075}_{-0.069}$. The equivalent value of the cosmological constant itself is $\Lambda = 8\pi G \rho_\Lambda = 1.027^{+0.013}_{-0.012} \times 10^{-35} \text{ s}^{-2}$ or in distance units $\Lambda/c^2 = 1.14^{+0.014}_{-0.028} \times 10^{-56} \text{ cm}^{-2}$.

In w CDM we show the best constraining combination in the right panel of Figure 10 for the $w - \Omega_m$ plane. We find:

$$w = -0.981^{+0.021}_{-0.022}, \quad \Omega_m = 0.305^{+0.004}_{-0.005}, \quad (26)$$

a 2% constraint on w that is consistent with the cosmological constant ($w = -1$).

C. Comparison of lensing probes

In this section we compare our 3×2 pt results with results from other Stage-III lensing analyses: the Kilo-Degree Survey [KiDS, 38] and the Hyper Suprime-Cam Subaru Strategic Program [HCS-SSP, 40]. A quantitative evaluation of the consistency of the three Stage-III results is not straightforward

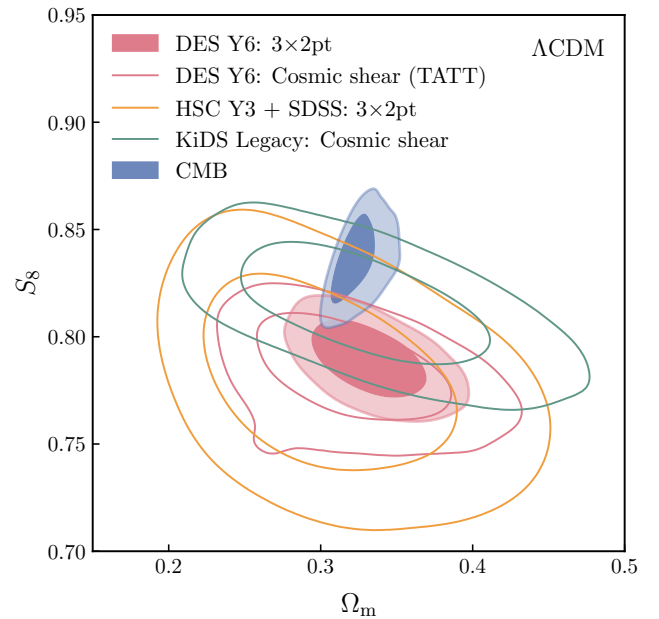


FIG. 11. Comparison of $S_8 - \Omega_m$ for the main Stage-III lensing surveys. Here we select the results from each survey that is most comparable to either our 3×2 pt or cosmic shear analysis. For KiDS, we show the KiDS-Legacy cosmic shear constraints [7] (green). For HSC, we show the 3×2 pt constraints from [45] (orange).

because of the numerous differences in model choices, scale cuts, and analysis techniques, and multiple results from each collaboration. We plot here results that are representative of each collaboration’s constraints on structure growth.

For KiDS, the most recent $3\times 2\text{pt}$ results come from [39], where the lensing data from the 1000 degree² KiDS survey were combined with spectroscopic data from BOSS and 2dFlens to form the $3\times 2\text{pt}$ data vector. Since then, KiDS made significant updates to their shear catalog, resulting in the KiDS-Legacy cosmic shear results [7]. Given the update, we show the KiDS-Legacy cosmic shear constraints in Figure 11 (green), and compare it to both the DES Y6 $3\times 2\text{pt}$ and the cosmic shear results (pink solid and open, respectively). We find that the constraining powers of KiDS-Legacy and DES Y6 from cosmic shear are similar, and the constraints are consistent: $S_8 = 0.815^{+0.016}_{-0.021}$ (KiDS) and $S_8 = 0.783^{+0.019}_{-0.015}$ (DES). DES $3\times 2\text{pt}$ provides tighter constraints primarily in the Ω_m direction but also in S_8 . It is also interesting to observe from Figure 11 that the degeneracy direction in this parameter plane is similar, as expected from the similar redshift range of the shear catalogs.

For HSC Y3, three versions of the $3\times 2\text{pt}$ analysis were carried out. All of them use the SDSS DR11 spectroscopic galaxies as the lens sample, as opposed to DES’s photometric lenses. In [43] (referred to as the large-scale analysis), the authors computed the matter power spectrum using a standard Boltzmann code (similar to DES’s use of CAMB), but employed a halo model to describe both nonlinear structure formation and galaxy bias [44] contrasting with DES Y6’s perturbative bias models combined with conservative scale cuts to avoid halo-model systematics. In [44], an emulator trained on simulations was used to model smaller scales, yielding tighter constraints in Ω_m . However, the latest analysis of [45] is most similar to this work in three key respects: it employs tomographic binning of the source sample (rather than a single redshift bin), applies conservative scale cuts determined by theory uncertainties (similar to [Y6MODEL]), and uses simple perturbative bias models without relying on halo model predictions for small-scale clustering. We show their constraint in Figure 11 in orange. Due to the smaller survey area (416 deg²), HSC Y3 constraints are substantially wider, $S_8 = 0.804^{+0.051}_{-0.051}$. They are also consistent with the DES results. We note that in Figure 11 we plot directly the published chains from each survey, instead of a matched re-analysis of their data. We leave a more detailed comparison with unified analysis choices [e.g. 139–142] for future investigation.

In summary, the final DES $3\times 2\text{pt}$ and cosmic shear analyses yield cosmological constraints in the $S_8 - \Omega_m$ plane that are consistent with the latest results from the other Stage-III weak-lensing surveys. Overall, the marginalized posteriors in this parameter space from all the weak lensing surveys are also consistent with the CMB, though the inferred S_8 from lensing remains systematically slightly lower than that inferred from CMB measurements. KiDS-Legacy finds the highest S_8 values, while DES $3\times 2\text{pt}$ gives the tightest S_8 constraint with the highest significance of deviation from CMB, but still below 3σ .

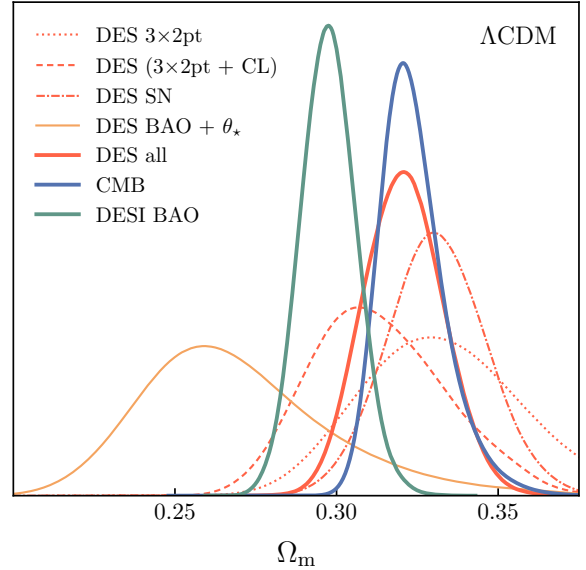


FIG. 12. Marginalized constraints on the total amount of matter Ω_m in the ΛCDM model from different DES probes and their combination, compared to CMB and DESI BAO. “DES all” includes Y6 $3\times 2\text{pt}$, SN, BAO, and Clusters. We obtain excellent agreement between “DES all” and CMB.

D. Constraints on the total amount of matter

The possibility of dynamical dark energy (DDE) has attracted considerable attention following recent measurements, with several studies attributing this preference to underlying Ω_m tensions between probes [e.g. 143]. Initial hints of tension within ΛCDM emerged from the combination of DES SN with BOSS BAO [12], which showed significant Ω_m disagreement. The DESI DR1 [13] and DR2 BAO measurements [137], when combined with type Ia supernovae data and CMB constraints, strengthened this evidence, yielding indications for DDE within the $w_0 - w_a$ CDM framework at the $\sim 3\sigma$ level. These analyses found SN measurements yielded higher Ω_m values than CMB, which in turn yielded higher values than BAO. The recent recalibration of DES SN [116] finds a $\sim 1\sigma$ lower Ω_m value, though still higher than BAO predictions.

In Figure 12, we compare the marginalized Ω_m constraints inferred from DES probes – including $3\times 2\text{pt}$, SN, BAO and CL – and assess their level of agreement with DESI BAO and CMB constraints. Our DES $3\times 2\text{pt}$, SN and CL results are in excellent agreement with the CMB, while DES BAO+ θ_* yields a lower result.⁹ All combined and without the θ_* prior, the DES probes find very good agreement with the CMB and are at 1.7σ difference from DESI BAO. A more rigorous and

⁹ For the DES BAO only case, we apply the θ_* prior to obtain an Ω_m constraint. θ_* is the angular scale of the acoustic peak, which isolates the geometric/background information from the CMB. We incorporate this via a Gaussian likelihood taken from the *Planck* 2018 temperature and polarization data [1], with $100\theta_* = 1.04109 \pm 0.00030$.

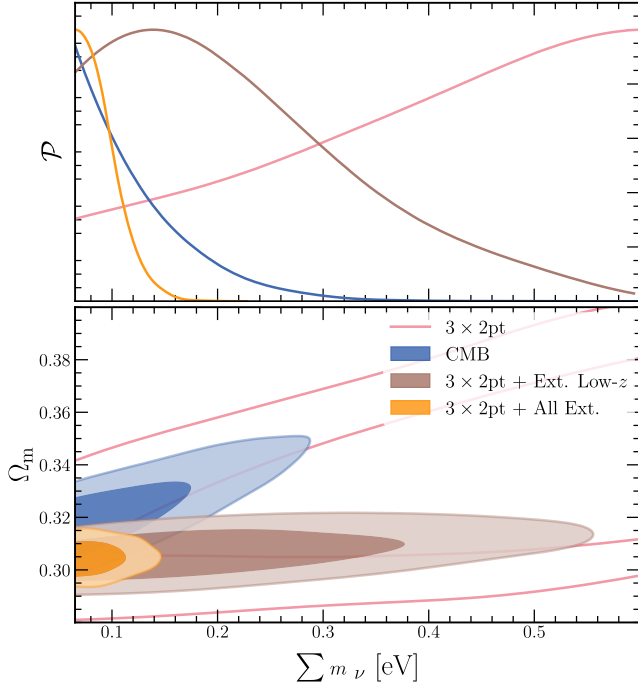


FIG. 13. Constraints on the sum of neutrino mass coming from the DES Y6 $3 \times 2\text{pt}$ and combination with other low- and high-redshift external probes. We note that all chains presented here contain a top-hat prior of $\sum m_\nu \in [0.06 - 0.6] \text{ eV}$.

complete comparison of geometric vs. growth probes will be explored in the forthcoming paper [11].

E. Neutrino mass

Figure 13 shows the marginalized constraints on the sum of neutrino masses $\sum m_\nu$ and the matter density Ω_m in flat ΛCDM , from our fiducial $3 \times 2\text{pt}$, CMB, $3 \times 2\text{pt+Ext. Low-}z$ and $3 \times 2\text{pt+All Ext.}$ As in Y3 [37], the $3 \times 2\text{pt}$ analysis alone does not provide a meaningful constraint on $\sum m_\nu$, and the marginalized posterior remains bounded by the adopted prior range of $0.06 \text{--} 0.6 \text{ eV}$. Our measurement of Ω_m peaks in a region that is consistent with the CMB value, unlike the BAO case where Ω_m is significantly lower than the CMB (Figure 12). This lower preference for Ω_m drives the joint neutrino constraints (orange contour in Figure 13) toward the lower boundary [144, 145], due to the degeneracy between Ω_m and $\sum m_\nu$.

The CMB (as defined in Section VII) alone yields an upper limit of $\sum m_\nu < 0.24 \text{ eV}$ (95% CL), while the inclusion of DES $3 \times 2\text{pt}$ slightly tightens this constraint to $\sum m_\nu < 0.22 \text{ eV}$. When combining DES $3 \times 2\text{pt}$ with the external low-redshift (Ext Low- z) probes, we obtain an upper bound of $\sum m_\nu < 0.47 \text{ eV}$. When we further combine this with the CMB, we find $\sum m_\nu < 0.14 \text{ eV}$, with an improvement due to the different Ω_m - $\sum m_\nu$ degeneracies of high- z and low- z probes (cf. Figure 13). This upper limit is noticeably weaker than the one reported by the DESI Collaboration us-

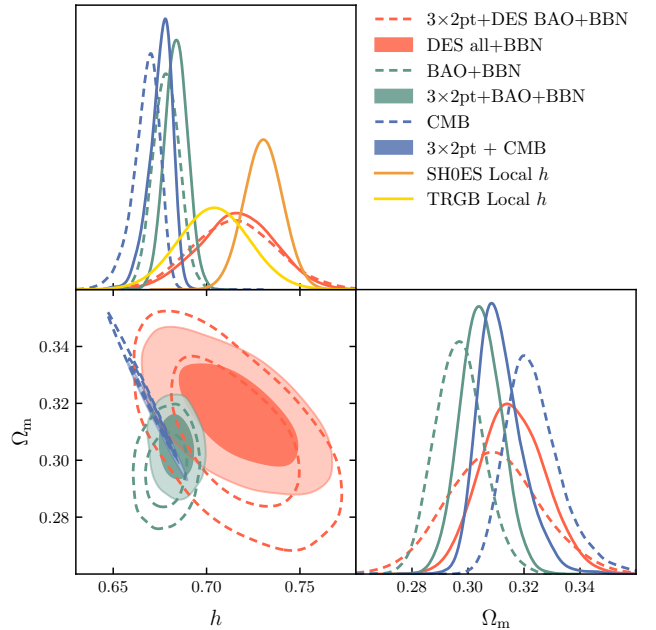


FIG. 14. Marginalized constraints on the Hubble parameter h and the total amount of matter Ω_m in the ΛCDM model compared to local measurements of h . The ‘‘BAO’’ label denotes the combination of DESI DR2 BAO and DES BAO measurements, with overlapping regions removed from the DES dataset.

ing DESI DR2 combined with the CMB (without lensing), $\sum m_\nu < 0.067 \text{ eV}$ [95% CL, 137]. The main reason is that we adopt physical priors that include the lower bound of 0.06 eV imposed by neutrino oscillation experiments [146], instead of the commonly used minimal mass of zero. Yet, the trend in our combined result remains consistent with external constraints, as the posterior in the ΛCDM framework consistently peaks at the lower prior boundary [144, 145].

All the marginalized neutrino constraints in ΛCDM are reported in Table IV.

F. Constraints on Hubble parameter

Next we consider the Hubble parameter evaluated at the present time, $H_0 = 100h \text{ km s}^{-1} \text{ Mpc}^{-1}$, motivated by significant tensions observed between different measurements.

Multiple direct local measurements prefer a higher value of the expansion rate than that inferred from the primary CMB, most prominently the $h = 0.7304 \pm 0.0104$ constraint from the SH0ES team [147] based on an astronomical distance ladder using Cepheid variables, and $h = 0.704 \pm 0.019$ [148] using the Tip of the Red Giant Branch (TRGB) method [148].

In the ΛCDM model, some of these local measurements stand in contrast to constraints from the CMB by *Planck* + ACT + SPT, which prefer $h = 0.667^{+0.009}_{-0.006}$, a 4.6σ tension in the 1D h projection compared to the SH0ES result, while consistent at 1.6σ with the TRGB result. This value comes from reanalyzing the relevant likelihood with our priors, including

varying neutrino masses, from Table IV and our sampler.

In Figure 14 we explore what DES $3\times 2\text{pt}$ adds to this picture. While $3\times 2\text{pt}$ provides only weak direct constraints on h , its strong constraining power on other cosmological parameters—especially Ω_m —helps break parameter degeneracies when combined with the CMB. When we combine $3\times 2\text{pt}$ with CMB data, we find $h = 0.675^{+0.007}_{-0.004}$, which is both more constraining and slightly higher than the CMB-only value. This upward shift arises primarily because $3\times 2\text{pt}$ prefers a lower Ω_m , which in turn pushes h upward through the degeneracy between these parameters. Due to this shift to higher h , since the uncertainties are smaller, the tension with local Universe measurements remains practically unchanged from the CMB-only case.

We can also constrain the value of h independently of CMB data using a combination of BAO and BBN constraints on $\Omega_b h^2$, which yields $h = 0.678 \pm 0.007$ when using DESI DR2 BAO + DES BAO (excl. DESI). When adding DES $3\times 2\text{pt}$ measurements, we also find a slightly more constraining and higher value of $h = 0.684 \pm 0.006$. These constraints are tighter than CMB-derived values, and are in 3.9σ tension with the local SHOES measurement, 5.1σ tension with the consensus H_0 , and 1.0σ agreement with TRGB.

For the first time, we can also obtain an independent measurement of h just from DES data ($3\times 2\text{pt}$ +SN+BAO+CL) and BBN: $0.715^{+0.021}_{-0.019}$, which is consistent with and as constraining as the most recent measurement reported by the TRGB method, with a 2.3σ shift compared with CMB. This is because DES $3\times 2\text{pt}$ constrains Ω_b to be slightly lower than the CMB-preferred value, which leads to higher h through the BBN prior. While the DES-based constraint is slightly higher in h when combined with BBN compared to the combination including DESI BAO, the two constraints are still consistent.

Strong lensing time-delay measurements can also constrain H_0 , albeit with larger uncertainty at current precision levels. From the recent TDCOSMO results [6], we find consistent results ($h = 0.727^{+0.048}_{-0.036}$) when reanalyzing their likelihood with our priors and sampler. When combined with $3\times 2\text{pt}$ data, we obtain a tighter constraint on H_0 with a slightly lower value of $h = 0.715 \pm 0.033$, primarily due to breaking degeneracies in the Ω_m direction. This result is consistent with the fiducial value reported by TDCOSMO Collaboration [6] of $h = 0.716^{+0.039}_{-0.033}$, obtained when combining the TDCOSMO-2025 sample with Ω_m constraints from the Pantheon+ SN Ia dataset.

VIII. CONCLUSIONS

In this paper we present the ΛCDM and $w\text{CDM}$ constraints from the DES Y6 $3\times 2\text{pt}$ analysis, combining three two-point functions of galaxy clustering and galaxy weak lensing. This result combines the full six-year DES data of 140 million weak lensing source galaxies and 9 million lens galaxies, covering roughly $4,300 \text{ deg}^2$. It rests atop 18 other supporting papers that describe components that went into this analysis, as well as the prior $3\times 2\text{pt}$ analyses from DES in Year 1 [36] and Year 3 [37].

We carry out extensive testing of our data and methodology in this paper, and in the 18 supporting papers, to ensure the robustness of the results. In addition, the combination of the three two-point functions naturally provides a self-calibration mechanism to safeguard against a number of systematic effects.

Assuming ΛCDM cosmology and linear galaxy bias, the DES Y6 $3\times 2\text{pt}$ analysis yields $S_8 = 0.789^{+0.012}_{-0.012}$ and $\Omega_m = 0.333^{+0.023}_{-0.028}$. This is a factor of two increase in constraining power compared to DES Y3, and rivals state-of-the-art CMB constraints in the S_8 direction, which measures the clustering amplitude of cosmic structure. Comparing with the latest CMB constraints from temperature and polarization based on a combination of SPT-3G DR1, ACT-DR6, and *Planck* 2018, we find a full parameter space difference of 1.8σ . When projected onto S_8 , i.e., focusing on growth of structure, the difference increases to 2.6σ , with DES preferring a lower value. The full parameter difference reduces to 1.0σ when considering *Planck* 2018 only, due both to *Planck* 2018 preferring lower S_8 values on its own than when combined with other CMB data, and to decreased uncertainties from the combined CMB dataset. The full parameter difference between DES Y3 $3\times 2\text{pt}$ and *Planck* 2018 is 1.5σ .

We then combine, for the first time, the four dark energy probes that were proposed at the inception of DES [15]: galaxy clusters, BAO, SN Ia and $3\times 2\text{pt}$. While we perform this combination in a sub-optimal way because the cluster analysis uses a different source population than the $3\times 2\text{pt}$ analysis, we still find improvement in the cosmological constraints, especially in Ω_m , when combining all probes compared to $3\times 2\text{pt}$. We find $S_8 = 0.794^{+0.009}_{-0.012}$ and $\Omega_m = 0.322^{+0.012}_{-0.011}$. This DES-only constraint is consistent at 2.8σ with the primary CMB constraints in the full parameter space. When combined with the CMB primary results, we find $S_8 = 0.815^{+0.008}_{-0.007}$ and $\Omega_m = 0.314^{+0.006}_{-0.007}$.

We also combine with a collection of external low- z probes (we refer to as Ext. Low- z), which include DESI BAO DR2, DES BAO (minus DESI overlap), DES SN, and SPT cluster abundances. We find further improvements in the cosmological constraints, though the S_8 constraint is still dominated by DES $3\times 2\text{pt}$. This combination is consistent with the CMB at the 2.3σ level, allowing us to combine them and achieve final constraints of 0.8% in S_8 and 1% in Ω_m .

We also explore $w\text{CDM}$ constraints for $3\times 2\text{pt}$ only, all DES probes, and combinations with external data. We find that marginalized w posteriors from all combinations are consistent with -1 . DES alone constrains w with better than 5% precision, while combining DES $3\times 2\text{pt}$ + Ext. Low- z + CMB results in 2% precision in w that is still consistent with -1 . We find no significant preference for $w\text{CDM}$ over ΛCDM from the $3\times 2\text{pt}$ data. Notably, the $2\text{--}3\sigma$ differences between low-redshift and CMB datasets persist comparably in both cosmological models, with full-parameter differences of 2.3σ for $3\times 2\text{pt}$ + Ext. Low- z (2.8σ for all DES probes) in ΛCDM and 2.4σ (2.5σ) in $w\text{CDM}$. This minimal extension to evolving dark energy density does not decrease the parameter differences observed in ΛCDM . We refer to [11] for exploration of alternative cosmological scenarios.

We discuss how the new 3×2 pt constraints from DES impact other Λ CDM tensions in cosmology today. DES data with a BBN prior constrain H_0 to $0.715^{+0.021}_{-0.019}$, very similar in mean and uncertainty to the TRGB local H_0 constraint. We also find that DES 3×2 pt does not significantly impact the upper bound of neutrino mass derived from other probes. Combining DES 3×2 pt with Ext. Low- z and CMB yields $\sum m_\nu < 0.14$ eV. We caution that we have placed a sharp prior at $\sum m_\nu = 0.06 - 0.6$ eV, which removes the parameter space of unphysical negative neutrino masses and reflects the current bounds from neutrino oscillation experiments.

In the larger context of weak lensing experiments, there has been a historic trend across measurements to prefer a slightly lower S_8 than the CMB-predicted value. The full-survey results from DES and e.g. KiDS [7] have tended to find slightly higher S_8 values than before, while remaining in excellent agreement with our previous DES analyses. At the same time, the joint CMB constraints from *Planck* 2018, SPT-3G DR1, and ACT-DR6 also shrank asymmetrically to slightly higher predictions of S_8 vs. *Planck* alone, leaving the DES-CMB consistency at 2.8σ . This leaves the overall state of the field in a similar place as it was in previous years: we see no substantial evidence for a discrepancy with the CMB in either S_8 or the full parameter space, with various estimates of significance across weak lensing experiments still ranging from $\sim 1\sigma$ to $\lesssim 3\sigma$.

The first cosmology analysis using two-point functions in DES was performed in 2016 [149] using cosmic shear from Science Verification data, alongside with first clustering and galaxy-galaxy lensing measurements [150, 151]. Over the past 10 years, we have processed more data, developed more sophisticated tools, invented new methodologies and trained a new generation of young scientists. This paper uses ~ 30 times the area, ~ 45 times the number of weak lensing galaxies, a much more optimized clustering sample, and a substantially much more complex and robust analysis framework compared to those first papers. We expect this first analysis using all 6 years of DES data for large-scale structure cosmology to be followed by more creative uses of the Y6 data going forward.

DES is a precursor survey to the Vera C. Rubin Observatory Legacy Survey of Space and Time (LSST), the Euclid mission, and the Nancy Grace Roman Space Telescope High Latitude Imaging Survey (HLIS). Part of the legacy of DES will be its traces in the planned cosmology analysis of these Stage-IV surveys (e.g. position and shear catalogs, redshift calibration, synthetic source injection, the blinding process and multi-stage analysis plan, the 3×2 pt pipeline, etc.). The journey of DES, together with other Stage-III galaxy imaging surveys, will continue with LSST, Euclid and Roman, opening the next golden era of galaxy imaging surveys.

IX. DATA AVAILABILITY

The data used in this analysis, including catalogues, data-vector measurements, likelihoods and chains, will be made public upon journal acceptance. The DES Y6 Gold catalogue derived from the DES Data Release 2 (DR2) is publicly avail-

able at <https://des.ncsa.illinois.edu/releases>.

ACKNOWLEDGMENTS

We would like to thank Angus H. Wright, Catherine Heymans and Rachel Mandelbaum for their input to Sec. VIIC, and the KiDS and HSC collaborations for providing their sampled posteriors used therein. We thank Sebastian Bocquet and the SPT collaboration for sharing the SPT-clusters chains. We also thank the TDCOSMO collaboration for providing early access to their likelihood and to Martin Millon for his help implementing it in COSMOSIS.

Author contributions: All authors contributed to this paper and/or carried out infrastructure work that made this analysis possible. Some highlighted contributions include

- Source sample selection and calibrations: A. Amon, K. Bechtol, M. R. Becker, M. Gatti, R. A. Gruendl, M. Jarvis, F. Menanteau, A. Roodman, E. S. Rykoff, T. Schutt, E. Sheldon, M. Yamamoto
- Lens sample selection and calibrations: S. Avila, M. Crotte, J. Elvin-Poole, E. Legnani, S. Lee, J. Mena-Fernández, A. Porredon, W. Riquelme, M. Rodriguez-Monroy, I. Sevilla-Noarbe, N. Weaverdyck
- Photometric redshifts: A. Amon, A. Alarcon, G. M. Bernstein, G. Camacho-Ciurana, A. Campos, C. Chang, W. d'Áziz-Assignies, J. de Vicente, G. Giannini, J. Myles, J. Prat, C. Sanchez, C.-H. To, L. Toribio San Cipriano, M. A. Troxel, N. Weaverdyck, B. Yin
- Simulations and derived calibrations: D. Anbajagane, J. Beas-Gonzalez, M. R. Becker, J. DeRose, S. Everett, E. Legnani, S. Mau, T. Schutt, M. Tabbutt, C.-H. To, M. Yamamoto, B. Yanny
- Data-vector measurements and cosmological inference: A. Amon, F. Andrade-Oliveira, J. Blazek, G. Campailla, J. M. Coloma-Nadal, W. d'Áziz-Assignies, A. Ferté, G. Giannini, M. Jarvis, E. Krause, E. Legnani, J. Muir, A. Porredon, J. Prat, M. Raveri, S. Samuroff, D. Sanchez-Cid, N. Weaverdyck, M. Yamamoto
- Paper writing and figures: A. Alarcón, A. Amon, G. M. Bernstein, G. Campailla, C. Chang, M. Crotte, W. d'Áziz-Assignies, A. Drlica-Wagner, G. Giannini, E. Krause, J. Muir, A. Porredón, J. Prat, D. Sanchez-Cid, I. Sevilla-Noarbe, M. A. Troxel, N. Weaverdyck, M. Yamamoto, B. Yin
- Comments to manuscript: S. Avila, G. M. Bernstein, S. Bocquet, T. Davis, T. Diehl, S. Dodelson, J. Frieman, I. Harrison, K. Herner, O. Lahav, R. Kron, E. Krause, R. Miquel
- Coordination and scientific management: M. R. Becker and M. Crotte (Year Six Key Project Coordinators), C. Chang and M. A. Troxel (Science Committee Chairs), A. Alarcón, A. Amon, S. Avila, J. Blazek, A. Ferté, G. Giannini, A. Porredon, J. Prat, M. Rodríguez-Monroy, C. Sanchez, D. Sanchez-Cid, T. Schutt, N. Weaverdyck, M. Yamamoto, B. Yin (Working Group and Analysis Team leads)

The remaining authors have made contributions to this paper that include, but are not limited to, the construction of DECam and other aspects of collecting the data; data processing and calibration; developing broadly used methods, codes, and simulations; running the pipelines and validation tests; and promoting the science analysis.

Funding and Institutional Support:

Funding for the DES Projects has been provided by the U.S. Department of Energy, the U.S. National Science Foundation, the Ministry of Science and Education of Spain, the Science and Technology Facilities Council of the United Kingdom, the Higher Education Funding Council for England, the National Center for Supercomputing Applications at the University of Illinois at Urbana-Champaign, the Kavli Institute of Cosmological Physics at the University of Chicago, the Center for Cosmology and Astro-Particle Physics at the Ohio State University, the Mitchell Institute for Fundamental Physics and Astronomy at Texas A&M University, Financiadora de Estudios e Projetos, Fundação Carlos Chagas Filho de Amparo à Pesquisa do Estado do Rio de Janeiro, Conselho Nacional de Desenvolvimento Científico e Tecnológico and the Ministério da Ciência, Tecnologia e Inovação, the Deutsche Forschungsgemeinschaft and the Collaborating Institutions in the Dark Energy Survey.

The Collaborating Institutions are Argonne National Laboratory, the University of California at Santa Cruz, the University of Cambridge, Centro de Investigaciones Energéticas, Medioambientales y Tecnológicas-Madrid, the University of Chicago, University College London, the DES-Brazil Consortium, the University of Edinburgh, the Eidgenössische Technische Hochschule (ETH) Zürich, Fermi National Accelerator Laboratory, the University of Illinois at Urbana-Champaign, the Institut de Ciències de l’Espai (IEEC/CSIC), the Institut de Física d’Altes Energies, Lawrence Berkeley National Laboratory, the Ludwig-Maximilians Universität München and the associated Excellence Cluster Universe, the University of Michigan, NSF NOIRLab, the University of Nottingham, The Ohio State University, the University of Pennsylvania, the University of Portsmouth, SLAC National Accelerator Laboratory, Stanford University, the University of Sussex, Texas A&M University, and the OzDES Membership Consortium.

Based in part on observations at NSF Cerro Tololo Inter-American Observatory at NSF NOIRLab (NOIRLab Prop. ID 2012B-0001; PI: J. Frieman), which is managed by the Association of Universities for Research in Astronomy (AURA) under a cooperative agreement with the National Science Foundation.

The DES data management system is supported by the National Science Foundation under Grant Numbers AST-1138766 and AST-1536171. This work used Jetstream2 and OSN at Indiana University through allocation PHY240006: Dark Energy Survey from the Advanced Cyberinfrastructure Coordination Ecosystem: Services & Support (ACCESS) program, which is supported by U.S. National Science Foundation grants 2138259, 2138286, 2138307, 2137603, and 2138296.

The DES Spanish institutions are partially supported

by MICINN/MICIU/AEI (/10.13039/501100011033) under grants PID2021-123012NB, PID2021-128989NB, PID2022-141079NB, PID2023-153229NA, PID2024-159420NB, PID2024-156844NB, CEX2020-001058-M, CEX2020-001007-S and CEX2024-001441-S, some of which include ERDF/FEDER funds from the European Union, and a grant by LaCaixa Foundation (ID 100010434) code LCF/BQ/PI23/11970028. IFAE is partially funded by the CERCA program of the Generalitat de Catalunya. We acknowledge the use of Spanish Supercomputing Network (RES) resources provided by the Barcelona Supercomputing Center (BSC) in MareNostrum 5 under allocations AECT-2024-3-0020, 2025-1-0045 and 2025-2-0046.

We acknowledge support from the Brazilian Instituto Nacional de Ciência e Tecnologia (INCT) do e-Universo (CNPq grant 465376/2014-2).

This document was prepared by the DES Collaboration using the resources of the Fermi National Accelerator Laboratory (Fermilab), a U.S. Department of Energy, Office of Science, Office of High Energy Physics HEP User Facility. Fermilab is managed by Fermi Forward Discovery Group, LLC, acting under Contract No. 89243024CSC000002.

Appendix A: Unblinding investigations

1. Result from parameter-level unblinding tests

The final stage of (parameter-level) unblinding included three main components that needed to be passed before fully unblinding:

- **Goodness of fit via Δ_{PPD} .** We calculated this separately for ξ_{\pm} , $2 \times 2\text{pt}$ and $3 \times 2\text{pt}$ under a ΛCDM model. For ξ_{\pm} we additionally looked at the values when assuming the NLA IA model instead of TATT. We also looked at $3 \times 2\text{pt}$ under a $w\text{CDM}$ model. For these Δ_{PPD} s, we targeted them to be greater than 0.01 to unblind.
- **Internal consistency via Δ_{PPD} .** From the $3 \times 2\text{pt}$ data vector, we can form 7 pair-wise consistency checks. We calculated all of them assuming a ΛCDM model. These are $P(2 \times 2\text{pt} | 3 \times 2\text{pt})$, $P(\xi_{\pm} | 3 \times 2\text{pt})$, $P(w | 2 \times 2\text{pt})$, $P(\gamma_t | 2 \times 2\text{pt})$, $P(w | \xi_{\pm} + \gamma_t)$, $P(\gamma_t | \xi_{\pm} + w)$, $P(\xi_{\pm} | 2 \times 2\text{pt})$. We targeted $\Delta_{\text{PPD}} > 0.01$ for most of these to unblind. The exception was $P(w | \xi_{\pm} + \gamma_t)$: in our simulation tests [31], we found that this suffers from significant prior-volume effects resulting in very small Δ_{PPD} values even when the data are generated self-consistently. We therefore decided to unblind even if this Δ_{PPD} is < 0.01 .
- **Visual inspection of the nuisance parameters.** We examined the posterior of a subset of the nuisance parameters compared to their priors to see if they significantly push against the prior edges. Here we only looked at parameters where we have derived tight Gaussian priors from simulations or external data, including the source

TABLE VII. Δ_{PPD} values for the unblinding tests with and without lens bin 2. The “No lens bin 2” is the analysis that we unblind and use for all results in this paper, unless noted otherwise. Entries with “-” are dominated by prior volume effects and not considered.

	Linear galaxy bias		Nonlinear galaxy bias	
	All data	No lens bin 2	All data	No lens bin 2
Goodness of fit				
ξ_{\pm}	0.162	0.153	0.153	0.153
ξ_{\pm} (NLA)	0.137	0.139	0.139	0.139
$2 \times 2\text{pt}$	0.032	0.173	0.108	0.233
$3 \times 2\text{pt}$	0.006	0.059	0.006	0.076
$3 \times 2\text{pt}$ ($w\text{CDM}$)	0.007	0.060	0.007	0.066
Internal consistency				
$P(2 \times 2\text{pt} 3 \times 2\text{pt})$	0.062	0.161	0.036	0.208
$P(\xi_{\pm} 3 \times 2\text{pt})$	0.141	0.137	0.136	0.132
$P(w 2 \times 2\text{pt})$	0.293	0.250	0.334	0.460
$P(\gamma_t 2 \times 2\text{pt})$	0.045	0.181	0.256	0.312
$P(w \xi_{\pm} + \gamma_t)$	-	-	-	-
$P(\gamma_t \xi_{\pm} + w)$	0.000	0.053	0.000	0.004
$P(\xi_{\pm} 2 \times 2\text{pt})$	0.004	0.049	0.007	0.051

and lens redshift uncertainties (u^l, u^s), the source calibration uncertainties (m), and the lens magnification parameters (α).

The first column Table VII shows the Δ_{PPD} s from our parameter-level unblinding tests in our first attempt to unblind using the full $3 \times 2\text{pt}$ data vector assuming ΛCDM and linear galaxy bias—it was clear that many of the tests were failing. When further examining the posterior of the nuisance parameters, we found that for the first mode of lens bin 2, the posterior deviated significantly from the prior (see Figure 15), and that bin contributed significantly to the internal tension. Also the posterior of the magnification coefficient for lens bin 6 deviated from its prior, albeit not as severely. A number of investigations were carried out (described in the next section) to isolate the root cause of this tension but were inconclusive. To be conservative, the team decided to remove lens bin 2 for unblinding and for our fiducial results but assess the impact of this decision on cosmology after unblinding. With the removal of lens bin two, the Δ_{PPD} values are shown in the second column of Table VII—we find acceptable Δ_{PPD} s for all goodness of fit and internal consistency tests. In turn, Table VIII shows the goodness of fit based on reduced χ^2 (obtained at the MAP of the chains). Results are broadly consistent with those of Table VII, with p -values increasing above the threshold of 0.01 once lens bin 2 is removed.

When assuming nonlinear galaxy bias as our model, we found similar trends in the Δ_{PPD} values as listed in the third and forth columns of Table VII, except for $P(\gamma_t | w + \xi)$, that remains below 1%, but for a small margin. As a result, we also remove lens bin 2 in our analysis with nonlinear galaxy bias.

TABLE VIII. Goodness of fit based on reduced χ^2 and corresponding p -values for the case of linear galaxy bias (with and without bin 2). The overall conclusions are consistent with the goodness of fit results based on Δ_{PPD} shown in Table VII

	Linear galaxy bias	No lens bin 2
All data		
χ^2/ν		
ξ_{\pm}	$309.1 / 278.4 = 1.11$	$308.1 / 278.7 = 1.11$
ξ_{\pm} (NLA)	$299.7 / 263.4 = 1.14$	$301.2 / 263.5 = 1.14$
$2 \times 2\text{pt}$	$402.0 / 363.5 = 1.11$	$333.2 / 307.3 = 1.08$
$3 \times 2\text{pt}$	$737.0 / 644.9 = 1.14$	$654.3 / 588.4 = 1.11$
$3 \times 2\text{pt}$ ($w\text{CDM}$)	$733.7 / 644.7 = 1.14$	$653.4 / 588.2 = 1.11$
p-value (σs)		
ξ_{\pm}	0.099 (1.28)	0.109 (1.23)
ξ_{\pm} (NLA)	0.062 (1.54)	0.055 (1.6)
$2 \times 2\text{pt}$	0.08 (1.41)	0.148 (1.05)
$3 \times 2\text{pt}$	0.007 (2.47)	0.031 (1.87)
$3 \times 2\text{pt}$ ($w\text{CDM}$)	0.008 (2.39)	0.032 (1.86)

2. Diagnostic tests for lens bin 2

One of the primary hints for potential systematic effects in lens bin 2 is the posterior of the first mode $u_1^{2,1}$ of the redshift uncertainty. When visualized in the redshift distribution space, the implication is that the data prefers a redshift distribution that is pushed to a higher value (see right panel in Figure 15). With these observations, we carried out the following investigations in the case of linear galaxy bias model.

a. Priors on redshift uncertainty

We explored several motivated approaches in widening the priors on the redshift uncertainty, in case we had somehow under-estimated the redshift uncertainty. This did not sufficiently resolve the problem, and we do not think this is a likely scenario as we have extensively tested the redshift pipelines as shown in [Y6SHEARZ, Y6PosPZ, Y6WZ].

First we increased the priors on WZ systematic parameters $\{s_{uk}\}_u$, cf. Y6WZ, and obtained new redshift modes. Next we looked at dropping the additional constraints coming from WZ entirely and only used SOMPZ to construct the modes. Finally, we increased the widths of the priors on the lens bin 2 mode amplitudes, $\{u_1^{2,i}\}_i$, by a factor of 3, allowing for larger variations in the reconstructed $n(z)$ compared to the fiducial priors. For this test, we also increased the prior on the magnification coefficient α^6 by a factor of 3. We found that:

- the lens bin 2 $n(z)$ and its variation, reconstructed from the larger-WZ-priors-redshift-modes were identical to the fiducial case, meaning that the WZ systematic function was already flexible enough in the first run;
- using SOMPZ only for the modes yielded a level of discrepancy similar to that obtained when using SOMPZ+WZ, with posteriors for lens bin 2 comparable to those shown in Figure 15, demonstrating that WZ

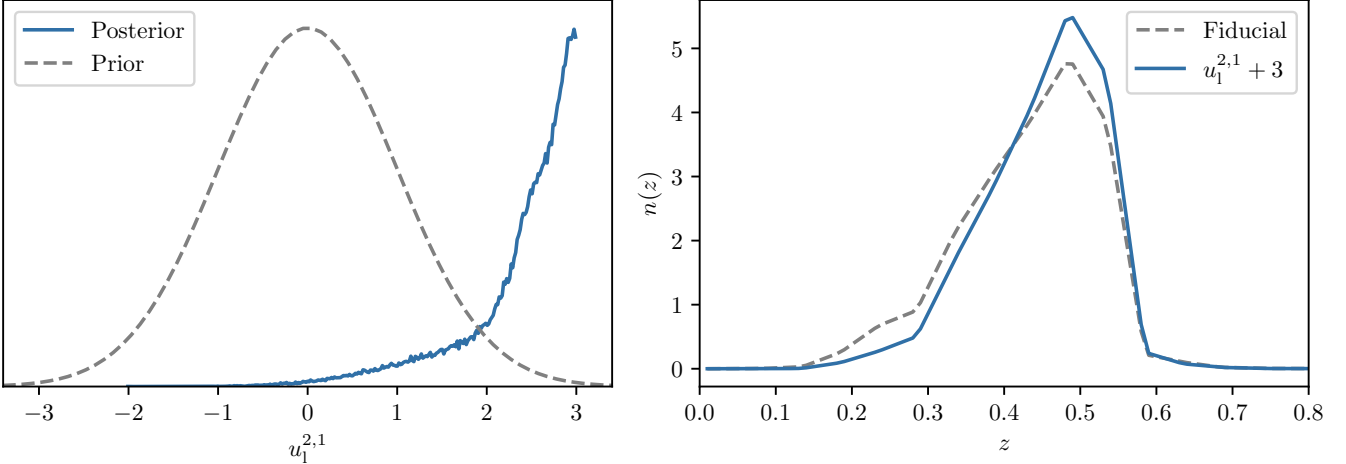


FIG. 15. Left: Posterior distribution of the leading (first) redshift mode coefficient for MAGLIM++ bin 2, $u_1^{2,1}$ (blue), compared to its prior (dashed grey). The posterior peaks toward the upper edge of the prior range. Right: Corresponding mean redshift distribution for MAGLIM++ bin 2, reconstructed from using the fiducial mode coefficients (dashed grey) and an artificially increased value of $u_1^{2,1}$ (blue), chosen to match the posterior shift in the left panel. Increasing the $u_1^{2,1}$ distribution narrows the bin 2 redshift distribution, enhancing the main peak and suppressing the low-redshift contribution around $z \approx 0.25$.

was not the cause of the problem;

- with wider priors, the $3 \times 2\text{pt } \Delta_{\text{PPD}}$ increases to 0.01, which lies at the threshold value, but remains significantly smaller than the $3 \times 2\text{pt } \Delta_{\text{PPD}}$ obtained when excluding lens bin 2 (0.06); the posteriors for lens bin 2 from this wide-prior run are discrepant with the fiducial-prior results at more than the 5σ level.

b. Parametrization of redshift uncertainty

One of the new implementations in Y6 uses modal decomposition [Y6MODES] to characterize the redshift uncertainties instead of the more *ad hoc* “shift and stretch” parametrization used in Y3 and other literature. One concern is that once we have chosen a certain set of modes, the model is only capable of modeling $n(z)$ s that are linear combinations of the modes, potentially excluding a true $n(z)$ that has a qualitatively different shape if it falls outside of our redshift error modeling and likelihood. One example is to examine the right-hand panel of Figure 15. This constrained approach would not be able to model the true $n(z)$ if it has significant support at redshift 0.7.

To diagnose this possibility, we also ran the full set of PPD tests assuming a “shift and stretch” parametrization, where the priors on the shift and stretch are derived from the same ensemble of SOMPZ+WZ $n(z)$ realizations where we derive the principle modes from. This essentially creates a different basis set for modeling redshift errors. We found that this does not significantly improve the $3 \times 2\text{pt } \Delta_{\text{PPD}}$ values (0.007), and the unblinding tests still failed. The posteriors on the lens bin 2 mean redshift are shifted by about 2σ from the prior mean ($\Delta\langle z \rangle \sim 0.015$), and the posterior of the stretch parameter is around 0.8, corresponding to a 5σ tension with the calibration prior. This test therefore rules out the new redshift marginali-

sation method (modes) as the cause of the problem.

3. Covariance mismatch

The Δ_{PPD} numbers are sensitive to the overall amplitude of the covariance matrix. A few percent change could result in the Δ_{PPD} values changing from 10^{-3} to 10^{-2} . There are a few known minor inconsistencies in our covariance matrix modeling that we tested to ensure that these are not the reason for the unacceptable Δ_{PPD} s.

First, the original version of COSMOcov used in this work did not support HMCODE2020, so we instead used HALOFIT for modeling the nonlinear power spectrum. We tested that this effect results in a $< 2.5\%$ difference in some elements of the diagonal of the covariance, which should be a negligible effect. Second, we assumed no IA in the covariance matrix. The validity of this assumption to first order depends on the best-fit IA constraints, which we use to generate the final covariance matrix. However fiducial IA values led to negligible changes in $\Delta\chi^2$, hence we conclude this should not cause low Δ_{PPD} s.

After unblinding, we updated the covariance to include baryonic feedback using HMCODE2020, fixing Θ_{AGN} to our baseline value, and IA. To assess the impact of potential missing components in the fiducial covariance, we recomputed it at the baseline best-fit cosmology, galaxy bias, and intrinsic alignment parameters, adopting the NLA model. The resulting posteriors showed no significant shifts and only negligible changes in constraining power, confirming that the fiducial covariance was sufficiently accurate and stable for the reported cosmological constraints.

4. Magnification priors

Similar to the first mode of the lens bin 2, the posterior of the magnification parameter for lens bin 6, α^6 , pushed against the priors. It was not as severe as $u_1^{2,1}$, but since magnification could be degenerate with cosmological parameters, we check whether the Δ_{PPD} numbers improve significantly when we relax the α^6 prior by a factor of 3 (we also relax the priors on $u_1^{2,1}$, cf. Appendix A 2a). We found that the Δ_{PPD} increased to 0.01, which is larger than the initial value (0.006), but remained small, indicating persistent tension. Then we ran a chain with the original magnification priors, but removing lens bin 2, and obtained a Δ_{PPD} of 0.059. We concluded that despite an apparent discrepancy between the magnification prior and the data posterior, internal consistency is acceptable.

5. Discussion

Given all the tests above, we were not able to unambiguously identify the root cause of the internal inconsistency in our data aside from the fact that it is related to the lens bin 2. We conclude that there is an unknown systematic effect that is likely associated with the lens bin 2. The particular redshift range that lens bin 2 covers has posed long-standing challenges related to the DES filter transitions and color-redshift degeneracies, and this could be at play here. These issues can be exacerbated by sample selection that directly depends on photo-zs in the wide-field survey, as maglim does.¹⁰ It is possible that we are only now reaching a level of precision in our measurements where this internal discrepancy can be detected at the significance we see here. It will continue to be a substantial challenge for future photometric galaxy lensing surveys. To be conservative, we removed all elements of the $3 \times 2\text{pt}$ data-vector that involve lens bin 2 before proceeding with further blinding tests and analyses.

After unblinding, we also examined the parameter constraints when we include lens bin 2 in our data vector. The best-fit cosmological parameters with and without lens bin 2 do not differ significantly, nor does the constraining power. Figure 16 shows our fiducial $3 \times 2\text{pt}$ constraints excluding lens bin 2, compared with the case where lens bin 2 is used. We find small shifts in Ω_m and σ_8 at the 0.4σ level, and negligible change in S_8 . Restoring lens bin 2 improves the overall constraining power by $\lesssim 10\%$ in terms of $\text{FoM}_{\sigma_8, \Omega_m}$, driven by Ω_m , and shows negligible improvement in S_8 errors. This is a reassuring result, suggesting that the unknown systematic effect that is contributing to the internal tension does not impact our cosmological constraints or conclusions. This is also a testimony of the robustness of the $3 \times 2\text{pt}$ combination. We will leave further discussion of the impact of lens bin 2 to the $2 \times 2\text{pt}$ combination in [Y6-2X2PT].

TABLE IX. Prior-volume effects assessment for ΛCDM . Pull statistics (truth-mean)/ σ for simulated runs with input parameters at the MAP values from $3 \times 2\text{pt}$ ΛCDM analysis, for the fiducial $3 \times 2\text{pt}$ linear bias analysis and the subsets $2 \times 2\text{pt}$ and cosmic shear (CS), as well for the nonlinear (NL) galaxy bias case.

Par	$3 \times 2\text{pt}$	$2 \times 2\text{pt}$	CS	TATT	CS NLA	$3 \times 2\text{pt}$ NL	$2 \times 2\text{pt}$ NL
S_8	+0.17	+0.23	+0.10	-0.07	+0.50	+0.35	
Ω_m	-0.32	-0.37	-0.14	-0.31	-0.64	-0.84	
σ_8	+0.26	+0.33	+0.06	+0.17	+0.65	+0.76	

TABLE X. Prior-volume effect assessment for $w\text{CDM}$. Pull statistics (truth-mean)/ σ for simulated runs with input parameters at the MAP values from the $3 \times 2\text{pt}$ ΛCDM analysis.

Parameter	$3 \times 2\text{pt}$	$3 \times 2\text{pt}$ NL
S_8	+0.43	+0.83
Ω_m	-0.05	-0.15
σ_8	+0.22	+0.54
w	+0.40	+0.63

Appendix B: Prior-volume effects

Projection or (prior-)volume effects refer to systematic biases in marginalized parameter posteriors away from the peak of the full-dimensional posterior. This is a model-dependent effect that arises when changes in the parameter volume contribution to the marginal posterior density dominate over changes in the goodness-of-fit. These volume effects tend to be stronger in cases where the likelihood depends nonlinearly on the parameters. When the data are very constraining, the likelihood drops quickly from the maximum-likelihood point and volume effects become negligible; conversely, they can be exacerbated for models with poorly-constrained parameters (see e.g. [152]).

Prior-volume effects complicated our scale cut validation procedure, as described in [Y6MODEL], making it difficult to distinguish between genuine systematic contamination and projection artifacts when testing different scale cut choices. These effects created counterintuitive behavior, where applying stricter scale cuts did not always improve validation performance— $\ddot{\text{A}}$ in some cases, removing more data points actually increased parameter shifts due to enhanced projection effects resulting from reduced constraining power. We assessed these effects by running chains with known input and comparing the posterior means to the true input values, quantified as: (truth-mean)/ σ , where σ is the posterior standard deviation. For this assessment, we first used the “DV v6” data vector employed throughout [Y6MODEL] and found significant shifts of $> 0.5\sigma$ in all parameters of interest, often exceeding 1σ (see more details in [Y6MODEL]). Consequently, we could no longer rely on ΔS_8 as a validation metric for $2 \times 2\text{pt}$ and $3 \times 2\text{pt}$ analyses, and instead only used 2D validation metrics in the (Ω_m, S_8) plane that were less susceptible to these artifacts, eventually using the S_8 metric only for cosmic shear.

In view of this, we agreed on a procedure to address such effects when presenting the results after unblinding. First, we would evaluate these effects during the scale cut process

¹⁰ The source sample does not directly rely on photo-zs for sample selection in the same way, and may be more robust to these issues because of this.

described in [Y6MODEL], as we found they were impacting our constraints. After unblinding, we had agreed to generate a noiseless simulated data vector at the MAP values¹¹ from the real data chains, obtained with a minimizer following the procedure described in Appendix E of [Y6MODEL], and then, with this data vector as input, to run a chain with a setup identical to the data analysis to quantify prior-volume effects under the same conditions, including identical covariance. We agreed before unblinding that parameters showing prior-volume effects larger than 1σ in the simulated data validation should be presented with caveats and would not be highlighted as key results in the abstract or summary tables, though they may be shown in plots alongside their MAP values with clear discussion of the impact.

We present the results of these tests in Table IX for Λ CDM and Table X for w CDM. Under the Λ CDM model, the fiducial linear bias 3×2 pt posterior exhibits minor prior-volume effects of less than 0.5σ for all parameters of interest. Cosmic shear and 2×2 pt analyses show similar behavior. Across all test configurations, linear galaxy bias models exhibit substantially smaller prior-volume effects than nonlinear bias models. For the nonlinear bias model, prior-volume effects are more pronounced, exceeding 0.5σ for most parameters but remaining below 1σ in all cases. For w CDM, the fiducial linear bias model presents minor biases, though larger than in Λ CDM, while the w CDM nonlinear bias model exhibits the largest biases, with a 0.83σ bias in S_8 .

Appendix C: Robustness of the DES Y6 3×2 pt results

In this appendix, we examine the robustness of our constraints by altering a number of analysis choices and comparing the resulting cosmological constraints with our fiducial result. We summarize the exercise in Figure 16 and discuss each test briefly below. The first set of tests concern the choice of a certain model in our pipeline

- **IA:** We use a 4-parameter TATT model as the fiducial IA model, but also look at the results using 1) the Non-linear Linear Alignment model [NLA, 153, 154] and 2) a 5-parameter TATT model, where we in addition free b_{TA} . For 1), adopting the NLA IA model shifts S_8 higher by 0.24σ with no change in the constraining power to $0.793^{+0.012}_{-0.012}$. For 2), we get an S_8 constraint of $0.787^{+0.012}_{-0.011}$, which is a 0.12σ shift from our fiducial analysis. Our results therefore appear to be insensitive to the choice of the IA model.

¹¹ Specifically, we generate a simulated input data vector using the best-fit parameters from the 3×2 pt Λ CDM analysis, including cosmology, galaxy bias, intrinsic alignments, and lens magnification. Redshift distributions and multiplicative shear are fixed to their fiducial values from Table III. We adopt the same priors as in the data chains, except for lens magnification and intrinsic alignment parameters with Gaussian priors, which are shifted to match the input values.

- **Galaxy bias:** As already discussed in Section V A 2, we find that our results are not sensitive to changing the galaxy bias model from linear to nonlinear.
- **Baryonic feedback:** Our fiducial analysis chooses to apply conservative scale cuts and not marginalize over baryonic feedback, but remove sufficient small-scale data so that the bias from fixing the modeled level of baryonic feedback is acceptable (see Section IV C). The parameter that controls the amplitude of the remaining baryonic effect is the sub-grid AGN heating temperature T_{AGN} . We fix $\Theta_{AGN} \equiv \log_{10}(T_{AGN}/K)$ to 7.7 in our fiducial analysis. We check the impact of freeing Θ_{AGN} between 7.3 and 8.3 given the same scale cuts. We find the S_8 constraint changes to $0.793^{+0.013}_{-0.014}$, a 10% less constraining power and a shift of S_8 higher by 0.3σ .
- **Magnification:** Our fiducial analysis derives the Gaussian priors on the lens magnification parameters through synthetic source injection, as described in [Y6MAG]. This differs from the Y3 analysis, in which the magnification parameters were fixed to their estimated values. To assess the impact of this choice, we repeat the analysis with the magnification parameters fixed and find no noticeable change in the inferred value of S_8 . Adopting uninformative flat priors instead of the fiducial priors leads to a shift of -0.27σ in S_8 .

The second set of tests concerns the different sampling strategies used in the analysis

- **MCMC sampler:** All of the results in the paper use the NAUTILUS sample. We check for our fiducial result, if we switch to high-accuracy settings of the POLY-CHORD nested sampling algorithm (the sampler validated in Y3 [155]), we find S_8 constraints for the fiducial 3×2 pt analysis to be $0.787^{+0.013}_{-0.013}$, which is consistent with what we derive from NAUTILUS.
- **Photometric redshift:** One of the new implementations in DES Y6 is that we have taken a more flexible form for parametrizing the redshift uncertainty based on [Y6MODES], where we sample over principal modes of the redshift distribution uncertainties. We check that if we revert back to the more *ad hoc* method of shifting and stretching a fixed mean $n(z)$, we get S_8 constraint of $0.781^{+0.011}_{-0.011}$. This shifts S_8 by about 0.5σ . Tests in [Y6MODES] show that the $n(z)$ modes and their amplitude priors better capture the uncertainties in the redshift compared to the shift-and-stretch parameters. Our result here demonstrates that the redshift marginalization scheme is indeed important.

We also run a chain with redshift modes constructed without the clustering information from [Y6WZ], obtaining $S_8 = 0.798 \pm 0.013$. Thus adding WZ information produces a shift about 0.7σ in S_8 , with an uncertainty decrease around 10%. This level of shift is larger than expected from the validation chains [Y6SHARPZ, Y6WZ], but the no-WZ and WZ marginalized S_8 contours remain consistent within

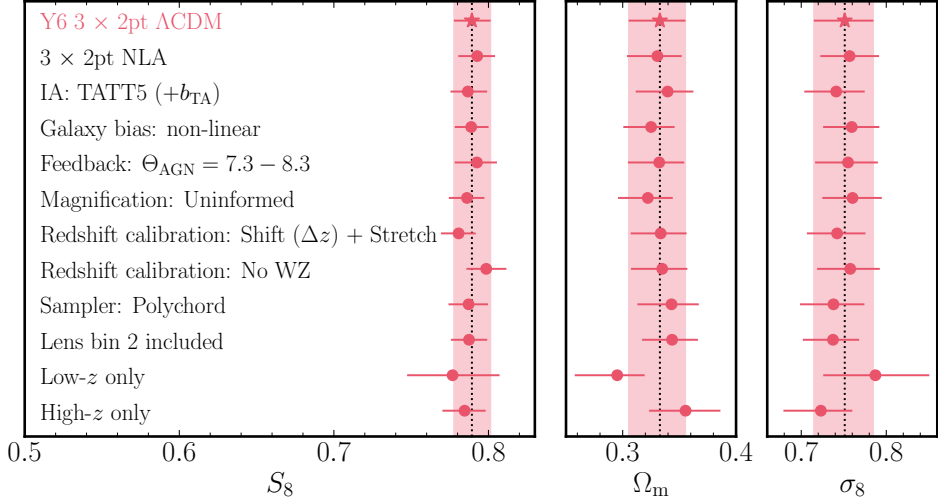


FIG. 16. Constraints on S_8 , Ω_m and σ_8 in Λ CDM from the fiducial 3×2 pt results, compared to a number of robustness tests performed in Section C. All constraints are shown as marginal 1σ constraints. From top to bottom we show our tests for astrophysical effects (IA, galaxy bias, baryonic feedback, magnification), different sampling approaches (changing samplers, different approaches to sample redshift uncertainty), and including/excluding part of the data vector (including lens bin 2, splitting the data by redshift).

1σ . This highlights the strong sensitivity of S_8 to redshift calibration [such sensitivity is evident in the KiDS legacy results, e.g. Figures G1 and I1; 7], and underscores the need for accurate, precise, and redundant redshift-calibration methods.

The third set of tests look at how including/excluding part of the data vector changes the results

- *Including lens bin 2:* We discussed in detail the motivation and investigation associated with the removal of lens bin 2 in Appendix A. Here we check the impact of including lens bin 2 back in the data vector (ignoring the internal inconsistency). We find that with lens bin 2, we have $S_8 = 0.787^{+0.012}_{-0.012}$, $\Omega_m = 0.344^{+0.023}_{-0.026}$, $\sigma_8 = 0.737^{+0.031}_{-0.035}$. The FoM $_{\sigma_8, \Omega_m}$ is slightly higher at 4286 due to the additional statistical power, but the constraints are effectively unchanged (the S_8 constraints shift by 0.12σ). This result is reassuring, and suggests that if there is some unknown systematic effect that is causing lens bin 2 to be inconsistent with the rest of the data vector, the effect of that systematic effect is not coupled with our main cosmology results.
- *High- z /Low- z :* We split the data into halves of high and low redshift. The low- z half consists of the 3×2 pt data vector formed by source bin 1 and 2 and lens bin 1 and 3, while the high- z half contains the remaining bins. We find that the high- z subset of the data gives $S_8 = 0.785^{+0.014}_{-0.014}$ and a FoM $_{\sigma_8, \Omega_m}$ of 2793, while the low- z subset gives $S_8 = 0.777^{+0.030}_{-0.029}$ and a FoM $_{\sigma_8, \Omega_m}$ of 1154. Both subsets shift to slightly lower S_8 values, but all within 0.5σ . The high- z subset dominates the constraining power both due to the higher lensing signal and the fact that we have removed lens bin 2.

Appendix D: Limiting uncertainties in DES Y6 3×2 pt constraints

The cosmological constraints from the DES Y6 3×2 pt analysis are shaped not only by the statistical power of the data but by the treatment of systematic uncertainties that affect both the modeling and the calibration of the observables. This appendix provides estimates of how different systematic effects contribute to the Y6 3×2 pt constraining power. As summarized in Section IV A, we treat these systematic uncertainties through a combination of parametric modeling of systematic effects and data/scale cuts, which exclude measurements affected by systematics not included in the Y6 model. The latter are used to effectively mitigate several effects in the non-linear regime, as accurate models for these effects are ongoing research projects. Scale cuts, however, come at the cost of removing a substantial fraction of the signal-to-noise ratio from the data vector.

Impact of small-scale systematics: As detailed in Section IV C and [Y6MODEL, Y6-1x2PT], key uncertainties in interpreting data points below the scale cuts are baryonic feedback effects on the matter power spectrum, IA in the non-perturbative regime, non-linear galaxy bias, and non-linear matter clustering.

For the cosmic shear data vector, our imposed scale cuts reduce the SNR from 83 to 43, and for galaxy clustering (linear bias, without lens bin 2) our scale cuts reduce the SNR from 233 to 86.

Furthermore, point mass marginalization mitigates the non-local effect of the 1-halo term in galaxy-galaxy lensing above the scale cut. The combination of the scale cuts and point mass marginalization reduce the data vector S/N from 143 to 39 for galaxy-galaxy lensing (without lens bin 2), and from 302 to 95 for the fiducial (NLA, linear galaxy bias, no lens bin

2) 3×2 pt analysis. While it is not straightforward to quantify the contributions of individual systematic effects, nor to convert this S/N difference to cosmological constraining power, a factor three difference in S/N clearly indicates the promise of accurate small-scale modeling. For reference, Y6 represents a factor of 26% improvement in S/N over the Y3 3×2 pt.

Impact of parameterized systematics: To assess how different parameterized systematic effects currently limit the cosmological precision of our analysis, we evaluate a suite of alternative analyses in which one systematic effect at a time is fixed to its best-fit model, thereby isolating how each systematic broadens the posterior on the S_8 parameter. Specifically, we quantify the impact of the uncertainty in our models for intrinsic alignment ($\sim 3\%$), redshift calibration ($\sim 14\%$) and magnification ($< 1\%$).

The dominant term in this category arises from uncertainties in the redshift distributions of both source and lens samples. Intrinsic alignment, magnification and shear uncertainties have a negligible impact on the posterior. Although these effects do not set the overall precision floor, the comparison shows that observational calibration has become an important contributor at Y6 statistical depth, as opposed to what we found in Y3, where redshift uncertainty was negligible. Improvements in redshift calibration, for example, via deeper spectroscopic validation samples [23], would reduce this component of the systematic error.

Appendix E: Full-parameter posterior for the DES Y6 3×2 pt analysis

In the main body of the article, we focused on the marginalized contours in the $S_8 \times \Omega_m$ plane, although our analysis marginalizes over 50 nuisance parameters. Here, we make explicit some of the relevant parameter dependencies.

In Figure 17, we show the posteriors of S_8 and Ω_m along with a subset of the nuisance parameters that are marginalized over, for the linear Λ CDM chain. Among the nuisance parameters with uninformative flat priors, we chose to show the galaxy biases of lens bins 3 and 6, as well as the IA amplitudes. Among the nuisance parameters with calibrated Gaussian priors, we show the source bin 4 multiplicative shear bias parameter m^4 , the lens bin 6 magnification coefficient α^6 , the first redshift modes of lens bins 3 and 6, and the first two redshift modes of the source bins. We deliberately selected parameters that illustrate differences between priors and posteriors, as well as correlations.

Below, we list the findings from the full nuisance-parameter posteriors that are not shown in this figure:

- The magnification coefficients are uncorrelated with all other parameters.
- The second and third redshift modes of each lens bin i , $u_1^{i,1/2}$, are uncorrelated with all other parameters.
- The IA slopes $\alpha_{1/2}^{\text{TATT}}$ are uncorrelated with all other parameters.
- The shear bias coefficients m^2 and m^3 are uncorrelated with cosmology, while m^1 shows a weak correlation.

We also observe correlations between the source redshift modes and the shear bias coefficients.

Below, we list the findings from the nuisance-parameter posteriors shown in Figure 17:

- Cosmology and galaxy biases are correlated.
- Each (linear) bias b_1^i is correlated with the first mode of the corresponding lens bin i , but the lens redshift modes do not show a clear correlation with cosmology.
- Some source redshift modes are correlated with S_8 , the strongest being the first mode.
- There is some correlation between IA amplitudes and cosmology.
- There are weak correlations between IA amplitudes and source redshift modes, but not with lens redshift modes.
- A small correlation is observed between m^4 and S_8 .

Investigation of the full nuisance-parameter posteriors reveals the following about the calibrated priors:

- The posterior of α^6 is in tension with the prior (cf. Appendix A 4).
- The data are informative for the first redshift modes of the lens bins and the first three source redshift modes, as well as for the shear bias coefficient m^4 . No significant tension is observed between priors and posteriors for these parameters.

Appendix F: Changes since Y3

This appendix lists major differences in data, measurements, models, and analysis methods between the current publication and the DES Y3 3×2 pt analysis reported in [37]. See the cited supporting papers for further information.

1. Images to catalogs

- The Y6 analysis is based on 63,888 DECam exposures in the *griz* bands (DR2) [Y6GOLD] as compared to 30,319 exposures in *griz* used in Y3 (DR1) [156].
- Enhanced star-galaxy separation and masking methods [Y6GOLD].
- Color-dependent PSF models [Y6PSF].
- Use METADETECTION in place of METACALIBRATION for shear estimation [Y6SHEAR].
- Increased simulation volume and realism for measuring blending effects on shear, and new parameterization of the blending corrections [Y6IMSIM].
- Deeper source catalog adding ~ 3 galaxies per arcmin 2 thanks to deeper imaging data in Y6. [Y6SHEAR]
- Enhanced masking, including areas ill-suited for systematic weighting [Y6MASK]

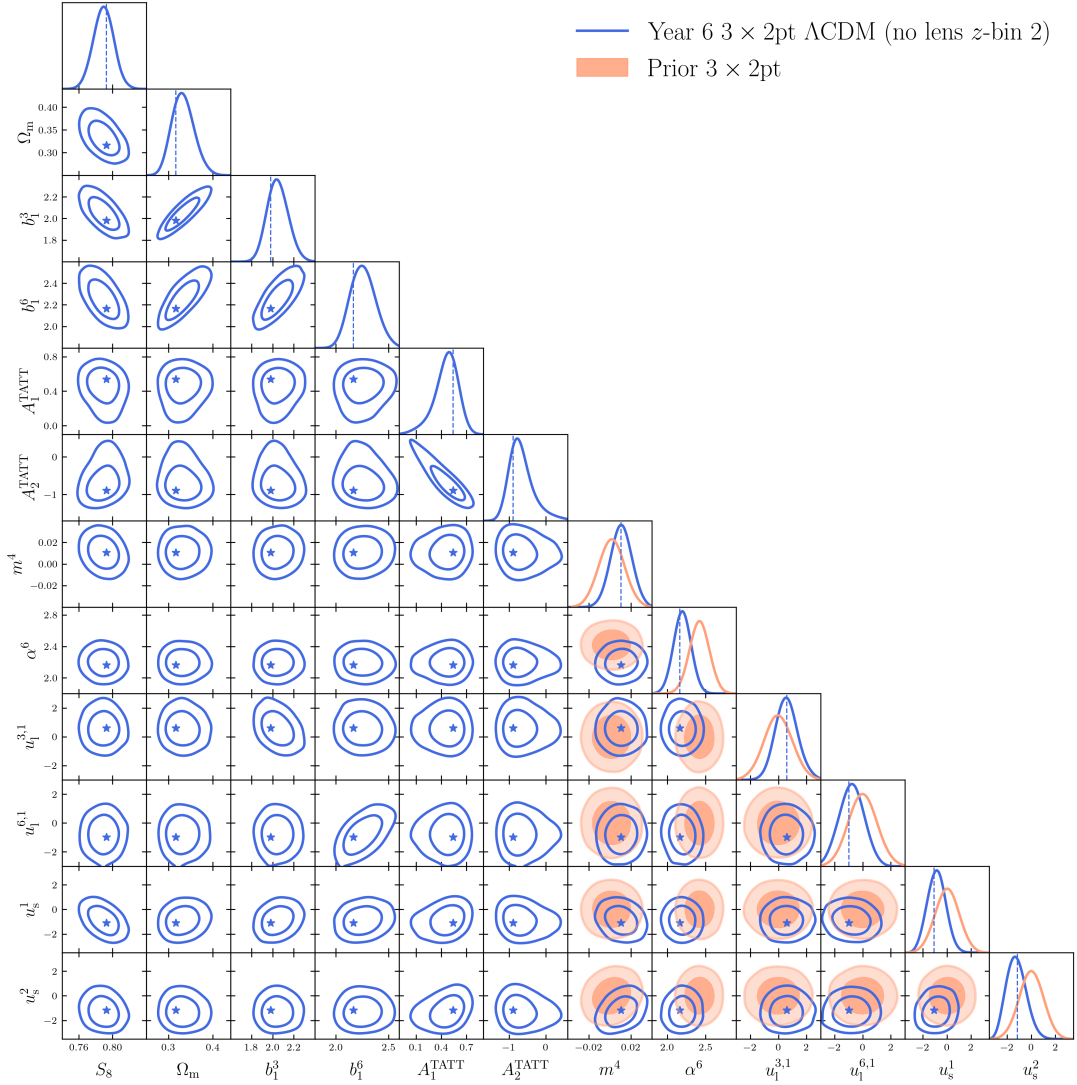


FIG. 17. Cosmological and nuisance parameters posteriors for the 3×2 pt linear Λ CDM chain. We show only a subset of ten nuisance parameters out of the full set of 50. We also plot the gaussian priors for the calibrated ones. All the others have uninformative flat priors.

- Improved selection, including redshift-bin conditioned star-galaxy separation and SOM-based culling of redshift interlopers [[Y6POS](#)].
- Higher resolution systematic galaxy weights with more realistic modeling [[Y6POS](#)].
- From the outset, two differentiated weighting schemes for clustering systematics (ENET and ISD) [[Y6POS](#)].
- Enlarged spectroscopic calibration sample [[Y6SHEARZ](#)].
- Different formulation of systematic-error model, and use of importance sampling after SOMPZ instead of joint sampling [[Y6WZ](#)].
- Compression of $n(z)$ samples' variation into mode coefficients replaces shift-and-stretch approximation to $n(z)$ variation [[Y6SHEARZ](#), [Y6PosPZ](#), [Y6WZ](#), [Y6MODES](#)].
- Shear-ratio likelihood from small scales not used in the 3×2 pt combination, but rather as an independent test of the redshift distributions and multiplicative shear biases for the highest redshift bins [[Y6GGL](#)].

2. Summary statistics and redshifts

- Larger area (100% of DES-wide in Y6 as opposed to 20% in Y3) and modified injection schemes for better accuracy on quantities measured using BALROG source injections [[Y6BALROG](#), [Y6MAG](#)].
- Use of g -band for source galaxy photometric redshifts instead of just riz [[Y6PSF](#), [Y6SHEAR](#)].

3. Models

- HMCode2020 with fixed $\Theta_{\text{AGN}} = 7.7$, instead of HALOFIT without baryons for the nonlinear matter power spectra [Y6MODEL].
- Scale cuts for linear galaxy bias case $w(\theta)$ is 9 Mpc/h instead of 8 Mpc/h and $\xi_{+/-}$ are defined considering extreme baryonic feedback suppression as described by BAHAMAS 8.0 [Y6MODEL] (γ_t is the same).
- Gaussian priors on magnification coefficients, instead of fixed [Y6MAG].
- Gaussian priors $\mathcal{N}(0.0, 3.0)$ truncated to $[-5, 5]$ on the intrinsic alignment redshift evolution parameters η_1 and η_2 (instead of flat as in Y3), b_{TA} fixed to unity (instead of the flat priors used in Y3) and the pivot redshift of $z_0 = 0.3$ instead of $z_0 = 0.62$ [Y6MODEL].
- Correlated priors for multiplicative shear bias and source redshift distribution calibration mode [Y6MODEL].
- Nonzero central values for multiplicative shear bias in covariance matrix [Y6MODEL].
- As in Y3, the default covariance computation uses [99] power spectrum model, while signal modeling has been updated to HMCode2020 with baryonic feedback [Y6MODEL].

- Corrections to the analytic shape/shot noise [100] computed from random catalogs in configuration space to account for the increased small-scale masking of the Y6 data as opposed to mask power spectrum (Y3).
- Numerical debiasing of (minor) $w(\theta)$ weights over-correction [Y6Pos].

4. Inference techniques

- Updated PPD methodology employs a Gaussian mixture model to compute an internal consistency metric which is interpretable without calibration and is more numerically stable than the Y3 implementation [Y6PPD].
- NAUTILUS as fiducial MCMC nested sampler algorithm, instead of POLYCHORD [Y6MODEL].
- Thorough assessment of projection effects.
- Inclusion of internal consistency via Δ_{PPD} as condition for unblinding
- Using normalizing flow for combining independent chains.

[1] Planck Collaboration, Planck 2018 results. VI. Cosmological parameters, *A&A* **641**, A6 (2020), arXiv:1807.06209 [astro-ph.CO].

[2] K. Lodha *et al.* (DESI), Extended Dark Energy analysis using DESI DR2 BAO measurements, arXiv e-prints , arXiv:2503.14743 (2025), arXiv:2503.14743 [astro-ph.CO].

[3] T. Louis *et al.* (ACT), The Atacama Cosmology Telescope: DR6 Power Spectra, Likelihoods and Λ CDM Parameters, arXiv e-prints , arXiv:2503.14452 (2025), arXiv:2503.14452 [astro-ph.CO].

[4] E. Camphuis *et al.* (SPT-3G), SPT-3G D1: CMB temperature and polarization power spectra and cosmology from 2019 and 2020 observations of the SPT-3G Main field, arXiv e-prints , arXiv:2506.20707 (2025), arXiv:2506.20707 [astro-ph.CO].

[5] D. Brout, D. Scolnic, *et al.*, The Pantheon+ Analysis: Cosmological Constraints, *Astrophys. J.* **938**, 110 (2022), arXiv:2202.04077 [astro-ph.CO].

[6] TDCOSMO Collaboration, TDCOSMO 2025: Cosmological constraints from strong lensing time delays, arXiv e-prints , arXiv:2506.03023 (2025), arXiv:2506.03023 [astro-ph.CO].

[7] A. H. Wright *et al.* (KiDS), KiDS-Legacy: Cosmological constraints from cosmic shear with the complete Kilo-Degree Survey, arXiv e-prints , arXiv:2503.19441 (2025), arXiv:2503.19441 [astro-ph.CO].

[8] R. Dalal, X. Li, *et al.* (HSC), Hyper Suprime-Cam Year 3 results: Cosmology from cosmic shear power spectra, *Phys. Rev. D* **108**, 123519 (2023), arXiv:2304.00701 [astro-ph.CO].

[9] S. Gwyn, A. W. McConnachie, *et al.*, UNIONS: The Ultra-violet Near-Infrared Optical Northern Survey, arXiv e-prints , arXiv:2503.13783 (2025), arXiv:2503.13783 [astro-ph.GA].

[10] Euclid Collaboration, Euclid: I. Overview of the Euclid mission, *A&A* **697**, A1 (2025), arXiv:2405.13491 [astro-ph.CO].

[11] DES Collaboration, Dark Energy Survey Year 6 Results: Constraints on extensions to Λ CDM from Galaxy Clustering and Weak Lensing, *in prep* (2026).

[12] DES Collaboration, The Dark Energy Survey: Cosmology Results with ~ 1500 New High-redshift Type Ia Supernovae Using the Full 5 yr Data Set, *ApJ* **973**, L14 (2024), arXiv:2401.02929 [astro-ph.CO].

[13] A. G. Adame *et al.* (DESI), DESI 2024 VI: cosmological constraints from the measurements of baryon acoustic oscillations, *JCAP* **2025**, 021 (2025), arXiv:2404.03002 [astro-ph.CO].

[14] B. Popovic *et al.* (DES), The Dark Energy Survey Supernova Program: A Reanalysis Of Cosmology Results And Evidence For Evolving Dark Energy With An Updated Type Ia Supernova Calibration, arXiv e-prints , arXiv:2511.07517 (2025), arXiv:2511.07517 [astro-ph.CO].

[15] DES Collaboration, The Dark Energy Survey, arXiv e-prints , astro-ph/0510346 (2005), arXiv:astro-ph/0510346 [astro-ph].

[16] DES Collaboration *et al.* (DES), The Dark Energy Survey: more than dark energy - an overview, *MNRAS* **460**, 1270 (2016), arXiv:1601.00329 [astro-ph.CO].

[17] K. Bechtol *et al.* (DES), Dark Energy Survey Year 6 Results: Photometric Data Set for Cosmology, arXiv e-prints , arXiv:2501.05739 (2025), arXiv:2501.05739 [astro-ph.CO].

[18] D. Anbajagane, M. Tabbutt, *et al.* (DES), Dark Energy Survey Year 6 Results: Synthetic-source Injection Across the Full

Survey Using Balrog, *The Open Journal of Astrophysics* **8**, 65 (2025), arXiv:2501.05683 [astro-ph.CO].

[19] T. Schutt et al. (DES), Dark Energy Survey Year 6 Results: Point-Spread Function Modeling, *The Open Journal of Astrophysics* **8**, 26 (2025), arXiv:2501.05781 [astro-ph.CO].

[20] M. Rodríguez-Monroy, N. Weaverdyck, et al. (DES), Dark Energy Survey Year 6 Results: improved mitigation of spatially varying observational systematics with masking, *arXiv e-prints*, arXiv:2509.07943 (2025), arXiv:2509.07943 [astro-ph.CO].

[21] M. Yamamoto, M. R. Becker, et al. (DES), Dark Energy Survey Year 6 results: cell-based coadds and METADETECTION weak lensing shape catalogue, *MNRAS* **543**, 4156 (2025), arXiv:2501.05665 [astro-ph.CO].

[22] N. Weaverdyck, M. Rodríguez-Monroy, et al. (DES), Dark Energy Survey Year 6 Results: MagLim++ Lens Sample Definition and Measurements of Galaxy Clustering, *in prep* (2026).

[23] B. Yin et al. (DES), Dark Energy Survey Year 6 Results: Redshift Calibration of the Weak Lensing Source Galaxies, *arXiv e-prints*, arXiv:2510.23566 (2025), arXiv:2510.23566 [astro-ph.CO].

[24] G. Giannini et al. (DES), Dark Energy Survey Year 6 Results: Redshift Calibration of the MagLim++ Lens Sample, *arXiv e-prints*, arXiv:2509.07964 (2025), arXiv:2509.07964 [astro-ph.CO].

[25] W. d'Assignies et al. (DES), Dark Energy Survey Year 6 Results: Clustering-redshifts and importance sampling of Self-Organised-Maps $n(z)$ realizations for 3×2 pt samples, *arXiv e-prints*, arXiv:2510.23565 (2025), arXiv:2510.23565 [astro-ph.CO].

[26] G. Bernstein et al. (DES), Sampling posterior distributions when only samples from a prior are available, *arXiv e-prints*, arXiv:2506.00758 (2025), arXiv:2506.00758 [astro-ph.IM].

[27] S. Mau, M. Becker, et al. (DES), Dark Energy Survey Year 6 Results: Image Simulations for Weak Lensing Shear and Photometric Redshift Calibration, *in prep* (2026).

[28] C.-H. To et al. (DES), Dark energy survey: Modeling strategy for multiprobe cluster cosmology and validation for the full six-year dataset, *Phys. Rev. D* **112**, 063537 (2025), arXiv:2503.13631 [astro-ph.CO].

[29] D. Sanchez-Cid, A. FertÁl, et al. (DES), Dark Energy Survey Year 6 Results: Multi-Probe Modeling Strategy and Validation, *in prep* (2026).

[30] E. Legnani et al. (DES), Dark Energy Survey Year 6 Results: Magnification modeling and its impact on galaxy clustering and galaxy-galaxy lensing cosmology, *in prep* (2026).

[31] C. Doux, J. Muir, et al. (DES), Dark Energy Survey Year 6 Results: fast and interpretable posterior predictive checks for correlated cosmic probes, *in prep* (2026).

[32] G. Giannini et al. (DES), Dark Energy Survey Year 6 Results: Galaxy-galaxy Lensing, *in prep* (2026).

[33] DES Collaboration, Dark Energy Survey Year 6 Results: Cosmological Constraints from Cosmic Shear, *in prep* (2026).

[34] DES Collaboration, Dark Energy Survey Year 6 Results: Cosmological Constraints from Galaxy Clustering and Galaxy-Galaxy Lensing, *in prep* (2026).

[35] W. Hu and B. Jain, Joint galaxy-lensing observables and the dark energy, *Phys. Rev. D* **70**, 043009 (2004), arXiv:astro-ph/0312395 [astro-ph].

[36] DES Collaboration, Dark Energy Survey Year 1 Results: Cosmological Constraints from Galaxy Clustering and Weak Lensing, *Phys. Rev. D* **98**, 043526 (2018), arXiv:1708.01530 [astro-ph.CO].

[37] DES Collaboration, Dark Energy Survey Year 3 results: Cosmological constraints from galaxy clustering and weak lensing, *Phys. Rev. D* **105**, 023520 (2022), arXiv:2105.13549 [astro-ph.CO].

[38] K. Kuijken et al. (KiDS), Gravitational lensing analysis of the Kilo-Degree Survey, *Mon. Not. R. Astron. Soc.* **454**, 3500 (2015), arXiv:1507.00738 [astro-ph.CO].

[39] C. Heymans et al. (KiDS), KiDS-1000 Cosmology: Multi-probe weak gravitational lensing and spectroscopic galaxy clustering constraints, *Astron. Astrophys.* **646**, A140 (2021), arXiv:2007.15632 [astro-ph.CO].

[40] H. Aihara et al. (HSC), The Hyper Suprime-Cam SSP Survey: Overview and Survey Design, *Publ. Astron. Soc. Jap.* **70**, S4 (2018), arXiv:1704.05858 [astro-ph.IM].

[41] C. Hikage et al. (HSC), Cosmology from cosmic shear power spectra with Subaru Hyper Suprime-Cam first-year data, *Publ. Astron. Soc. Jap.* **71**, 43 (2019), arXiv:1809.09148 [astro-ph.CO].

[42] T. Hamana et al. (HSC), Cosmological constraints from cosmic shear two-point correlation functions with HSC survey first-year data, *Publ. Astron. Soc. Jap.* **72**, 16 (2020), arXiv:1906.06041 [astro-ph.CO].

[43] S. Sugiyama et al. (HSC), Hyper Suprime-Cam Year 3 results: Cosmology from galaxy clustering and weak lensing with HSC and SDSS using the minimal bias model, *Phys. Rev. D* **108**, 123521 (2023), arXiv:2304.00705 [astro-ph.CO].

[44] H. Miyatake et al. (HSC), Hyper Suprime-Cam Year 3 results: Cosmology from galaxy clustering and weak lensing with HSC and SDSS using the emulator based halo model, *Phys. Rev. D* **108**, 123517 (2023), arXiv:2304.00704 [astro-ph.CO].

[45] T. Zhang et al., Cosmology and Source Redshift Constraints from Galaxy Clustering and Tomographic Weak Lensing with HSC Y3 and SDSS using the Point-Mass Correction Model, *arXiv e-prints*, arXiv:2507.01386 (2025), arXiv:2507.01386 [astro-ph.CO].

[46] DES Collaboration, Dark energy survey year 3 results: Cosmological constraints from cluster abundances, weak lensing, and galaxy clustering, *Phys. Rev. D* **112**, 083535 (2025), arXiv:2503.13632 [astro-ph.CO].

[47] DES Collaboration, Dark Energy Survey: A 2.1% measurement of the angular baryonic acoustic oscillation scale at redshift $z_{\text{eff}}=0.85$ from the final dataset, *Phys. Rev. D* **110**, 063515 (2024), arXiv:2402.10696 [astro-ph.CO].

[48] DES Collaboration, Dark Energy Survey Year 6 Results: Cosmological constraints from four dark energy probes, *in prep* (2026).

[49] N. Jeffrey, M. Gatti, et al. (DES), Dark Energy Survey Year 3 results: Curved-sky weak lensing mass map reconstruction, *MNRAS* **505**, 4626 (2021), arXiv:2105.13539 [astro-ph.CO].

[50] S. Bocquet et al. (DES and SPT), SPT clusters with DES and HST weak lensing. II. Cosmological constraints from the abundance of massive halos, *Phys. Rev. D* **110**, 083510 (2024), arXiv:2401.02075 [astro-ph.CO].

[51] H. T. Diehl et al., *The DES and Operations: Year 6 àÁS The Finale*, Tech. Rep. (SLAC National Accelerator Laboratory (SLAC), Menlo Park, CA (United States); Fermi National Accelerator Laboratory (FNAL), Batavia, IL (United States), 2020).

[52] K. Honscheid et al. (DES), The Dark Energy Camera (DE-Cam), ICHEP08 (2008), arXiv:0810.3600 [astro-ph].

[53] B. Flaugher et al. (DES), The Dark Energy Camera, *A.J.* **150**, 150 (2015), arXiv:1504.02900 [astro-ph.IM].

[54] DES Collaboration, The Dark Energy Survey Data Release 2, *ApJS* **255**, 20 (2021), arXiv:2101.05765 [astro-ph.IM].

[55] E. Morganson *et al.* (DES), The Dark Energy Survey Image Processing Pipeline, *PASP* **130**, 074501 (2018), [arXiv:1801.03177 \[astro-ph.IM\]](#).

[56] J. De Vicente, E. Sánchez, and I. Sevilla-Noarbe, DNF - Galaxy photometric redshift by Directional Neighbourhood Fitting, *MNRAS* **459**, 3078 (2016), [arXiv:1511.07623 \[astro-ph.CO\]](#).

[57] W. G. Hartley, A. Choi, *et al.* (DES), Dark Energy Survey Year 3 Results: Deep Field optical + near-infrared images and catalogue, *MNRAS* **509**, 3547 (2022), [arXiv:2012.12824 \[astro-ph.CO\]](#).

[58] E. Suchyta *et al.*, No galaxy left behind: accurate measurements with the faintest objects in the Dark Energy Survey, *MNRAS* **457**, 786 (2016), [arXiv:1507.08336 \[astro-ph.GA\]](#).

[59] S. Everett *et al.* (DES), Dark Energy Survey Year 3 Results: Measuring the Survey Transfer Function with Balrog, *ApJS* **258**, 15 (2022), [arXiv:2012.12825 \[astro-ph.CO\]](#).

[60] E. S. Sheldon, M. R. Becker, N. MacCrann, and M. Jarvis, Mitigating Shear-dependent Object Detection Biases with Metacalibration, *Astrophys. J.* **902**, 138 (2020), [arXiv:1911.02505 \[astro-ph.CO\]](#).

[61] R. Armstrong *et al.* (LSST DESC), The little coadd that could: Estimating shear from coadded images, *arXiv e-prints*, [arXiv:2407.01771 \(2024\)](#), [arXiv:2407.01771 \[astro-ph.CO\]](#).

[62] M. Jarvis *et al.* (DES), Dark Energy Survey year 3 results: point spread function modelling, *MNRAS* **501**, 1282 (2021), [arXiv:2011.03409 \[astro-ph.IM\]](#).

[63] N. MacCrann, M. R. Becker, *et al.* (DES), Dark Energy Survey Y3 results: blending shear and redshift biases in image simulations, *MNRAS* **509**, 3371 (2022), [arXiv:2012.08567 \[astro-ph.CO\]](#).

[64] A. Porredon *et al.* (DES), Dark Energy Survey Year 3 results: Optimizing the lens sample in a combined galaxy clustering and galaxy-galaxy lensing analysis, *Phys. Rev. D* **103**, 043503 (2021), [arXiv:2011.03411 \[astro-ph.CO\]](#).

[65] N. Weaverdyck, D. Schlegel, and A. Raichoor, Mitigating additive contamination via redshift bin optimized star-galaxy separation, *in prep* (2026).

[66] D. Lang, unWISE: Unblurred Coadds of the WISE Imaging, *A.J.* **147**, 108 (2014), [arXiv:1405.0308 \[astro-ph.IM\]](#).

[67] A. M. Meisner, D. Lang, and D. J. Schlegel, Deep full-sky coadds from three years of *wise* and NEOWISE observations, *The Astronomical Journal* **154**, 161 (2017).

[68] N. Weaverdyck and D. Huterer, Mitigating contamination in LSS surveys: a comparison of methods, *MNRAS* **503**, 5061 (2021), [arXiv:2007.14499 \[astro-ph.CO\]](#).

[69] M. Rodríguez-Monroy *et al.* (DES), Dark Energy Survey Year 3 results: galaxy clustering and systematics treatment for lens galaxy samples, *MNRAS* **511**, 2665 (2022), [arXiv:2105.13540 \[astro-ph.CO\]](#).

[70] M. J. Jarvis *et al.*, The VISTA Deep Extragalactic Observations (VIDEO) survey, *MNRAS* **428**, 1281 (2013), [arXiv:1206.4263 \[astro-ph.CO\]](#).

[71] H. J. McCracken *et al.*, UltraVISTA: a new ultra-deep near-infrared survey in COSMOS, *A&A* **544**, A156 (2012), [arXiv:1204.6586 \[astro-ph.CO\]](#).

[72] J. Gschwend *et al.* (DES), DES science portal: Computing photometric redshifts, *Astronomy and Computing* **25**, 58 (2018), [arXiv:1708.05643 \[astro-ph.GA\]](#).

[73] S. J. Lilly *et al.*, The zCOSMOS 10k-Bright Spectroscopic Sample, *ApJS* **184**, 218 (2009).

[74] D. C. Masters *et al.*, The Complete Calibration of the Color-Redshift Relation (C3R2) Survey: Survey Overview and Data Release 1, *Astrophys. J.* **841**, 111 (2017).

[75] D. C. Masters *et al.*, The Complete Calibration of the Color-Redshift Relation (C3R2) Survey: Analysis and Data Release 2, *Astrophys. J.* **877**, 81 (2019), [arXiv:1904.06394 \[astro-ph.GA\]](#).

[76] S. A. Stanford *et al.* (Euclid), Euclid Preparation. XIV. The Complete Calibration of the Color-Redshift Relation (C3R2) Survey: Data Release 3, *ApJS* **256**, 9 (2021), [arXiv:2106.11367 \[astro-ph.CO\]](#).

[77] O. Le Fèvre *et al.*, The VIMOS VLT Deep Survey final data release: a spectroscopic sample of 35 016 galaxies and AGN out to $z \sim 6.7$ selected with $17.5 \leq i_{AB} \leq 24.75$, *A&A* **559**, A14 (2013), [arXiv:1307.0545 \[astro-ph.CO\]](#).

[78] M. Scovéggio *et al.*, The VIMOS Public Extragalactic Redshift Survey (VIPERS). Full spectroscopic data and auxiliary information release (PDR-2), *A&A* **609**, A84 (2018), [arXiv:1611.07048 \[astro-ph.GA\]](#).

[79] A. G. Adame *et al.* (DESI), The Early Data Release of the Dark Energy Spectroscopic Instrument, *A.J.* **168**, 58 (2024), [arXiv:2306.06308 \[astro-ph.CO\]](#).

[80] J. R. Weaver *et al.*, COSMOS2020: A Panchromatic View of the Universe to $z \sim 10$ from Two Complementary Catalogs, *ApJS* **258**, 11 (2022), [arXiv:2110.13923 \[astro-ph.GA\]](#).

[81] M. Eriksen, A. Alarcon, *et al.*, The PAU Survey: early demonstration of photometric redshift performance in the COSMOS field, *MNRAS* **484**, 4200 (2019), [arXiv:1809.04375 \[astro-ph.GA\]](#).

[82] D. Navarro-Gironés *et al.*, The PAU survey: photometric redshift estimation in deep wide fields, *MNRAS* **534**, 1504 (2024), [arXiv:2312.07581 \[astro-ph.CO\]](#).

[83] C. Sánchez, J. Prat, *et al.* (DES), Dark Energy Survey Year 3 Results: Exploiting small-scale information with lensing ratios, *Phys. Rev. D* **105**, 083529 (2022), [arXiv:2105.13542 \[astro-ph.CO\]](#).

[84] M. Jarvis, TreeCorr: Two-point correlation functions, *Astrophysics Source Code Library*, record ascl:1508.007 (2015).

[85] J. Zuntz *et al.*, Cosmoss: Modular cosmological parameter estimation, *Astronomy and Computing* **12**, 45–59 (2015).

[86] A. Stebbins, Weak Lensing On the Celestial Sphere, *arXiv e-prints*, [astro-ph/9609149 \(1996\)](#), [arXiv:astro-ph/9609149 \[astro-ph\]](#).

[87] A. Lewis, A. Challinor, and A. Lasenby, Efficient Computation of Cosmic Microwave Background Anisotropies in Closed Friedmann-Robertson-Walker Models, *Astrophys. J.* **538**, 473 (2000), [arXiv:astro-ph/9911177 \[astro-ph\]](#).

[88] A. Lewis and S. Bridle, Cosmological parameters from cmb and other data: A monte carlo approach, *Physical Review D* **66**, 10.1103/physrevd.66.103511 (2002).

[89] A. J. Mead, S. Brieden, T. Tröster, and C. Heymans, HMPCODE-2020: improved modelling of non-linear cosmological power spectra with baryonic feedback, *MNRAS* **502**, 1401 (2021), [arXiv:2009.01858 \[astro-ph.CO\]](#).

[90] X. Fang, E. Krause, T. Eifler, and N. MacCrann, Beyond limber: efficient computation of angular power spectra for galaxy clustering and weak lensing, *Journal of Cosmology and Astroparticle Physics* **2020** (05), 010–010.

[91] I. G. McCarthy, J. Schaye, S. Bird, and A. M. C. Le Brun, The BAHAMAS project: calibrated hydrodynamical simulations for large-scale structure cosmology, *MNRAS* **465**, 2936 (2017), [arXiv:1603.02702 \[astro-ph.CO\]](#).

[92] N. MacCrann, J. Blazek, B. Jain, and E. Krause, Controlling and leveraging small-scale information in tomographic galaxy-galaxy lensing, *MNRAS* **491**, 5498 (2020), [arXiv:1903.07101 \[astro-ph.CO\]](#).

[93] J. A. Blazek, N. MacCrann, M. A. Troxel, and X. Fang, Be-

yond linear galaxy alignments, *Phys. Rev. D* **100**, 103506 (2019), [arXiv:1708.09247 \[astro-ph.CO\]](#).

[94] C. M. Hirata and U. Seljak, Intrinsic alignment-lensing interference as a contaminant of cosmic shear, *Phys. Rev. D* **70**, 063526 (2004), [arXiv:astro-ph/0406275 \[astro-ph\]](#).

[95] S. Bridle and L. King, Dark energy constraints from cosmic shear power spectra: impact of intrinsic alignments on photometric redshift requirements, *New Journal of Physics* **9**, 444 (2007), [arXiv:0705.0166 \[astro-ph\]](#).

[96] E. Krause and T. Eifler, cosmolike - cosmological likelihood analyses for photometric galaxy surveys, *MNRAS* **470**, 2100 (2017), [arXiv:1601.05779 \[astro-ph.CO\]](#).

[97] X. Fang, T. Eifler, and E. Krause, 2D-FFTLog: efficient computation of real-space covariance matrices for galaxy clustering and weak lensing, *MNRAS* **497**, 2699 (2020), [arXiv:2004.04833 \[astro-ph.CO\]](#).

[98] O. Friedrich et al. (DES), Dark Energy Survey year 3 results: covariance modelling and its impact on parameter estimation and quality of fit, *MNRAS* **508**, 3125 (2021), [arXiv:2012.08568 \[astro-ph.CO\]](#).

[99] R. Takahashi, M. Sato, T. Nishimichi, A. Taruya, and M. Oguri, Revising the Halofit Model for the Nonlinear Matter Power Spectrum, *Astrophys. J.* **761**, 152 (2012), [arXiv:1208.2701 \[astro-ph.CO\]](#).

[100] M. A. Troxel, Krause, E., et al. (DES), Survey geometry and the internal consistency of recent cosmic shear measurements, *MNRAS* **479**, 4998 (2018), [arXiv:1804.10663 \[astro-ph.CO\]](#).

[101] E. Krause et al. (DES), Dark Energy Survey Year 3 Results: Multi-Probe Modeling Strategy and Validation, [arXiv e-prints](#), [arXiv:2105.13548 \(2021\)](#), [arXiv:2105.13548 \[astro-ph.CO\]](#).

[102] A. Porredon et al. (DES), Dark Energy Survey Year 3 results: Cosmological constraints from galaxy clustering and galaxy-galaxy lensing using the MagLim lens sample, *Phys. Rev. D* **106**, 103530 (2022), [arXiv:2105.13546 \[astro-ph.CO\]](#).

[103] S. Pandey et al. (DES), Dark Energy Survey year 3 results: Constraints on cosmological parameters and galaxy-bias models from galaxy clustering and galaxy-galaxy lensing using the redMaGiC sample, *Phys. Rev. D* **106**, 043520 (2022), [arXiv:2105.13545 \[astro-ph.CO\]](#).

[104] J. U. Lange, NAUTILUS: boosting Bayesian importance nested sampling with deep learning, *MNRAS* **525**, 3181 (2023), [arXiv:2306.16923 \[astro-ph.IM\]](#).

[105] M. Raveri, C. Doux, and S. Pandey, Understanding posterior projection effects with normalizing flows, [arXiv \(2024\)](#), [arXiv:2409.09101 \[astro-ph.IM\]](#).

[106] M. Raveri and C. Doux, Non-Gaussian estimates of tensions in cosmological parameters, *Phys. Rev. D* **104**, 043504 (2021), [arXiv:2105.03324 \[astro-ph.CO\]](#).

[107] M. Gatti et al. (DES), Dark Energy Survey Year 3 results: Simulation-based cosmological inference with wavelet harmonics, scattering transforms, and moments of weak lensing mass maps. II. cosmological results, *Phys. Rev. D* **111**, 063504 (2025), [arXiv:2405.10881 \[astro-ph.CO\]](#).

[108] M. Raveri and W. Hu, Concordance and discordance in cosmology, *Phys. Rev. D* **99**, 043506 (2019), [arXiv:1806.04649 \[astro-ph.CO\]](#).

[109] C. Doux et al. (DES), Dark energy survey internal consistency tests of the joint cosmological probes analysis with posterior predictive distributions, *MNRAS* **503**, 2688 (2021), [arXiv:2011.03410 \[astro-ph.CO\]](#).

[110] DES Collaboration, Dark Energy Survey Year 3 results: Constraints on extensions to Λ CDM with weak lensing and galaxy clustering, *Phys. Rev. D* **107**, 083504 (2023), [arXiv:2207.05766 \[astro-ph.CO\]](#).

[111] B. Joachimi et al. (KiDS), KiDS-1000 methodology: Modelling and inference for joint weak gravitational lensing and spectroscopic galaxy clustering analysis, *A&A* **646**, A129 (2021), [arXiv:2007.01844 \[astro-ph.CO\]](#).

[112] DES Collaboration, Dark Energy Survey: implications for cosmological expansion models from the final DES Baryon Acoustic Oscillation and Supernova data, [arXiv e-prints](#), [arXiv:2503.06712 \(2025\)](#), [arXiv:2503.06712 \[astro-ph.CO\]](#).

[113] J. Muir et al. (DES), Blinding multiprobe cosmological experiments, *MNRAS* **494**, 4454 (2020), [arXiv:1911.05929 \[astro-ph.CO\]](#).

[114] J. Mena-Fernández et al. (DES), Dark Energy Survey: Galaxy sample for the baryonic acoustic oscillation measurement from the final dataset, *Phys. Rev. D* **110**, 063514 (2024), [arXiv:2402.10697 \[astro-ph.CO\]](#).

[115] J. Mena-Fernández et al. (DES), Dark Energy Survey: DESI-Independent Angular BAO Measurement, [in prep \(2026\)](#).

[116] B. Popovic et al., A Reassessment of the Pantheon+ and DES 5YR Calibration Uncertainties: Dovekie, [arXiv e-prints](#), [arXiv:2506.05471 \(2025\)](#), [arXiv:2506.05471 \[astro-ph.CO\]](#).

[117] B. O. Sánchez et al. (DES), The Dark Energy Survey Supernova Program: Light Curves and 5 Yr Data Release, *Astrophys. J.* **975**, 5 (2024), [arXiv:2406.05046 \[astro-ph.CO\]](#).

[118] M. Vincenzi et al. (DES), The Dark Energy Survey Supernova Program: Cosmological Analysis and Systematic Uncertainties, *Astrophys. J.* **975**, 86 (2024), [arXiv:2401.02945 \[astro-ph.CO\]](#).

[119] E. S. Rykoff et al., redMaPPer. I. Algorithm and SDSS DR8 Catalog, *Astrophys. J.* **785**, 104 (2014), [arXiv:1303.3562 \[astro-ph.CO\]](#).

[120] M. Costanzi et al. (DES), Cosmological constraints from DES Y1 cluster abundances and SPT multiwavelength data, *Phys. Rev. D* **103**, 043522 (2021), [arXiv:2010.13800 \[astro-ph.CO\]](#).

[121] H.-Y. Wu et al. (DES), Optical selection bias and projection effects in stacked galaxy cluster weak lensing, *MNRAS* **515**, 4471 (2022), [arXiv:2203.05416 \[astro-ph.CO\]](#).

[122] Z. Zhang et al., Modelling galaxy cluster triaxiality in stacked cluster weak lensing analyses, *MNRAS* **523**, 1994 (2023), [arXiv:2202.08211 \[astro-ph.CO\]](#).

[123] C. Zhou et al., Forecasting the constraints on optical selection bias and projection effects of galaxy cluster lensing with multiwavelength data, *Phys. Rev. D* **110**, 103508 (2024), [arXiv:2312.11789 \[astro-ph.CO\]](#).

[124] A. Lee et al., Optical galaxy cluster mock catalogs with realistic projection effects: Validations with the SDSS clusters, *Phys. Rev. D* **111**, 063502 (2025), [arXiv:2410.02497 \[astro-ph.CO\]](#).

[125] C. To, E. Krause, et al. (DES), Dark Energy Survey Year 1 Results: Cosmological Constraints from Cluster Abundances, Weak Lensing, and Galaxy Correlations, *Phys. Rev. Lett.* **126**, 141301 (2021), [arXiv:2010.01138 \[astro-ph.CO\]](#).

[126] DES Collaboration, Dark energy survey year 3 results: Cosmological constraints from cluster abundances, weak lensing, and galaxy clustering, *Phys. Rev. D* **112**, 083535 (2025), [arXiv:2503.13632 \[astro-ph.CO\]](#).

[127] DES Collaboration, First Cosmology Results using Type Ia Supernovae from the Dark Energy Survey: Constraints on Cosmological Parameters, *ApJ* **872**, L30 (2019), [arXiv:1811.02374 \[astro-ph.CO\]](#).

[128] DES Collaboration, Dark Energy Survey Year 3 results: A 2.7% measurement of baryon acoustic oscillation distance scale at redshift 0.835, *Phys. Rev. D* **105**, 043512 (2022), [arXiv:2107.04646 \[astro-ph.CO\]](#).

[129] H. Prince and J. Dunkley, Data compression in cosmology:

A compressed likelihood for Planck data, *Phys. Rev. D* **100**, 083502 (2019), arXiv:1909.05869 [astro-ph.CO].

[130] H. Jense, M. Viña, E. Calabrese, and C. Hill, The choice of Planck CMB likelihood in cosmological analyses, arXiv e-prints , arXiv:2510.09430 (2025), arXiv:2510.09430 [astro-ph.CO].

[131] J.-M. Delouis, L. Pagano, S. Mottet, J.-L. Puget, and L. Vibert, SRoll2: an improved mapmaking approach to reduce large-scale systematic effects in the Planck High Frequency Instrument legacy maps, *A&A* **629**, A38 (2019), arXiv:1901.11386 [astro-ph.CO].

[132] L. Pagano, J.-M. Delouis, S. Mottet, J.-L. Puget, and L. Vibert, Reionization optical depth determination from Planck HFI data with ten percent accuracy, *A&A* **635**, A99 (2020), arXiv:1908.09856 [astro-ph.CO].

[133] C. Garcia-Quintero et al. (DESI), Cosmological implications of DESI DR2 BAO measurements in light of the latest ACT DR6 CMB data, *Phys. Rev. D* **112**, 083529 (2025).

[134] N. Sailer, G. S. Farren, S. Ferraro, and M. White, Disputable: the high cost of a low optical depth, arXiv e-prints , arXiv:2504.16932 (2025), arXiv:2504.16932 [astro-ph.CO].

[135] L. Balkenhol, C. Trendafilova, K. Benabed, and S. Galli, candl: cosmic microwave background analysis with a differentiable likelihood, *A&A* **686**, A10 (2024), arXiv:2401.13433 [astro-ph.CO].

[136] DES and SPT Collaborations, Joint analysis of Dark Energy Survey Year 3 data and CMB lensing from SPT and Planck. III. Combined cosmological constraints, *Phys. Rev. D* **107**, 023531 (2023), arXiv:2206.10824 [astro-ph.CO].

[137] M. Abdul Karim et al. (DESI), DESI DR2 results. II. Measurements of baryon acoustic oscillations and cosmological constraints, *Phys. Rev. D* **112**, 083515 (2025), arXiv:2503.14738 [astro-ph.CO].

[138] N. Schöneberg, The 2024 BBN baryon abundance update, *JCAP* **2024**, 006 (2024), arXiv:2401.15054 [astro-ph.CO].

[139] C. Chang et al. (LSST DESC), A unified analysis of four cosmic shear surveys, *MNRAS* **482**, 3696 (2019), arXiv:1808.07335 [astro-ph.CO].

[140] E. P. Longley, C. Chang, C. W. Walter, et al. (LSST DESC), A unified catalogue-level reanalysis of stage-III cosmic shear surveys, *MNRAS* **520**, 5016 (2023), arXiv:2208.07179 [astro-ph.CO].

[141] DES and KiDS Collaborations, DES Y3 + KiDS-1000: Consistent cosmology combining cosmic shear surveys, *The Open Journal of Astrophysics* **6**, 36 (2023), arXiv:2305.17173 [astro-ph.CO].

[142] A. Porredon et al. (DESI), DESI-DR1 3×2 -pt analysis: consistent cosmology across weak lensing surveys, arXiv e-prints , arXiv:2512.15960 (2025), arXiv:2512.15960 [astro-ph.CO].

[143] X. T. Tang, D. Brout, T. Karwal, C. Chang, V. Miranda, and M. Vincenzi, Uniting the Observed Dynamical Dark Energy Preference with the Discrepancies in Ω_m and H_0 across Cosmological Probes, *ApJ* **983**, L27 (2025), arXiv:2412.04430 [astro-ph.CO].

[144] W. Elbers et al. (DESI), Constraints on neutrino physics from DESI DR2 BAO and DR1 full shape, *Phys. Rev. D* **112**, 083513 (2025), arXiv:2503.14744 [astro-ph.CO].

[145] D. Chebat et al. (DESI), Cosmological neutrino mass: a frequentist overview in light of DESI, arXiv e-prints , arXiv:2507.12401 (2025), arXiv:2507.12401 [astro-ph.CO].

[146] S. Navas et al., Review of particle physics, *Phys. Rev. D* **110**, 030001 (2024).

[147] A. G. Riess et al., A Comprehensive Measurement of the Local Value of the Hubble Constant with $1 \text{ km s}^{-1} \text{ Mpc}^{-1}$ Uncertainty from the Hubble Space Telescope and the SH0ES Team, *ApJ* **934**, L7 (2022), arXiv:2112.04510 [astro-ph.CO].

[148] W. L. Freedman, B. F. Madore, T. J. Hoyt, I. S. Jang, A. J. Lee, and K. A. Owens, Status report on the chicago-carnegie hubble program (cchp): Measurement of the hubble constant using the hubble and james webb space telescopes, *The Astrophysical Journal* **985**, 203 (2025).

[149] DES Collaboration, Cosmology from cosmic shear with Dark Energy Survey Science Verification data, *Phys. Rev. D* **94**, 022001 (2016), arXiv:1507.05552 [astro-ph.CO].

[150] M. Crocce et al. (DES), Galaxy clustering, photometric redshifts and diagnosis of systematics in the DES Science Verification data, *MNRAS* **455**, 4301 (2016), arXiv:1507.05360 [astro-ph.CO].

[151] J. Clampitt et al. (DES), Galaxy-galaxy lensing in the Dark Energy Survey Science Verification data, *MNRAS* **465**, 4204 (2017), arXiv:1603.05790 [astro-ph.CO].

[152] B. Hadzhiyska, K. Wolz, S. Azzoni, D. Alonso, C. García-García, J. Ruiz-Zapatero, and A. Slosar, Cosmology with 6 parameters in the Stage-IV era: efficient marginalisation over nuisance parameters, *The Open Journal of Astrophysics* **6**, 23 (2023), arXiv:2301.11895 [astro-ph.CO].

[153] C. M. Hirata and U. Seljak, Intrinsic alignment-lensing interference as a contaminant of cosmic shear, *Phys. Rev. D* **70**, 063526 (2004), arXiv:astro-ph/0406275 [astro-ph].

[154] S. Bridle and L. King, Dark energy constraints from cosmic shear power spectra: impact of intrinsic alignments on photometric redshift requirements, *New Journal of Physics* **9**, 444 (2007), arXiv:0705.0166 [astro-ph].

[155] P. Lemos, N. Weaverdyck, et al. (DES), Robust sampling for weak lensing and clustering analyses with the Dark Energy Survey, *MNRAS* **521**, 1184 (2023), arXiv:2202.08233 [astro-ph.CO].

[156] D. Collaboration, The Dark Energy Survey: Data Release 1, *ApJS* **239**, 18 (2018), arXiv:1801.03181 [astro-ph.IM].